Determination of nanoparticle size and surface charge in suspension by an electroacoustic method

by

Yaroslav Wroczynskyj

A thesis submitted to the Faculty of Graduate Studies of

The University of Manitoba

in partial fulfilment of the requirements for the degree of

MASTER OF SCIENCE

Department of Physics and Astronomy

University of Manitoba

Winnipeg, Manitoba, Canada

Abstract

An apparatus intended to measure the pressure oscillations generated by nanoparticle suspensions in response to an AC electric field was designed and made operational. Electroacoustic measurements were performed on nanoparticle systems covering a range of particle sizes and zeta-potentials, determined using typical particle characterization techniques. The results of the electroacoustic experiments were mapped to the hydrodynamic size and zeta-potentials of the various nanoparticle systems. It was determined that while the electroacoustic technique can be used successfully to measure the motion of nanoparticles in response to an AC electric field, additional improvements to the electroacoustic apparatus are required to allow for a more rigorous mapping of electroacoustic measurements to particle hydrodynamic size and zeta-potential.

Acknowledgements

The completion of this thesis and the work therein would not have been possible without the untiring aid of my supervisor, Dr. Johan van Lierop. His constant encouragement and willingness to discuss in detail the contents of this work were invaluable. I would like to express deep gratitude also to Dr. John Page, with whom discussions were always enlightening, and to Dr. Donald Miller and Zhizhi Sun for providing a motivation for the completion of this work.

I would like to thank also Ryan Desautels for his help in x-ray diffraction measurements and the interpretation of their results, and to Elizabeth Skoropata and our collaborators at Kent State for providing some of the nanoparticle samples used in this work. I express my gratitude to the support and administrative staff, who were always able and willing to help; the graduate studies administrator, Susan Beshta, for keeping me up to date on deadlines and on track for completion and to Gilles Roy for his seemingly infinite knowledge of the operation of equipment within the department.

I would like to reiterate my thanks to all those listed above for the immense support and motivation they provided. It is through their support that this thesis and the work therein was completed.

Yaroslav Wroczynskyj

October 2014

Contents

List of Figures

List of Tables

Chapter 1

Introduction to the thesis

Magnetic nanoparticles have shown great promise for biomedical applications [1] [2]. To use effectively nanoparticles for biomedical applications, including magnetic hyperthermia treatment, as contrast enhancing agents for magnetic resonance imaging, and targeted drug delivery [3], [4], requires a thorough understanding of nanoparticle properties in application conditions. That is, the effect that application conditions (e.g. biologically relevant materials) have on nanoparticle characteristics such as their size and surface charge must be completely understood. This is because nanoparticle surface charge properties determine not only their stability in suspension but also their particle-particle interactions and how they react with their environment.

Characterization methods used currently to assess these quantities include various optical techniques (electrophoresis [5], dynamic and phase analysis light scattering [6]) along with measurements of a particle's dielectric permittivity (dielectrophoresis

[7]). These methods posses limitations that preclude the determination of nanoparticle hydrodynamic size (i.e. particle size including coating) and surface charge in conditions analogous to the human body. For example, light scattering techniques require optically transparent suspending media along with sufficiently dilute samples so as to ensure single scattering of the incident light [8]. Thus, a technique that is able to probe effectively the surface charge and hydrodynamic size of nanoparticles suspended in biologically relevant materials will prove indispensable towards understanding nanoparticle interactions with complex media (e.g. media containing biological proteins).

It has been determined previously that the magnetic properties of a nanoparticle system can change dramatically with alteration of the nanoparticle surface through coating (e.g. reduced response in a magnetic field) [9], [10]. Mapping the changes in nanoparticle magnetism to quantitative determinations of their surface charge and size in suspension is also necessary towards developing an understanding of the effects that surface modification have on a nanoparticle's magnetism.

Finally, developing a basic understanding of the effects that application conditions have on nanoparticle surface properties and the consequent changes in magnetic behaviour will allow ultimately for the rational design of nanoparticle systems tailor made for specific biomedical applications such as the targeted delivery of pharmaceutical materials, e.g. across the blood-brain-barrier [3].

1.1 Particle surface and electrokinetic properties

Nanoparticles in a liquid suspension can be classified as a sol, a type of colloidal species defined as a solid phase dispersed in a liquid medium [11]. Thus, nanoparticle surface charge and size are determined not only by the nanoparticle composition (both core and coating) but also their environment. Typical coating materials for nanoparticles destined for eventual biomedical use are organic in nature, in the form of ligands or polymers intended to modify the nanoparticle's interaction with human tissue [4], [12]. These organic coatings can be considered diffuse and their conformation around the particle surface can be altered dramatically in response to changes in the suspending medium e.g., solution pH. The diffusive nature of organic materials for nanoparticle surfactants gives rise to problematic definitions of the relevant surface properties of a sol [13]. In particular, the concept of surface charge, or zeta-potential, is intrinsically difficult to define unambiguously as it is model dependent. Additionally, the size of nanoparticles in suspension, or the hydrodynamic size, can vary significantly because the diffuse coating can change conformation depending on the environment. The zeta-potential of a nanoparticle suspension is a crucial quantity for assessing the effectiveness of a particular nanoparticle formulation for application, determining both the colloidal stability of the particles and their interaction with their environment.

To better understand the difficulties in determining nanoparticle zeta-potential, it is important to discuss the electrokinetic theory developed for colloids. The simplest

model of a solid particle in liquid suspension is a two-layer system; the first consisting of a collection of charges firmly affixed to the particle surface along with an outer layer comprised primarily of diffuse charges. The fixed electric charge at the particle surface acts to attract (from the suspending medium) ions of opposite charge near the particle-liquid interface until charge balance occurs (electrically neutral). This electrical double layer model can be parametrized by the particle radius, a, and the Debye screening length, κ^{-1}, which is a measure of the characteristic length of the diffuse ion cloud [14]. The parameter κa is used as classification for the different regimes used in modelling the double layer structure, namely the thin and thick double layer. The thin electrical double layer regime, $\kappa a \gg 1$, describes accurately particles in which the diffuse layer is small with respect to the particle radius (applicable typically to micrometre-sized particles). Conversely, the thick electrical double layer, $\kappa a \ll 1$ regime, occurs for diffuse layers large with respect to the particle size.

In the framework of the electrical double layer model for a sol, the "hard" (solid) particle is assigned a surface potential, Φ_0. While this potential is intuitively the ideal quantity for describing the charge of a colloidal particle in liquid suspension, it is not directly accessible experimentally due to the screening effect of the attracted ions of opposite charge from the suspending medium (counterions). That is, there exists a layer of electrostatically attracted counterions that can be considered stationary with respect to the particle surface, beyond which the counterions are only loosely bound to the particle because of the screening effects of the first layer. It is this loosely

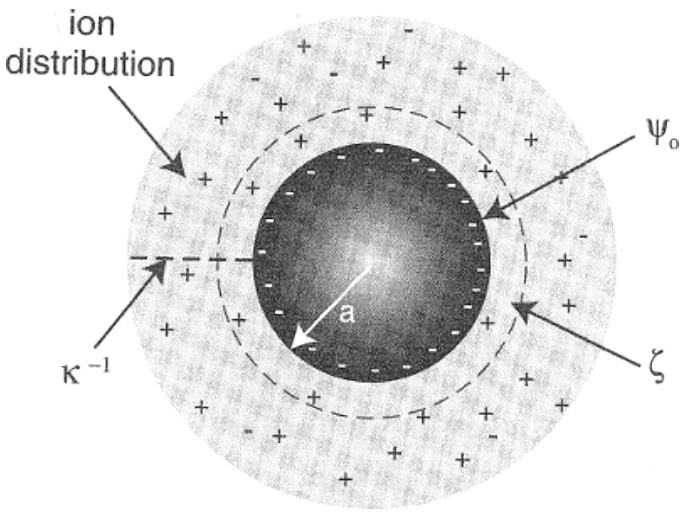

Figure 1.1: A schematic of the electrical double layer model of a particle with radius a in liquid suspension, showing the definition of relevant potentials. The zeta-potential (ζ) is defined at the slip plane (dashed line) - the point after which attracted counterions can be considered stationary [11].

bound layer which can be deformed by external forces such as from an electric field or viscous drag. The boundary between these two regions is known as the shear or slip plane, and the potential at this point is defined as the zeta-potential. A schematic representation of the electrical double layer model is shown Fig. 1.1.

Assessing the zeta-potential of particles in suspensions is done typically by measuring their response to an applied electric field. As with any charged particle, the solid phase of a colloidal suspension will move in response to an electric field. The extent of a particle's motion is defined through the electrophoretic mobility, μ, by [15]

$$\vec{v} = \mu \vec{E} \tag{1.1}$$

where $\vec{E}$ is the applied electric field and $\vec{v}$ is the particle velocity. In the case of a thin double layer ($\kappa a \gg 1$), Smoluchowski [16] has (under the condition of nonconducting particles with no surface electric field) derived a relation between a particle's zeta-potential, ζ, and μ in suspension, namely

$$\mu = \frac{\epsilon\epsilon_0\zeta}{\eta} \tag{1.2}$$

where ϵ and η are the relative permittivity and dynamic viscosity, respectively, of the suspending medium and ϵ_0 is the permittivity (electric field flux per unit charge) of free space. Fundamental to this derivation is the assumption that the externally applied field is not affected by the field created by the charge distribution surrounding the particles in suspension. Polarization of the double layer is not taken into account, and thus the electric and hydrodynamic (e.g. viscous drag) forces can be considered to be acting in opposite directions [13]. For thick double layers ($\kappa a \ll 1$), the colloidal particles can be treated essentially as point charges [11]. For this limit of the double layer, Hückel [17] derived the electrophoretic mobility to be

$$\mu = \frac{2\epsilon\epsilon_0\zeta}{3\eta} \tag{1.3}$$

which is applicable only for moderate values of zeta-potential, e.g. $\zeta < k_BT/e$, where k_BT is the thermal energy and e is the fundamental charge, typically on the order of 25 mV at room temperature. The extensive diffuse layer treated by the Hückel equation leads to a smaller counterion charge density at the interfacial layer, and thus

viscous drag effects are decreased as there is less counterion migration opposite the particle motion [14].

For the region applicable to nanoparticles (moderate values of κa), there exists no convenient framework for the electrophoretic mobility as nanoparticles fall in a region where no favourable assumptions can be made. That is, the particle can no longer be treated as a point charge (as with Hückel's theory) nor can the surface be considered flat (in the Smoluchowski regime). Henry [18] bridged these two regions empirically with a polynomial function, monotonically increasing from 1 to 3/2 (the prefactors of the Smoluchowski and Hückel equations, respectively)

$$\mu = \frac{\epsilon\epsilon_0\zeta}{\eta} f_H(\kappa a) \tag{1.4}$$

where $f_H(x)$ has the structure

$$f_H = 1 + \frac{x^2}{16} - \frac{5x^3}{48} + \frac{x^5 - x^4}{96} + \cdots \tag{1.5}$$

This expression allows for a more accurate determination of particle zeta-potentials from electrophoretic mobility measurements for a wide range of κa values, although it is still somewhat restricted in that it is only valid for moderate values of zeta-potential and does not account for double layer polarization.

The model most applicable to the electrophoretic mobility of nanoparticles can be determined by a calculation of the Debye screening length of a particle in solvent containing N ionic species using [13]

$$\kappa = \left(\frac{\sum_{i=1}^{N} e^2 z_i^2 n_i}{\epsilon \epsilon_0 k_B T} \right)^{1/2} \tag{1.6}$$

where z_i and n_i are the charge and concentration, respectively, of ionic species i. Equation 1.6 illustrates the effects that the concentration and charge of ions present in the suspending medium have on the extent of the diffuse layer. A charge balance is more quickly reached when the suspending medium has a larger concentration of ionic species or the ions have a larger valence, thus leading to smaller diffuse layers. This effect is so strong that some colloidal suspensions can be forced into

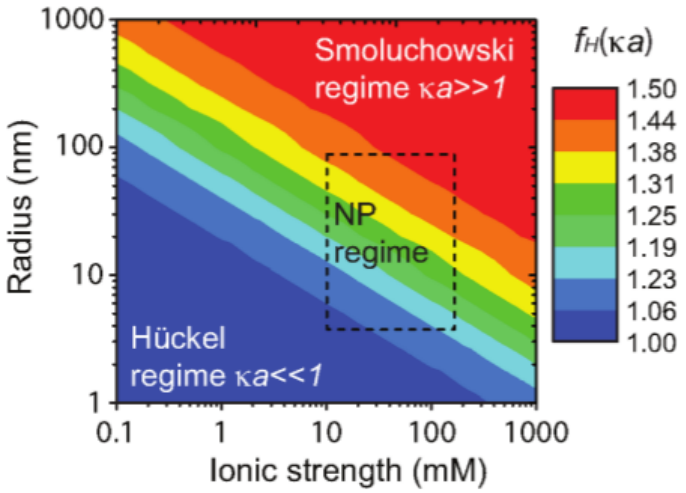

Figure 1.2: A contour plot showing approximately the regions of validity for the various theories of electrophoretic mobility as a function of particle size and ionic strength of the suspending medium. Reprinted with permission from [14]. Copyright 2012 American Chemical Society.

either the Smoluchowski or Hückel regime by altering the type of ions and the ionic concentration in the suspending medium. Figure 1.2 shows the regions of validity for the aforementioned models as functions of particle size and ionic concentration [14]. The application of these models to sizes and ionic concentrations typical of nanoparticle suspensions is also highlighted.

Figure 1.2 illustrates also the difficulty in determining the zeta-potential of nanoparticles, which fall in the transition region between the Smoluchowski and Hückel regimes where only empirical formulations for their electrophoretic mobility exist. Altering the ionic concentration of the fluid in which the nanoparticles are suspended to "push" them into either analytical regime (as is done typically) is often counterproductive as ultimately the zeta-potential must be determined in application conditions where control of the suspending medium is not possible. Thus determining the zeta-potential of nanoparticles from observations of their electrophoretic mobility is a challenging endeavour, not only because of the difficulty in mapping the mobility to the zeta-potential but in actually measuring the electrophoretic mobility.

1.2 Electroacoustic effect

Typical methods of measuring the electrophoretic mobility of colloids rely exclusively on optical techniques. For colloids in optically transparent media and at low concentrations, phase analysis light scattering is the preferred technique [6]. While applicable to nanoparticle suspensions, this technique cannot be used to determine

zeta-potential in conditions analogous to application; blood and biological cells are not optically transparent, and concentrations are typically made as large as possible to ensure the desired effect (e.g. for targeted drug delivery). It is possible to ascertain the electrophoretic mobility of concentrated colloids using classical electrophoresis, where particle motion in a DC electric field is observed using confocal microscopy [5] although it is still limited to optically transparent media. The small size of nanoparticles precludes the use of this technique. Thus to date, no comprehensive study of nanoparticle zeta-potentials in conditions analogous to biomedical application has been performed.

There are methods of obtaining the zeta-potential of colloids that do not rely on optical measurements, but instead use acoustic phenomena. These techniques have been used successfully to determine the zeta-potential of micrometre-sized colloids at moderate concentrations, but they have not yet been used to measure nanoparticle suspensions. If these methods could be extended properly for use with nanoparticle systems, in-depth studies of nanoparticle surface properties in application conditions could be attempted. A discussion of the theory behind these techniques follows.

An applied electric field will induce motion of the charged solid phase of a colloidal suspension relative to the liquid phase. If the DC field discussed previously is substituted for one alternating in magnitude over time (AC field), it is expected that the particle motion will oscillate in turn. Intuitively, the magnitude of the velocity obtained by the particles in an AC field will depend on the strength of the field along

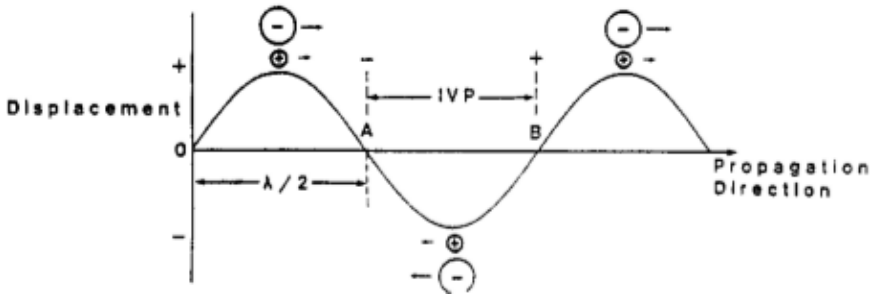

Figure 1.3: A representation of the response of an electrolyte solution to a pressure oscillation of wavelength λ, or the ionic vibration potential. Reprinted with permission from [19]. Copyright 1988 American Chemical Society.

with the overall charge of the particles. Additionally, some phase delay is expected, a consequence of viscous drag forces from the suspending medium (an effect which should in some way depend on the particle's hydrodynamic size). Thus, a method that accurately tracks the motion of a colloid in response to an AC field should provide ultimately a means to assess concurrently the particle hydrodynamic size and zeta-potential directly.

It was theorized by Debye [20] that pressure oscillations travelling through an electrolyte solution would give rise to an electrical potential, assuming that there is a difference in density between the ionic species present in the solution. That is, local changes in pressure would induce relative motion between the cations and anions in the electrolyte, and thus create local changes in potential. This is shown schematically in Fig. 1.3 [19]. First theories of this effect, known as the ionic vibration potential, took into account only frictional (viscous) and electrical forces. Debye's original

theory for the ionic vibration potential has been modified more recently [21] by taking into account electrophoretic and relaxation effects. With these modifications, it was determined that the ionic vibration potential probes not the absolute masses of ions in solution, but their effective mass that account for the displacement of the solvent. The similarities of an ionic solution to a colloidal suspension led other researchers [22], [23] to propose an effect analogous to the ionic vibration potential for colloids, termed the colloid vibration potential.

Whereas the ionic vibration potential relies on the displacement between differ-

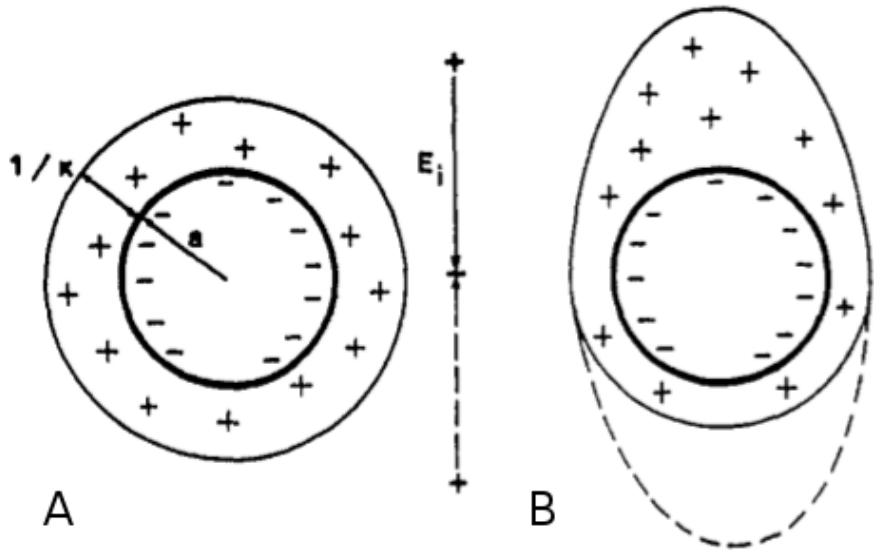

Figure 1.4: A representation of the effect that an applied electric field has on the diffuse layer of a particle in suspension. (A) the diffuse layer is at equilibrium under zero applied field (B) an applied electric field acts to deform the diffuse layer as solid core moves (dashed line is the orientation for an electric field of opposite polarity). Reprinted with permission from [19]. Copyright 1988 American Chemical Society.

ently charged ionic species in suspension, the colloid vibration potential is attributed to the relative motion of the solid core of a colloid from its associated electrical double layer. The diffuse ion cloud surrounding the particle stretches and contracts with the local changes in pressure which occur when an ultrasound wave travels through the suspension. This is effectively a polarization of the double layer which induces an oscillating dipole moment. This is shown schematically in Fig. 1.4. The extent that the electrical double layer polarizes depends essentially on the electrokinetic properties of the colloid and physical properties of the suspending medium, such as the nature of the ionic species and their concentration.

The converse effect of the colloid vibration potential was proposed to be a useful means of measuring the motion of particles in response to an AC electric field and thus allowing for the determination of zeta-potential [24]. This reciprocal phenomena, termed electrokinetic sonic amplitude or the electroacoustic effect, measures the pressure oscillations produced by particles moving in response to an applied AC electric field. If a sample of particles in liquid suspension is subjected to a DC electric field, motion of the charged hard phase will be induced. As the colloid is initially at rest, the suspension has zero momentum and thus the generation of compression waves, i.e. changes in momentum, does not seem possible. This is because to first order (neglecting polarization), the electric field provides no force to the system as a consequence of the particle's electrical neutrality [25]. Indeed, the production of sound occurs only when the sample is contained within a closed volume with a hard physical

boundary which acts to provide an external force and thus change the momentum of the suspension.

This is most easily understood by considering a fixed volume adjacent to the boundary of the suspension, as shown in Fig. 1.5 [25]. An electric field is applied parallel to the normal of the boundary, in this case inducing motion of the solid phase away from the boundary. As the suspension has initially zero momentum, it is required by momentum conservation that

$$\rho_p F_p + \rho F = 0 \tag{1.7}$$

where F_p and F are measures of the volume flowing per unit time of the particles and liquid, and ρ_p and ρ are their respective densities. Equation 1.7 represents essentially the momentum of the suspension; the momentum flux of the particles is

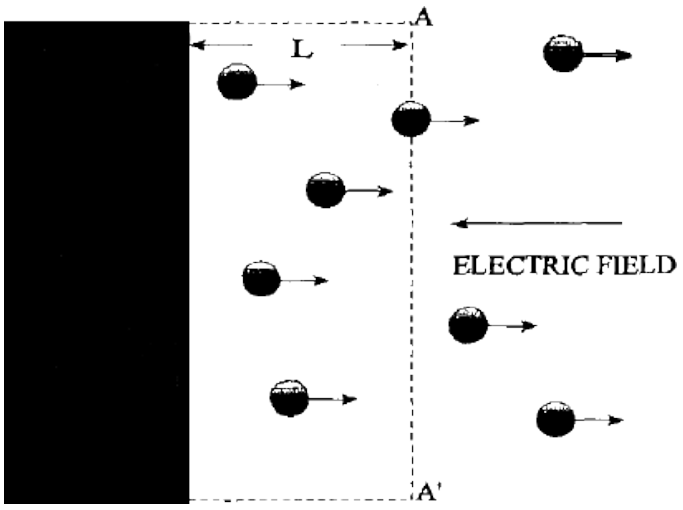

Figure 1.5: A schematic representation of the electroacoustic effect [25].

balanced completely by the momentum flux of the liquid phase. Thus, if the hard and soft phase differ in density, then there must be a difference in the volume flux between the particles and suspending medium. If the above condition is satisfied, there will be a net flux of material across the boundary A-A' in Fig. 1.5, producing local changes in pressure. For AC electric fields, the hard particles are attracted toward and away from the electrode, which causes oscillations in the direction of the net material flux with respect to the suspension boundary, producing ultimately oscillating pressure waves.

The net volume flux near the suspension boundary, F_p+ F, with Eqn. 1.7 gives

$$F_p + F = \frac{\rho - \rho_p}{\rho} F_p = -\frac{\Delta\rho}{\rho}\phi v \tag{1.8}$$

where $\Delta\rho$ is the difference in density between the solid and liquid phases $(\rho_p - \rho)$, ϕ is the particle volume fraction, and v is the average particle velocity. It can be seen from Eqn. 1.8 that compression waves with larger magnitudes will be produced from concentrated colloids with very dense hard phases (relative to the liquid medium). It should be noted that while compression waves should emanate from any boundary of the suspension in the framework of the presented argument, the effect is most pronounced at the electrodes producing the spatially uniform electric field, as the particle motion is parallel to the boundary normal. Although typically ignorable because the product $\phi\Delta\rho$ is small for electrolyte species, their contribution to the produced compression waves must be considered for very dilute colloidal samples,

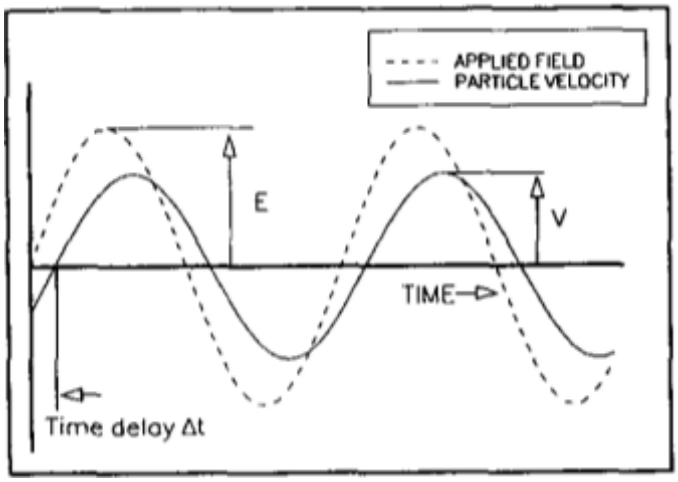

Figure 1.6: Schematic representation of a particle's response in an AC electric field, highlighting the phase delay, Δt, between the electric field and particle velocity arising from viscous drag forces between the particles and suspending medium. Here, E and v represent the magnitude of $\vec{E}$ and $\vec{v}$, respectively. [25].

or in the case of small $\Delta\rho$. The component of the compression waves produced by additional electrolyte species can be simply subtracted from the signal produced from the colloidal sample as the overall electroacoustic signal is a superposition of all the species in suspension [26].

The average velocity in Eqn. 1.8 is the quantity that can be related to the electrophoretic mobility of the colloid (e.g. by means of Eqn. 1.1, modified to take into account the oscillating nature of the electric field). An AC field with frequency ω can be represented as $\vec{E}e^{i\omega t}$, with a complementary particle velocity, $\vec{v}e^{i\omega t}$. For increasing ω, inertial (drag) forces are expected to become more significant introducing a phase delay, Δt, between the electric field and the particle velocity as shown schematically

in Fig. 1.6. Completing the relation between particle velocity and an AC electric field requires modification of the electrophoretic mobility, now a dynamic mobility, μ_D. It is clear from Eqn. 1.1 and the definition of $\vec{E}$ and $\vec{v}$ given above that the dynamic mobility is a complex quantity with magnitude E/V and argument $\omega\Delta$t.

The dynamic mobility, μ_D, can take many forms depending on the system being measured by the electroacoustic method, taking into consideration varying double layer thicknesses as well as particle concentrations and shapes. The simplest model is for spherical particles with a thin double layer at moderate concentrations, up to ~ 5 % w/v (weight of particles over total volume of suspension), satisfying the single scattering limit [27]

$$\mu_D = \frac{2\epsilon\epsilon_0\zeta}{3\eta} G\left(\frac{\rho\omega a^2}{\eta}\right)\left(1 + f\left(\frac{K_s}{K^\infty a}, \frac{\omega\epsilon\epsilon_0}{K^\infty}\right)\right) \tag{1.9}$$

where G is a complex function which represents the inertial forces acting on the particles, $(1 + f)$ accounts for the conductivity of the electric double layer, K_s is the surface conductivity of the double layer and K^∞ is the electrical conductivity of the suspending medium. The magnitude of $G(x)$ decreases monotonically from 1 to 0, while the argument approaches a limit of -$\pi/4$. The form of $G(x)$ is shown in Fig. 1.7. It is the inertial forces acting on the particle which determine the frequency range in which particle size and zeta-potential assessment is possible. That is, when $x \ll 1$, the magnitude of G is approximately one; in this case viscous drag forces are almost negligible and thus over the frequencies in which $x \ll 1$, particle sizing is not possible

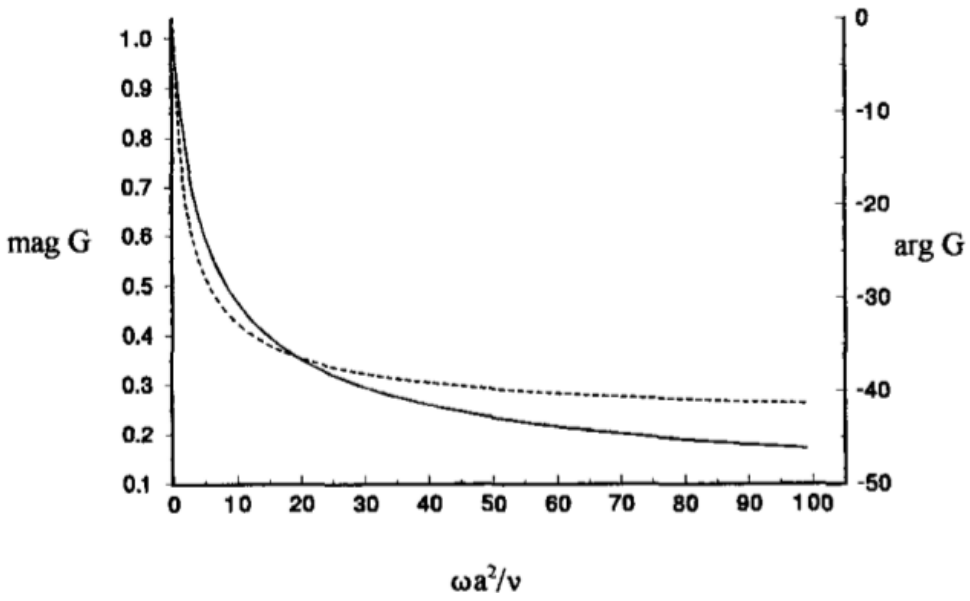

Figure 1.7: Magnitude (solid line) and argument (dashed line) of $G(x)$ which describes the inertial forces acting on a particle in liquid suspension [25].

although zeta-potential is still accessible. For large values of x, the magnitude of G approaches zero, thus decreasing the dynamic mobility. At these frequencies, inertial forces are strong enough that the particles are not able to respond within a sufficient time to the alternating electric field, and no motion is possible. The optimal frequency range for concurrent determination of particle size and zeta-potential is that which $x \simeq 1$, where $G(x)$ changes more drastically. As an example of a useful frequency range for assessing both particle size and zeta-potential, 100 nm particles suspended in water have $x = \rho\omega a^2/\eta = 1$ at 15 MHz.

As mentioned previously, the f factor in the dynamic mobility is related to the particle's double layer conductivity. More correctly, it is a measure of the tangential

electric field at the particle surface. It is this factor which accounts for the polarization of the double layer in an electric field. Polarization of the double layer acts essentially as a secondary drag force on the particle motion. That is, the diffuse ions in the double layer have charge opposite to the particle core and thus create a local electric field opposite in orientation to the applied field. This reduces the overall electric field experienced by the particle as a whole thus reducing the electrophoretic motion of the particle. Fortunately, the $(1 + f)$ factor in Eqn. 1.9 is effectively a constant for most colloids with thin double layers. This can be seen from the dependence of the surface conductivity on the physical properties of the particle and suspending medium, assuming that polarization occurs wholly in the double layer; namely [28]

$$\frac{K_s}{K^{\infty}a} = \frac{2}{\kappa a}\left(\cosh\left[\frac{ze\zeta}{2k_BT}\right] - 1\right)\left(1 + \frac{2\epsilon[k_BT]^2}{z^2\eta De^2}\right) \tag{1.10}$$

where z and D are the valence and diffusivity, respectively, of the ionic species in suspension. For colloids with thin double layers (i.e. κa $\gg 1$), the surface conductivity is small due to the $1/\kappa a$ prefactor in Eqn. 1.10. The ratio of permittivities of the particles to the suspending medium also fortuitously acts to reduce the influence of the $(1+f)$ factor in the dynamic mobility. That is, the function f contains terms with factors of ϵ_p/ϵ, where ϵ_p is the particle permittivity. This ratio is typically small for water based suspensions, and thus the terms containing this ratio in the f function are negligible. Most water based colloids with thin double layers have $f = 0.5$ [24]. In this case, the variations in magnitude and argument of the dynamic mobility with

the frequency of the electric field arise wholly from the G function.

While the theory describing the electroacoustic effect for dilute suspensions with thin double layers is useful for measuring the zeta-potential and hydrodynamic size of colloids suspended in optically dense media, it is still lacking in its ability to treat concentrated suspensions. It is still possible to measure the electroacoustic effect produced by concentrated colloids with moderate and thick double layers, although mapping these results to particle size and zeta-potential is challenging. This is of particular concern for nanoparticle suspensions as these typically have moderate double layer thicknesses (see Fig. 1.2) and have varying concentrations for use in application. Thus, an extension of the theory of dynamic mobility to concentrated samples with different double layer thickness would be invaluable for determining the surface properties of a nanoparticle formulation and ultimately allow for an assessment of their effectiveness for a particular biomedical application.

In order to extend the electroacoustic method to more concentrated samples and those with thick double layers requires different theoretical models of the dynamic mobility. Various attempts have been made to develop the theory of dynamic mobility to increase the scope of the electroacoustic technique. These methods include a coupled phase model that describes the relative motion of the particles and liquids along with a cell model concept that accounts for electro- and hydrodynamic forces [29], [30]. The coupled phase model was developed essentially from an expression of Newton's second law which includes contributions from a pressure differential and

viscous drag forces, originally developed to describe the colloid vibration potential. This model has been used successfully for determining the attenuation of acoustic waves in colloids [31], [32]. Derivation of this model requires no assumptions about particle concentration and thus can be applied to colloids of any volume fraction. The cell model concept was developed by a similar method to Eqn. 1.9 [30]. Here, each particle, along with a spherical shell of suspending medium, is considered a separate element. Interparticle interactions are included by using appropriate boundary conditions and overlapping double layers are also considered. This model has been successfully mapped to electroacoustic measurements of colloids with a hydrodynamic size of 0.35 μm up to a volume fraction of 43 % w/v [30].

1.3 Previous work using electroacoustic measurements

To show the validity of the electroacoustic method, it will be useful to survey the literature for successful use of the technique for determining the surface properties of **micrometre-sized** colloidal samples. The first electroacoustic apparatus was not able to determine concurrently both particle size and zeta-potential because it was limited to only a single frequency [33]. The derivation of a theory for electroacoustic effects in dilute suspensions of spherical particles by O'Brien in 1988 [24] allowed for the development of a new design of electroacoustic apparatus which could measure

over a range of frequencies. This development culminated in the work of O'Brien et al. [25] who presented the first experimental evidence of size and zeta-potential determination from electroacoustic measurements. Figure 1.8 shows the first measurement of the dynamic mobility for 0.30 μm colloidal silica particles suspended in water with the addition of potassium chloride as an electrolyte. Electroacoustic measurements were also performed on colloidal spheres of titanium dioxide (0.35 μm), alumina (0.48 μm), calcium carbonate (2.3 μm) and aluminium hydroxide (0.58 μm). The determined size distributions were compared with those obtained by light scattering techniques and showed agreement within 5 %.

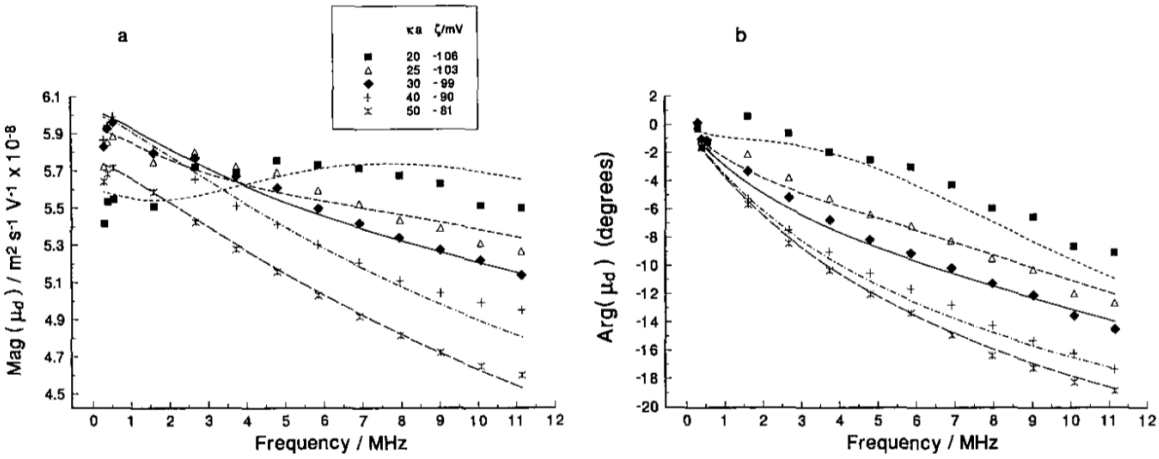

Figure 1.8: Magnitude (a) and argument (b) of the dynamic mobility obtained for colloidal silica at five different electrolyte concentrations (corresponding to five double layer thicknesses). The curves are fits to the thin double layer theory [25].

Hackley and Malghan [34] used electroacoustic measurements to assess the zeta-potential as a function of pH on colloidal silica samples with a hydrodynamic di-

ameter of 0.4 μm. Their results were compared with zeta-potentials determined by electrophoresis measurements and showed excellent agreement. Electroacoustic measurements have highlighted also previously unobserved effects in emulsions such as skim milk, which contains suspensions of the protein casein in a high electrolyte concentration. Wade et al. [35] showed with electroacoustic measurements a change in the zeta-potential of the suspended casein protein (0.2 μm average size) from -18 mV to -11 mV when the sample pH was lowered, with an accompanying five-fold increase in hydrodynamic size. While the change in zeta-potential was easily explained within the current theory, the size increase was not previously observed by light scattering measurements. It was suggested that this occurred due to the necessary dilution of the sample required for light scattering measurements which masked the apparent aggregation of the casein micelles. This work also confirmed the validity of subtracting the electroacoustic signal of the electrolyte to reveal only that of the suspended particles; the casein protein has a density very close to water and thus the electrolyte dominated the electroacoustic signal.

Dukhin and Goetz [36] have used the electroacoustic method to determine changes in the zeta-potential and hydrodynamic of colloidal alumina (2 μm median diameter) and rutile (0.3 μm median diameter) with pH. They also quantified the accuracy and precision of the technique for determining zeta-potential by performing repeated measurements on the same sample, quoting an accuracy of several mV and a precision of around 0.5 mV. More recently, the electroacoustic technique has been used to

monitor aggregation of dense silica suspensions under agitation. Tourbin and Frances [37] measured 30 % w/w silica suspensions on-line under constant agitation. For this particular colloid, it was determined that the dilution of the sample required for measurement with light scattering techniques had no affect on the aggregation process with changing electrolyte concentration. Electroacoustic measurements have also been used successfully to measure the surface properties of mixed mineral systems. Klein et al. [38] determined that the electroacoustic theory accurately predicts the zeta-potential of mixed systems where the species have similar sizes. They found that for mixed systems where the species had vastly different sizes and zeta-potentials of opposite sign, this mapping was not accurate as there was increased interparticle interactions between the different species leading to aggregation.

While it is clear that electroacoustic technique has been used successfully for the determination of hydrodynamic size and zeta-potential of colloidal suspensions with median particle diameters $\geq$ 200 nm, no study of nanoparticle surface charge and hydrodynamic size has been performed using the electroacoustic method. Therefore, extending the electroacoustic technique to measure successfully nanoparticle surface charge and hydrodynamic size in suspension presents a promising opportunity for developing a basic understanding of the effects that biologically relevant media have on nanoparticle surface properties.

Chapter 2

Experimental techniques

In order to use successfully the electroacoustic method for assessing nanoparticle surface charge and hydrodynamic size requires an understanding of the reasoning and assumptions used in the construction of the electroacoustic apparatus. The following sections contain a detailed discussion regarding the required elements for electroacoustic measurements and the reasoning used for the selection of particular components along with a description of the construction of the electroacoustic apparatus. This chapter includes also a discussion of the various experimental techniques used (e.g. dynamic light scattering) in quantifying the nanoparticle suspensions for comparison with the electroacoustic measurements. Finally, a description of the nanoparticle suspensions used for the various measurement techniques is provided.

2.1 Electroacoustic cell design considerations

The electroacoustic cell consists essentially of a closed volume containing parallel electrodes for applying a spatially uniform electric field and a means of measuring the produced compression waves. Measurement of the acoustic signal is accomplished using transducers which convert mechanical energy to electric charge that can be amplified and recorded. Transducers are composed typically of a piezoelectric material which possesses a microstructure that produces electrical energy under mechanical strain. Conversely, if an electrical potential is applied to a piezoelectric material, strain is induced in the microstructure [39]. Thus, an ultrasound transducer acts as both a generator and receiver of ultrasound waves. Various piezoelectric materials exist, e.g. ceramic materials which possess regular crystal structure. It is also possible to induce piezoelectric properties in polymers by orientation; that is, by promoting a polarizable phase of the polymer which responds to both mechanical and electrical energy. The first polymer shown to have piezoelectric behaviour was polyvinylidene fluoride [40], which was the material chosen for the construction of the transducer used in the electroacoustic apparatus.

As a piezoelectric transducer responds not only to mechanical energy but to changes in electrical potential, elements must be added to the cell in order to separate the desired acoustic signal resulting from the sample, and the electrical response of the transducer to the applied voltage at the electrodes. For this purpose, two quartz delay rods of sufficient length are added to either end of the cell which introduce a $\sim$

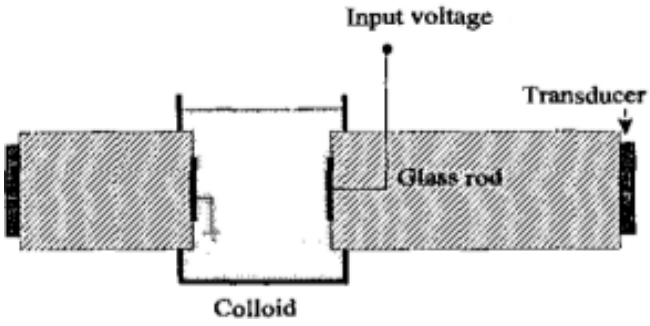

Figure 2.1: A schematic of the electroacoustic cell [25].

5 μs delay from signal generation to detection. The delay in detection arises due to the length of time required for a compression wave to propagate down the delay rod. For example, an ultrasound wave will pass through a 1 cm length of quartz[1] in 1.7 μs. This delay, in combination with a pulsed voltage applied to the electrodes (with duration < 5 μs) is expected to allow sufficient time for the separation of the electrical pickup and desired signal. These delay rods provide also a convenient location to position the electrodes for the generation of the largest compression waves from the sample, as discussed previously. A simple schematic of an electroacoustic cell is shown in Fig. 2.1 [25].

For an ideal cell, the measuring transducer will detect three separate signals. The first, as discussed previously, is a consequence of the transducer's response to the applied voltage (electrical cross-talk). The second detected signal emanates from the sample and is generated at the electrode closest to the measuring transducer.

[1]The velocity of a compression wave through quartz is a constant 5900 m s^{-1} [41]. The propagation time is equal to the distance travelled over the constant velocity of the compression wave

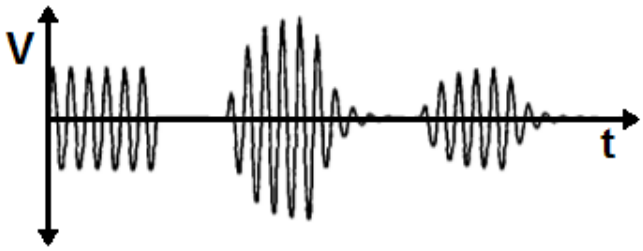

Figure 2.2: The response of a single transducer after a sinusoidal burst potential is applied to the cell electrodes, showing only the initial electrical cross-talk and the electroacoustic signal produced by the sample [25].

The third signal is also from the sample, but is generated at the opposite electrode, having travelled through the sample cell then into the delay rod. Each signal can be separated sufficiently by selecting appropriate lengths of the delay rods and the thickness of the cell (distance between delay rods). The medium contained within the cell acts also to vary the propagation time of compression waves through the cell and must be accounted for. A schematic representation of the signal detected by a single transducer is shown in Fig. 2.2 [25].

Selecting the width of the electroacoustic cell is not only a means of separating the signals produced by the sample, but also prevents the washing out of the signal by possible reflections of undesired compression waves. That is, as a consequence of the response of the transducers to the initial applied voltage, compression waves propagate down the delay rods towards the cell. The acoustic signal generated from the electrical pickup will both transmit into the cell and reflect at the delay rod

interface. The reflected signal will propagate back down the delay rod and be detected by the transducer. Detection of the reflected signal will occur at ~ 10 μs (twice the delay for a single transit down the quartz rod). Thus if the cell thickness provides only 5 μs of delay, the signal generated by the sample at the far electrode would be completely dominated by the reflections.

It is important to discuss the effect that the delay rods have on the produced electroacoustic signal. The delay rod and the cell filled with suspension have an acoustic impedance which do not match. That is, there is an impedance mismatch the delay rod-to-suspension interface that prevents all the acoustic energy in the suspension from being transmitted into the delay rod. The theory on which the electroacoustic effect is based is simplest for this configuration as the electrode dimensions are much larger than the particle size [42], as the pressure waves can be treated as planar at the electrodes. This gives ultimately the electroacoustic signal [25]

$$EA = A\phi\frac{\Delta\rho}{\rho}\langle\mu_D\rangle E\frac{Z_s}{Z_s + Z_r} \tag{2.1}$$

where $\langle\mu_D\rangle$ is the particle averaged dynamic mobility, A is a constant which takes into account the properties of the measuring transducer and electronics, and Z_s and Z_r are the acoustic impedances of the suspension and delay rod, respectively. While for dilute suspensions, the acoustic impedance of a colloid can be taken simply as the impedance of the suspending medium, Z_s becomes a function of the properties of the particles in suspension for increasing concentration. Thus, this quantity must

be measured for concentrated samples in order to acquire an accurate electroacoustic signal. Z_r can be treated as a constant, as the acoustic impedance of quartz is not affected by different suspensions.

It is possible to measure the acoustic impedance of the suspension by means of the second transducer. As opposed to applying the pulse voltage to the electrodes which flank the cell, this potential is applied to the transducer not used in measurement which generates a compression wave that propagates down the delay rod toward the suspension. Part of the acoustic wave is reflected at the delay rod-sample interface. The fraction of the amplitude that does reflect is given by the reflection coefficient, R_s

$$R_s = \frac{Z_r - Z_s}{Z_r + Z_s} \tag{2.2}$$

and

$$1 - R_s = \frac{Z_s}{Z_r + Z_s} \tag{2.3}$$

which is the dependence on the acoustic impedances in Eqn. 2.1. Using also the fact that the acoustic impedance of air is very small when compared with the impedance of water, it can be assumed that the reflection coefficient given by Eqn. 2.2 is effectively unity when the cell is empty. Therefore, the quantity $1-R_s$ can be treated as the difference between the reflected signal for an air-filled cell and one filled with a colloid (R_a - R_s). The dependence of Eqn. 2.1 on the acoustic impedance can be

eliminated by dividing the electroacoustic signal by $S_a - S_s$, where S is the Fourier transform of the reflected signal, namely [25]

$$\frac{EA}{S_a - S_s} = B\phi\frac{\Delta\rho}{\rho}\langle\mu_D\rangle E \tag{2.4}$$

This remaining unknown factors are $\langle\mu_D\rangle$, which is the quantity to be measured, and B, which is a modified instrument parameter depending on the properties of the transducer and the measurement electronics. The instrument constant B is a function of a frequency and to some degree, the conductivity of the cell; large changes in cell impedance can lead to difficulties in applying an electric field with a fixed magnitude from sample to sample. The instrument constant B can be determined by measuring the electroacoustic signal of a colloid with known dynamic mobility over a range of frequencies. It can also be determined by measurement of an electrolyte which should provide a consistent mobility that can be determined from known properties of the ionic species of the electrolyte [25].

2.2 Cell construction

The first step in constructing the electroacoustic measurement cell was selecting a transducer with an appropriate frequency response. The G function shown in Fig. 1.7 determines what range of electric field frequencies would show the largest changes in dynamic mobility for colloids with thin double layers. From this and the sizes of nanoparticles to be measured (10 - 500 nm diameters), a transducer with a frequency

response centred around 10 MHz is desirable. For this purpose, a polymer piezoelectric transducer was selected. The chosen transducer is fabricated from polyvinylidene fluoride, with a thickness of approximately 50 μm (Atochem, Norristown, PA). The characteristic frequency response of a polymer transducer is determined by the thickness of the material and the velocity at which ultrasound propagates through the material. Resonance occurs when the piezoelectric film thickness is equal to one half wavelength of the ultrasound wave propagating through the material [43]. The longitudinal mode of ultrasound through polyvinylidene fluoride has a velocity of 2200 m/s. Thus, three layers of 50 μm thick polyvinylidene fluoride has a characteristic frequency of $\sim$ 7.5 MHz.

The delay rods were fabricated from UV grade fused silica (Laboratory Optical Co., Sturbridge, MA), with a length of 2.85 cm (1.12 inches) and a diameter of 1.26 cm (0.5 inches). The rod ends are parallel to within 5 μm, perpendicular to the rod axis to within 1 μm, and polished flat to within four fringes (1.26 μm for light with a wavelength of 600 nm). One end of each delay rod is plated with a 500 nm thick gold electrode on top of a chromium binder. Three separate layers of the polymer transducer were fixed to the unplated end of two delay rods using a two-part epoxy (Stycast 1266, Emerson and Cuming, Billerica, MA). The layers are connected mechanically in series and electrically in parallel. The electrical contact on the transducer layer closest to the delay rod was grounded electrically using silver paint and the outermost layer was connected to a coaxial cable by means of a spring

loaded contact. The ends of the delay rods that have electrodes attached are secured in split ring clamps that are meant to hold them in place and also provide a means of connecting the delay rod assemblies to the sample containing cell.

The first version of the sample cell was constructed from an aluminium slab of $\sim$ 6.5 mm thickness. A cylindrical hole of 1.26 cm (0.5 inch) diameter was machined into the centre of the aluminium. In this configuration, there was not sufficient clearance for securing leads to the electrodes in order to apply an electric field, and thus this cell was used only in the characterization of the transducer response. To address the clearance issue of the aluminium sample space, a second cell was fabricated from acrylic. Acrylic was selected for ease of fabrication and because it provides sufficient chemical resistance to the suspending fluids used. The geometry used was a cylindrical shell with an inner diameter of 1.9 cm, an outer diameter of 3 cm and an overall length of 3 cm. The delay rods were inserted $\sim$ 0.5 cm into the cell for an overall separation of 1.9 cm. Two large holes were drilled along the diameter in the middle of the acrylic cylinder to allow for sample to be added and subsequently drained from the sample cell. Two smaller holes were made along the cylinder diameter near the ends of the cell to allow electrical contacts to be run to the electrodes. This configuration allowed for changes in the separation of the electrodes by adjusting the placement of the delay rods in the split ring clamps. Figures 2.3 and 2.4 are photographs of the final configuration of the electroacoustic cell.

The connections to the electrodes were made using thin copper foil cut into a

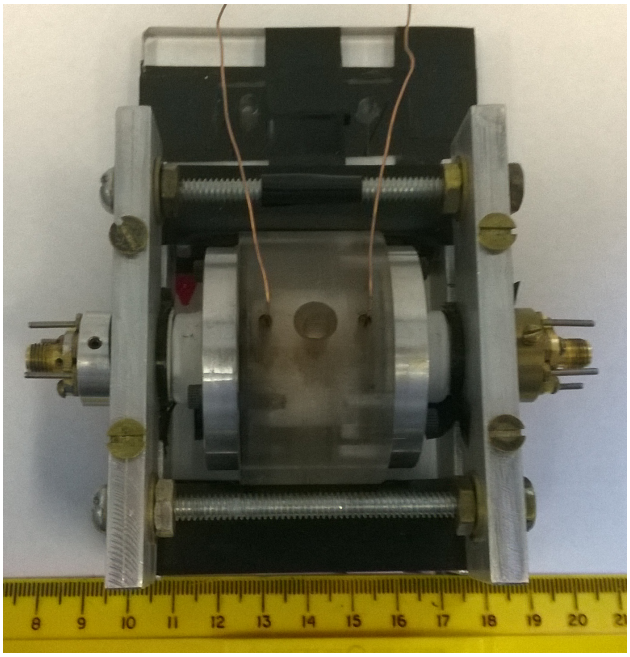

Figure 2.3: Photograph of the constructed electroacoustic cell.

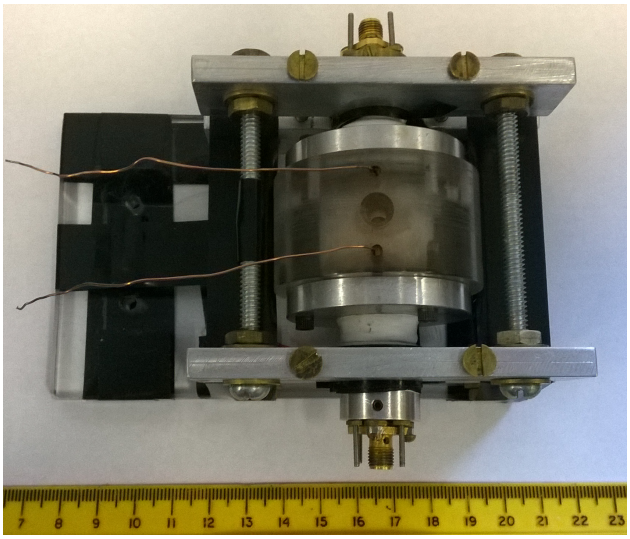

Figure 2.4: Photograph of the constructed electroacoustic cell.

'T' shape, approximately 1.5 cm across and 1 cm in height. The largest dimension was attached using cyanoacrylate glue to the outside of the delay rod for mechanical stability. A small length of insulated copper wire was also soldered to this portion of the electrode contact so that it could be connected to the electronics which provide the applied potential. The remaining copper foil was bent over the edge of the gold plated end of the delay rod. A thin layer of silver paint was used to provide an electrical connection between the electrode and the contact. Effort was made to decrease the size of this portion of the contact and to use as little electrically conductive paint as possible in order to minimize deviations from perfectly parallel electrodes.

2.3 Measurement electronics

Characterization of the transducer response required only two pieces of electronics; a pulser and an oscilloscope for recording the output. The pulser is a versatile component for many ultrasound experiments; it provides the various elements necessary for quantification of an acoustic system. Its primary functionality is to provide an electrical pulse, typically used to produce compression waves from a transducer. The pulser used (Panametrics 5058PR, Olympus Co.) provides a variable pulse voltage and damping, along with several different repetition rates. This device can operate in reflection and transmission modes. The reflection mode measures the response of the transducer that the pulse voltage is applied to, while the transmission mode can be used to measure the response of a second transducer in the acoustic system. In both

configurations, the signal was passed through a receiving amplifier with adjustable gain and attenuation along with variable low- and high-pass filters. The amplified signal was then used as output to be recorded with an oscilloscope. The pulser provided also a timing signal which was used to set the oscilloscope trigger. Characterization of the two transducers used in the electroacoustic apparatus was performed in both transmission and reflection modes with fixed pulse and amplification settings

The electronics required to produce and measure an electroacoustic signal from a colloid can be thought of simply as an input and output. The input electronics provide the stimulating electric field while the output side allows for measuring and recording of the produced signal. The measurement side of the system consists solely of an amplifier and an oscilloscope (Tektronix TDS5032B, Tektronix, Beaverton, OH). Amplification of the output signal was provided by the receiving amplifier contained within the previously mentioned pulser.

The equipment providing the electrical input signal has gone through a number of configurations. Initially, input was provided by a simple function generator (General Radio 1269-A, General Radio Co., Concord, MA) with sinusoidal output capable of frequencies ranging from 0.5 to 50 MHz. Output voltage was controllable by a variable resistor which adjusted the output impedance. No amplification was used for this configuration and thus the applied potential was limited to $\sim$ 1 V peak-to-peak. The function generator was then replaced with an arbitrary waveform generator (Agilent 33220A, Agilent Technologies, Santa Clara, CA) which was used in burst

configuration. This instrument provided an n-cycle sinusoidal output over a frequency range of 0.1 to 10 MHz, with magnitudes up to 20 V peak-to-peak. The burst period (number of bursts per second) was also adjustable. A burst period of 50 ms was used for most measurements allowing an acoustic wave to complete at least ten transits of the cell. A timing output was available also for triggering the measuring oscilloscope.

The same arbitrary waveform generator was used also in conjunction with a broad-band radio-frequency amplifier (Electronics and Innovation 2200L, Electronics and Innovation Ltd., Rochester, NY) that provided a constant gain of 50 dB. Input to the amplifier was limited to $\sim$ 500 mV peak-to-peak in order to prevent damage to the

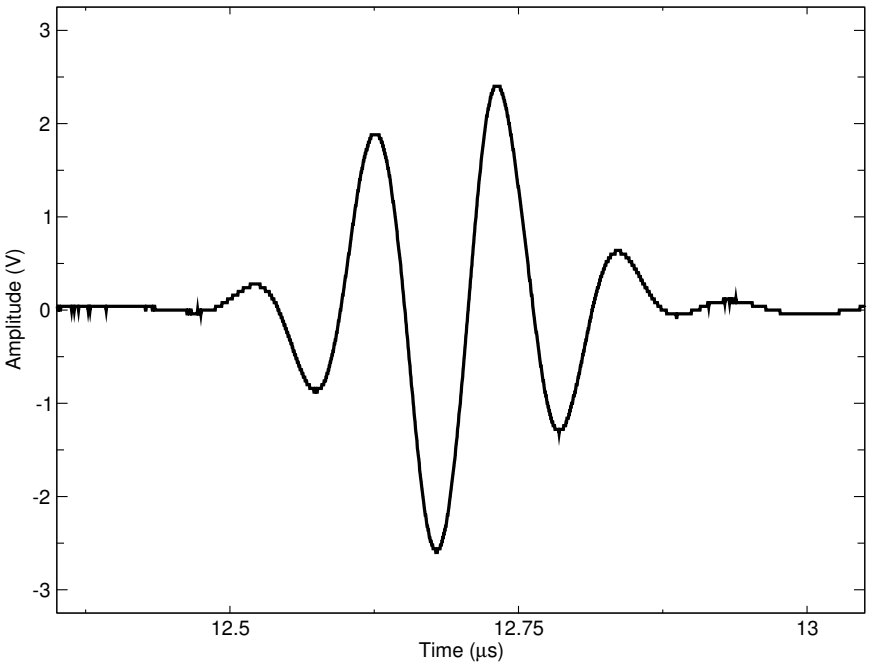

Figure 2.5: The damped sine wave potential, Gauss2, at a frequency of 9 MHz, applied to the electrodes for the final configuration of the electroacoustic apparatus.

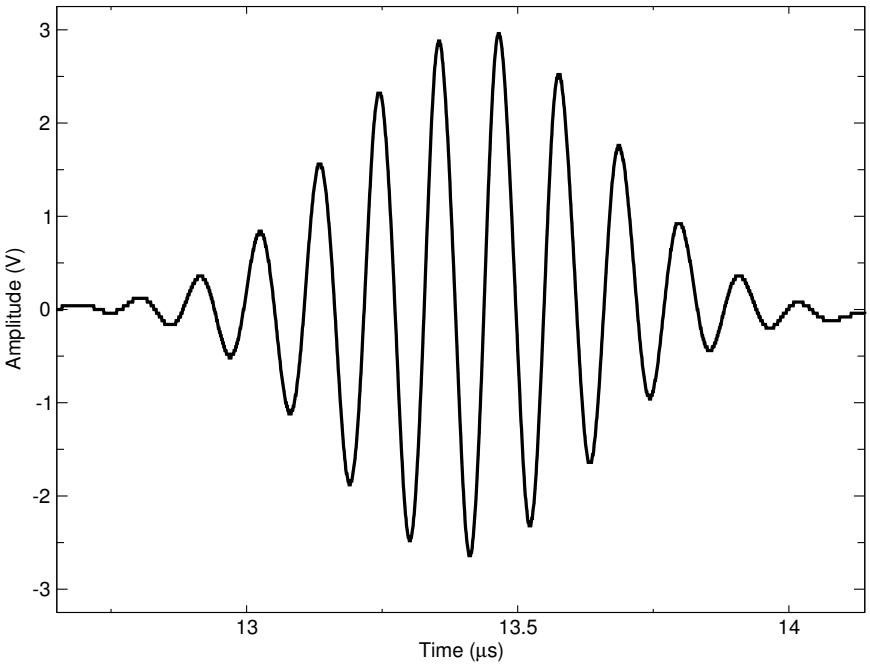

Figure 2.6: The damped sine wave potential, Gauss6, at a frequency of 9 MHz, applied to the electrodes for the final configuration of the electroacoustic apparatus.

electrode contacts. The final configuration the arbitrary wave form generator which allowed for the application a sinusoidal burst convoluted with a Gaussian distribution, outputting effectively a damped burst pulse. The two potentials applied to the electrodes are shown in Figs. 2.5 and 2.6. In this case, amplification was provided by a gated radio-frequency amplifier (Ritec GA-2500A, Ritec Inc., Warwick, RI) with variable gain. As this amplifier has a limited duty cycle ($\sim 1\%$), a digital delay (Stanford Research Systems DG535) with multiple output triggers was required. The gated amplifier was triggered over a 49 μs interval, with a repetition rate of 40 Hz. The start of the burst potential was triggered 12 μs after the start of the amplification window

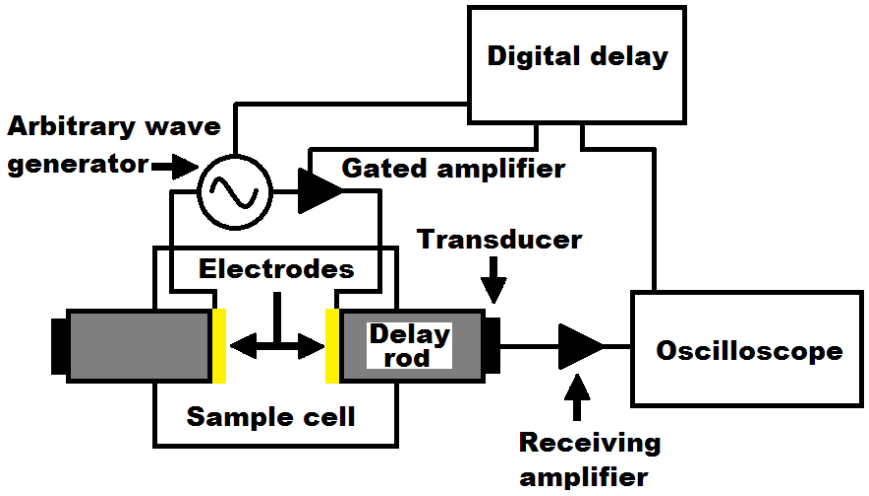

Figure 2.7: A schematic of the electroacoustic cell with the electronics used for measurements.

and was used also as a trigger to begin measurement with an oscilloscope. Figure 2.7 shows a schematic of the electronics used in the electroacoustic measurements.

2.4 Dynamic light scattering

The most widely used method for assess the size of particles in liquid suspension through a measure of their hydrodynamic radius is dynamic light scattering [44]. In light scattering measurements, a coherent and monochromatic source is incident on a scattering volume. If the particles are smaller than the wavelength, λ, of the incident beam, light is scattered isotropically (Rayleigh scattering) [8]. The scattered light intensity can then be recorded by a detector at a scattering angle θ. Dynamic light scattering probes time varying effects in a sample by measuring the scattered

light intensity over a range of time scales. As particles in liquid suspension undergo stochastic motion due to kinetic interactions with the suspending medium, the scattered light intensity at a fixed detector angle is expected to fluctuate. The mean square displacement, s, of this random motion over a time interval t is given as [45]

$$\langle s^2 \rangle = 2Dt = \frac{2k_B T}{f_{drag}} t \tag{2.5}$$

where f_{drag} is a retarding force provided by the suspending medium and D is the associated diffusion constant. In the case of linear diffusion of spherical particles, the drag force takes the form $f_{drag} = 6\pi\eta a$ [8] and thus the diffusion constant is

$$D = \frac{k_B T}{6\pi\eta a} \tag{2.6}$$

It is clear from Eqn. 2.6 that the hydrodynamic size of a particle in suspension is attainable through the diffusion constant assuming the dynamic viscosity of the suspending medium is known. The diffusion constant is obtained through dynamic light scattering experiments by means of an intensity autocorrelation function [8], $g(t)$, the form of which is shown in Fig. 2.8. Put simply, the scattered light intensity at time t_i is correlated with the same quantity at an earlier time, t_0. The simplest approach is to relate the autocorrelated light intensity to a single exponential decay, $g = e^{-\Gamma t}$, where Γ is related to the diffusion constant through the square of the scattering vector, q, given by [8]

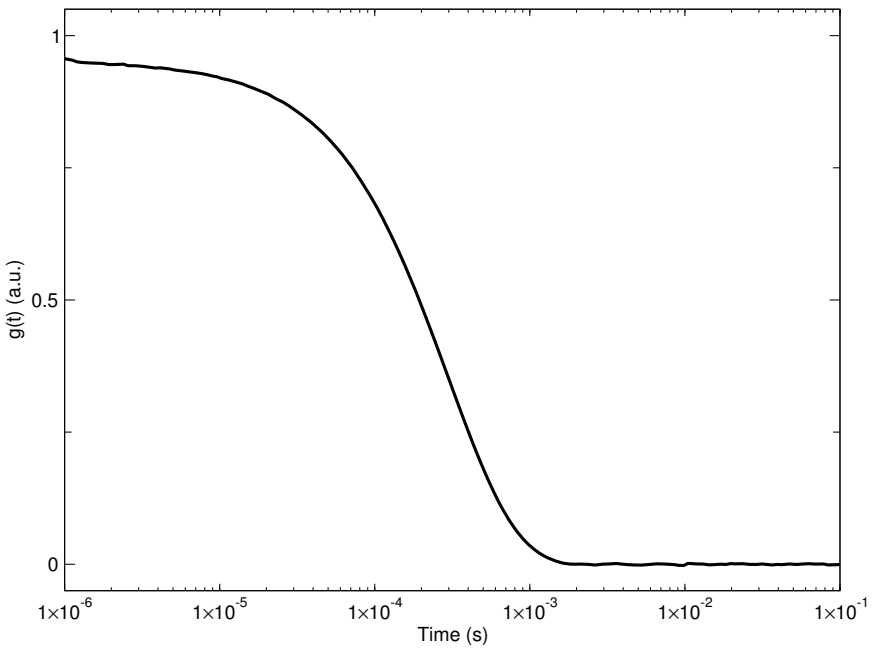

Figure 2.8: The form of the autocorrelation function, $g(t)$.

$$q = \frac{4\pi n}{\lambda} sin\left(\frac{\theta}{2}\right) \tag{2.7}$$

where n is the refractive index of the suspension. The particle size in suspension is obtainable through

$$g(q,t) = e^{-q^2 Dt} \tag{2.8}$$

It is important to note that this method of determining particle size from the autocorrelation function obtained by dynamic light scattering experiments requires single scattering. That is, the autocorrelation function does not account for multiple scattering events [8]. Thus using dynamic light scattering for particle size determina-

tion requires dilute suspensions with concentrations typically below 1 % v/v (volume of particles over total suspension volume). More complex measurement methods are available for multiple scattering experiments (i.e. more concentrated samples) but the analysis used for interpreting these measurements is highly sample dependent, requiring knowledge of the sample structure factor [8].

Dynamic light scattering measurements were performed using a Photocor FC complex (Photocor Instruments Inc., College Park, MD) photon correlation spectrometer, shown in Fig. 2.9. The photo multiplier tube used to measure the scattered light intensity is mounted on an arm which allows for variation of the scattering angle. Autocorrelation functions were obtained at scattering angles of 60°, 90° and 120°. Collecting autocorrelation functions at multiple scattering angles is advantageous in that non-spherical particles can be identified by changes in the form of the hydrodynamic size distribution as a function of the scattering angle [8].

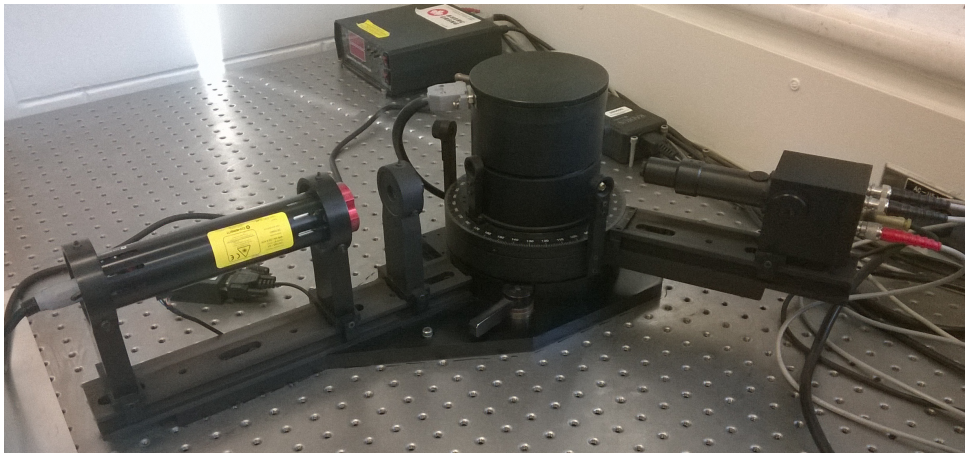

Figure 2.9: A photograph of the Photocor FC complex photon correlation spectrometer.

2.5 Impedance measurements

A magnetic nanoparticle can be described simply as a sub-magnetic-domain-sized particle, such that its constituent magnetic moments act cooperatively and thus can be treated as a single large magnetic moment having a uniaxial anisotropy. That is, the net magnetization can lie along one of two energetically favourable anti-parallel directions separated by an energy barrier set by the particle volume and its anisotropy. If a collection of nanoparticles are aligned in a magnetic field which is subsequently removed, the overall magnetization of the system will relax by two mechanisms. The first, Néel relaxation, involves the thermally activated reversal of the particle's magnetic moment through the energy barrier separating the two easy-axes of magnetization [46]. The Néel relaxation mechanism has a characteristic reversal time, τ_N given by

$$\tau_N = \tau_0 \exp\left(\frac{KV_m}{k_B T}\right) \tag{2.9}$$

where K is the particle anisotropy, V_m is the magnetic core volume and τ_0 is the attempt time, depending both on the measurement conditions and the sample being probed.

The second mechanism is through rotational diffusion, occurring only in liquid suspension, where kinetic interactions from the suspending medium act to rotate the particle as a whole while the magnetic moment remains fixed relative to the particle. The rotational diffusion of a particle has a characteristic time for reversal, τ_B, given

by [47]

$$\tau_B = \frac{1}{2\pi f_B} = \frac{3V\eta}{k_B T} \tag{2.10}$$

where V is the hydrodynamic volume of a spherical particle. Rotational diffusion occurs typically on time scales much larger than Néel relaxation and is often separated sufficiently in frequency such that the two relaxation mechanisms can be determined independently.

The magnetic relaxation of a collection of magnetic nanoparticles can be tracked through measurements of their complex susceptibility, relating the magnetization of a material to an applied magnetic field. The frequency dependent complex susceptibility is given by [48]

$$\chi = \chi'(\omega) - i\chi''(\omega) = \chi_0 \left[\frac{1}{1 + (\omega\tau)^2} - i\frac{\omega\tau}{1 + (\omega\tau)^2} \right] \tag{2.11}$$

where τ is an effective relaxation time and $\chi_0 = \mu_0 n m^2 / 3k_B T$ is the static susceptibility in zero field, depending on the magnetic moment of a single nanoparticle, m, the nanoparticle number density, n, and μ_0 is the permeability (magnetization per unit magnetic field) of free space.

Fannin et al. [49] have developed a technique by which the relaxation behaviour in a suspension of magnetic nanoparticles is measured through a change in impedance of an inductor. That is, a small slit of width L_1 (which acts as a sample space) is cut in a toroidal inductor with magnetic path length L_2. The nanoparticle permeability

can be determined by measuring the impedance of the inductor with the slit empty and filled with a nanoparticle suspension. The inductance of the empty (Z_{ce}) and full (Z_{cf}) inductor is given by

$$Z_{ce} = R_w + i\omega\alpha L_0 \left(\frac{\mu_r}{1 + \gamma/\mu_r} \right) \ , \ Z_{cf} = R_w + i\omega\alpha L_0 \left(\frac{\mu_r}{1 + \gamma\mu_r/\mu_l} \right) \tag{2.12}$$

where R_w is the resistance of the inductor windings, μ_r and μ_l are the relative (complex) permeability of the toroid and the nanoparticle suspension, respectively, L_0 is the inductance of an air coil with the same dimensions as the toroid, $\alpha = (L_1 + L_2)/L_2$ and $\gamma = L_1/L_2$. As the susceptibility is related directly to the permeability, measuring the inductor impedance over a range of frequencies allows a determination of the frequency dependant complex susceptibility of a nanoparticle suspension.

This technique requires simply a broadband network analyser (Agilent 4294a,

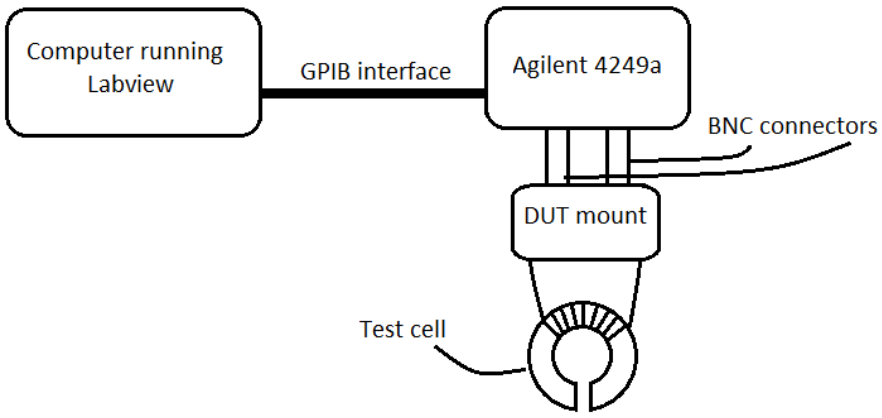

Figure 2.10: Block diagram of the instruments used for the impedance technique.

Agilent Technologies,Santa Clara, CA) capable of measuring the complex impedance of any device, a means of data logging and the test cell itself. A schematic of the instrumentation required for measuring magnetic nanoparticle susceptibility is shown in Fig. 2.10.

2.6 Particle suspensions

2.6.1 Latex spheres

In order to assess the effectiveness and accuracy of the electroacoustic method in determining the surface properties of colloidal suspensions required the use of particles with well defined size and surface charge. For this purpose, polystyrene (latex) spheres in water suspension that are used typically in calibration of scanning electron microscopes were purchased (Alfa Aesar, Ward Hill, MA). These calibration spheres are particularly useful in that their zeta-potential does not depend strongly on the particle size within a given theoretical framework, as shown in Fig. 2.11 [50], and thus allow for determination of particle size effects on the electroacoustic measurement. The latex spheres chosen have diameters of 100 nm, 210 nm, 500 nm and 850 nm, providing a meaningful range of sizes for testing the apparatus. It is important to note that although the latex calibration spheres are well defined in size and zeta-potential, their density is only 0.9 - 1.1 kg m^{-3} [51]. Thus, the the factor $\Delta\rho/\rho$ is approximately 0.1, leading ultimately to a small electroacoustic signal.

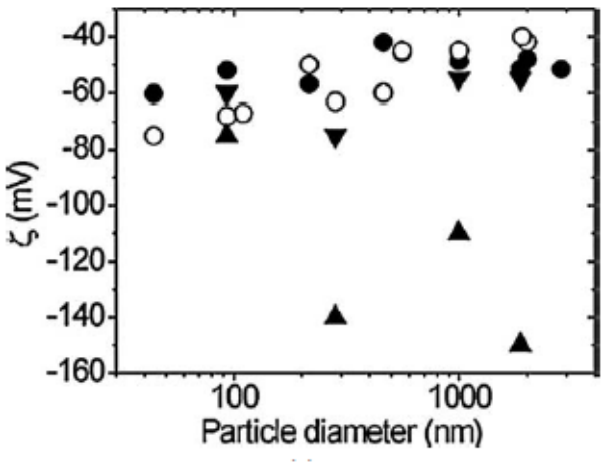

Figure 2.11: zeta-potential for latex spheres of various size determined by AC dielectrophoretic measurements interpreted in three different theoretical models of electrokinetic properties [50].

2.6.2 Nanoparticle suspensions

Various nanoparticle systems were used in this study. Magnetite "nanochips" were synthesized from an iron-acetate precursor using a one-pot technique [52] by collaborators at Kent State University. The shape of these nanochips was determined to be plate-like and not spherical. These particles were conjugated with an ethylenediaminetriacetic acid complex (EDT NC). Initial characterization by dynamic (particle size) and phase analysis light scattering (zeta-potential) of these particles by the group at Kent State determined a hydrodynamic radius of $\sim$ 30 nm and a zeta-potential in deionized water of -40 mV. These nanochips were received in water suspension and additional dilutions were performed with deionized water.

An additional magnetite nanoparticle formulation was used. These nanoparticles were synthesized by the group at Kent State using a similar technique as the ethylenediaminetriacetic acid coated magnetite nanochips. These nanoparticles are made as uncoated spheres with a diameter of 20 nm and are coated post synthesis with aminosilane (AmS nanoparticle). Initial characterization of the coated nanoparticles performed using light scattering techniques by the group at Kent State revealed a hydrodynamic diameter of 25 nm and a zeta-potential of 21 mV for the AmS nanoparticle.

Cobalt ferrite nanoparticles (CoFe nanoparticle) were synthesized in-house from ferric and cobalt chloride salts using a co-precipitation technique [53]. Oleic acid was used as a capping agent, and acted to halt growth of the particles. The synthesis involves a drying step and thus produces nanoparticles as a powder. This powder was suspended in propanol for dynamic light scattering and electroacoustic measurements. The diameter of CoFe nanoparticles synthesized by this technique is expected to be 15 - 50 nm.

Gold nanoparticles (Au nanoparticle) were synthesized in-house using a nonhydrolytic single-precursor technique [54]. The synthesis method involves essentially injecting the metal precursor into a hot (250 - 300 °C) long-chain amine (octylamine) which acts as a surfactant. Nanoparticles synthesized by this technique are expected to have diameters ranging from 6 - 10 nm. Gold nanoparticles were suspended in hexanes for dynamic light scattering and electroacoustic measurements.

Finally, measurements were also performed on Lignosite (Georgia Pacific, Augusta, GA), a commercially manufactured magnetite nanoparticle suspended in an organic oil. These nanoparticles were diluted in deionized water which formed stable suspensions.

Table 2.1: Summary of the samples used for measurements.

Sample	**Label**	**Medium**	**Radius (nm)**	ζ **(mV)**	**Density (10^3 kg m^{-3})**
100 nm latex	100 nm	water	50	-60 [50]	0.9-1.1 [51]
210 nm latex	210 nm	water	105	-60 [50]	0.9-1.1 [51]
500 nm latex	500 nm	water	250	-60 [50]	0.9-1.1 [51]
850 nm latex	850 nm	water	425	-60 [50]	0.9-1.1 [51]
EDT NC	NC	water	30	-40	5.2 [55]
AmS NP	NP	water	12.5	21	5.2 [55]
Au NP	Au	hexanes	3-3.5 [54]	-	18.8 [56]
CoFe NP	CoFe	propanol	15 - 50 [53]	-	5.3 [57]
Lignosite	Lig	water	-	-	5.2 [55]

Chapter 3

Cell characterization

Before the electroacoustic apparatus can be used for measuring the surface properties of nanoparticles in liquid suspension, a characterization of the constructed electroacoustic cell is required. The following section discusses quantification of the transducers used for the electroacoustic apparatus, along with a description of the cell properties, e.g., the delays in detection associated with the width of the various components of the electroacoustic cell and the electrical properties of the cell as a whole.

3.1 Transducer response

Initial characterization of the transducers was performed with the electroacoustic apparatus that contained the 6.5 mm thick aluminium cell. A compression wave was produced at one transducer using a short pulse of 100 V with a 20 Hz repetition rate,

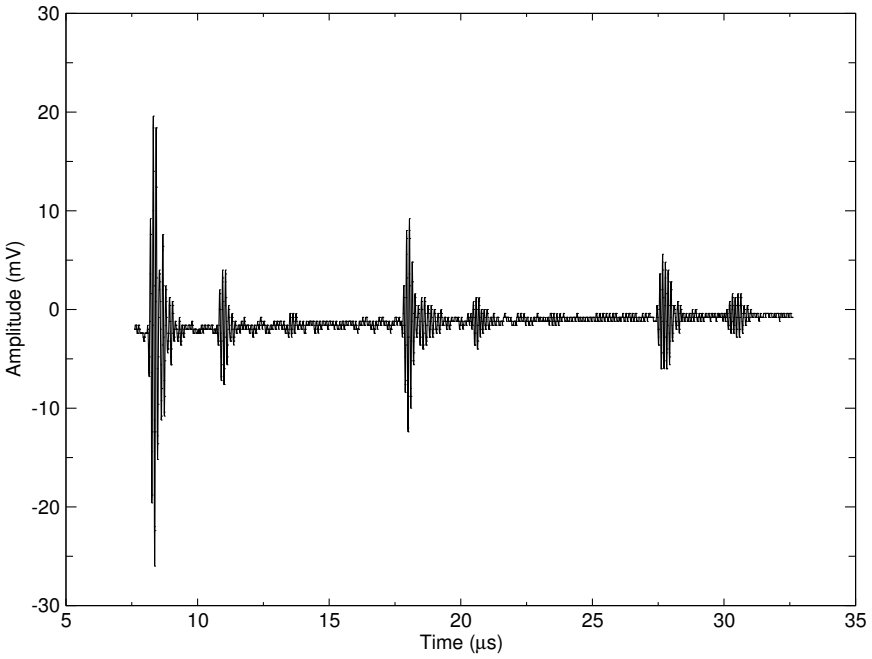

Figure 3.1: Response of transducer attached to delay rod #1 in reflection mode.

corresponding to a period of 50 ms. This period provided sufficient time to observe at least ten full transits of the compression wave through the cell. The receiving amplifier provided 60 dB of gain through a 1 MHz high-pass filter. Measurements were taken in both reflection (measurement is performed on the same transducer which receives the initial pulse) and transmission (signal from the second transducer is measured) modes. Figs. 3.1 and 3.2 show the response of both transducers in reflection mode. No point averaging was done for these measurements.

There is little change in the reflection mode response for the different transducers. The signal from the first transducer shows fewer oscillations in the 15 - 20 μs time interval when compared with the second transducer. This is explained possibly by

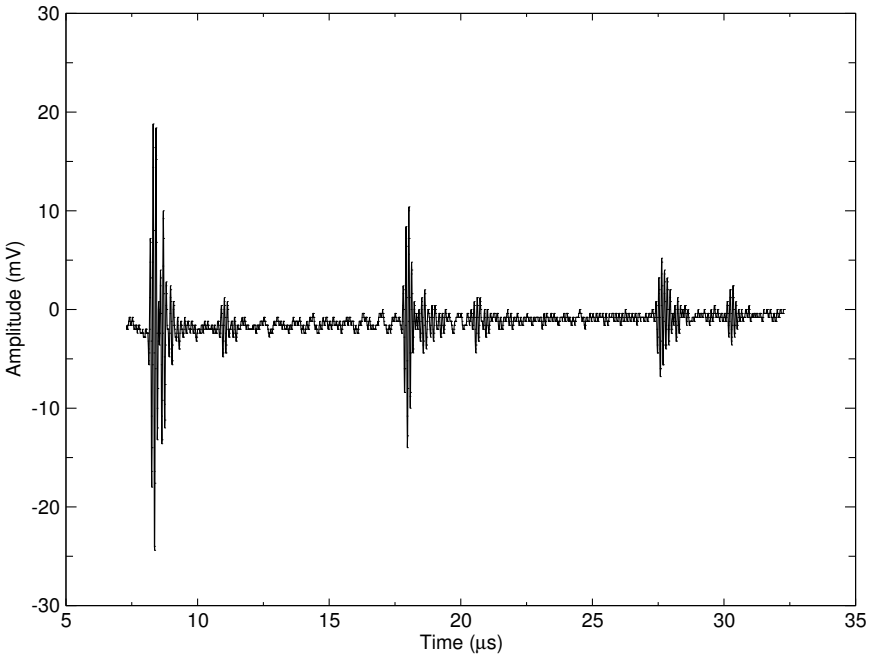

Figure 3.2: Response of transducer attached to delay rod #2 in reflection mode.

poor binding between the three polymer layers used in the transducer construction which would act to reduce the damping of the transducer and thus cause a longer ringing. The first feature is expected to occur at 9.8 μs, corresponding to a transit down and back up the delay rod. While the initial feature in both Figs. 3.1 and 3.2 occurs at $\sim$ 7.5 μs, the time delay between successive major features is the expected 10 μs as these are simply the second and third reflections. A delayed trigger setting on the oscilloscope or beginning measurement at the end of the pulse potential are possible explanations for this discrepancy. There is a secondary pulse approximately 3 μs after the first reflection. The source of this feature is unclear; no dimension of the apparatus would introduce a 3 μs (a delay corresponding to $\sim$ 1.75 cm of quartz). It is

possible that there are additional reflections occurring at the other boundaries of the electroacoustic cell. In particular, the delay rods do not cover completely the surface of the split-ring clamp which hold the delay rods in place. The area of the split-ring clamp unobstructed by the delay rods provides a second surface where compression waves could reflect.

Figure 3.3 shows the fast Fourier transform of the first feature in the reflection measurements for each delay rod. Fourier transforms were performed after some data manipulation (e.g. rescaling the beginning of the time window to zero) using a function built into GNU Octave. The transducers have a nearly identical frequency

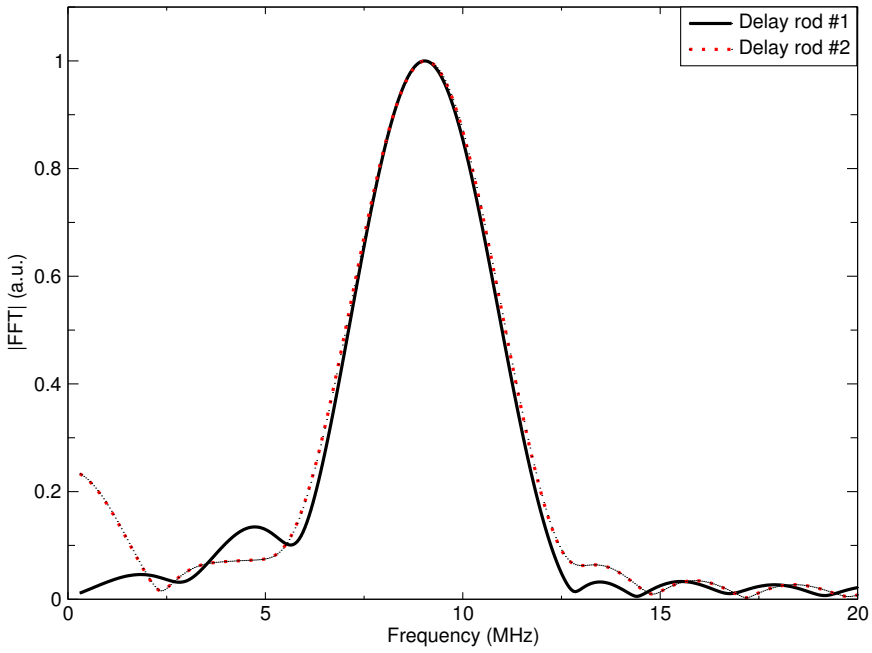

Figure 3.3: Normalized fast Fourier transform of the first reflection for both transducers, with a central frequency of 9 MHz and $\sim$ 5 MHz full width half maximum.

response. Both are centred at 9 MHz and have similar bandwidths. The low frequency components of the Fourier transforms show some differences, particularly the apparent shoulder at ~ 5 MHz for the transducer attached to delay rod #1 and the secondary peak near 0 MHz in the transform of the signal from the second delay rod. These low frequency components reflect how well the transducers are bonded together, mapping possibly to the extraneous ringing observed in Figs. 3.1 and 3.2.

Characterization of the electroacoustic cell filled with water was performed also using transmission mode measurements, shown in Fig. 3.4 for emission from delay rod # 1. The first feature occurs at 12.5 μs, matching closely the expected delay; 4.9 μs for the transmitting delay rod, 3 μs through the the 6.5 mm length of water

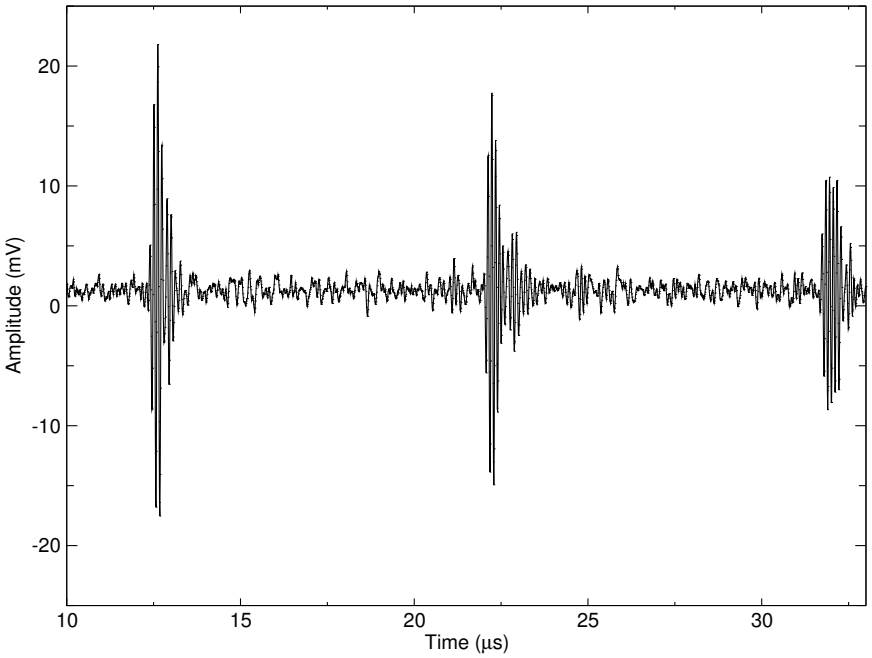

Figure 3.4: Transmission through the first iteration of the electroacoustic cell.

and another 4.9 μs for the receiving delay rod. The secondary feature observed 3 μs after the primary reflection seen in Figs. 3.1 and 3.2 is less prevalent in this mode of measurement.

Figure 3.5 shows the first response of the transducer in the transmission mode measurement with a higher time resolution. The transducer response is as expected for a propagating ultrasound wave (essentially a damped sine function) although there is an anomalous break in periodicity (the dashed line in Fig. 3.5 at $\sim$12.8 μs), which is likely a consequence of imperfect binding of the three layers of piezoelectric polymers used in constructing the transducer.

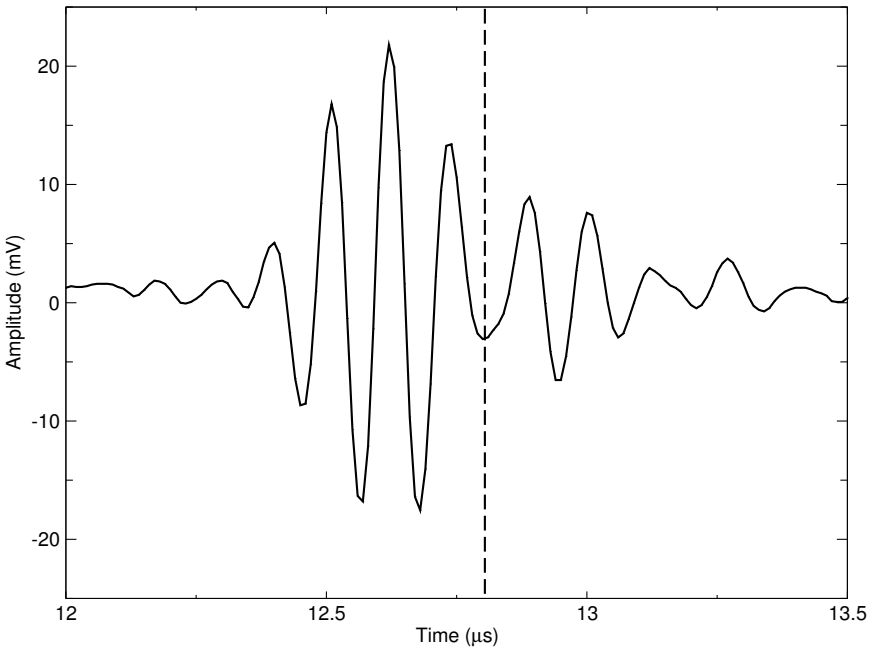

Figure 3.5: Detailed plot of the first feature present in the transmission through the aluminium cell. Dashed line shows the anomalous break in periodicity.

The frequency components of the first feature of the transducer response in transmission mode were determined by a fast Fourier transform, the result of which is shown in Fig. 3.6. As expected, the Fourier transform does not vary significantly from the ones obtained in the reflection measurements. The peak position and bandwidth are effectively the same, with some discrepancies at low frequencies, attributable to the abrupt change in period seen in Fig. 3.5.

Measurements in transmission mode were completed also using the second transducer as the generator of compression waves. The attenuation of the cell was estimated by normalizing the magnitude of each feature observed in the transmission

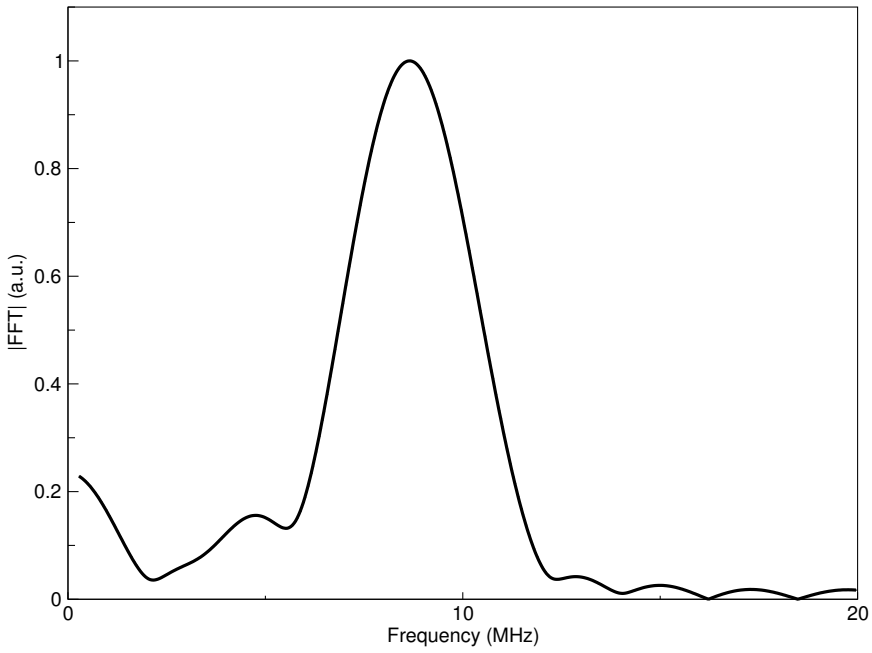

Figure 3.6: Normalized fast Fourier transform of the first transmission through the aluminium cell.

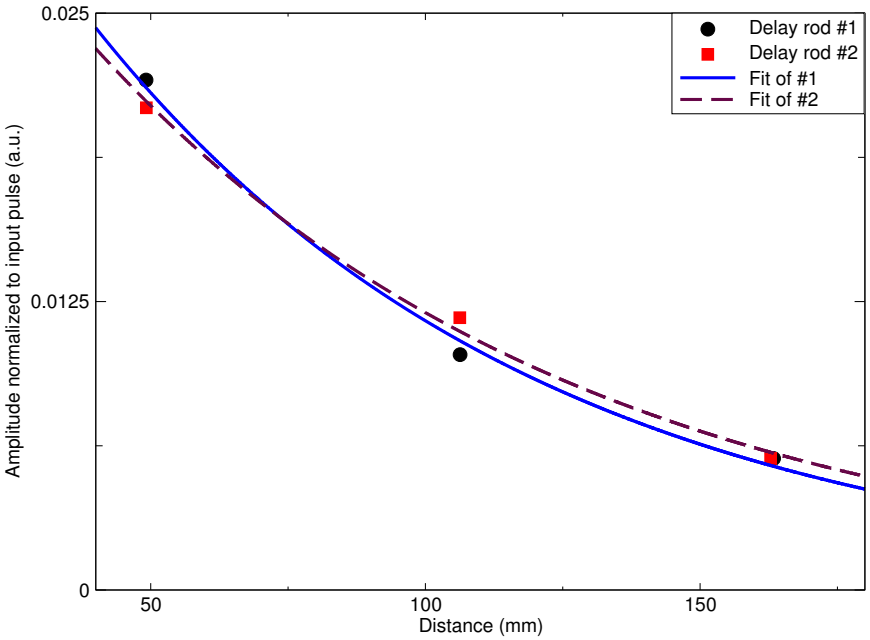

Figure 3.7: Estimate of the attenuation through the aluminium cell. Maximum values for each feature were recorded and normalized to the maximum of the first transmission. Solid and dashed lines are exponential fits to the data.

measurements for both transducers to the input pulse voltage (provided by the pulser, $\sim$ 100 V). The distance of propagation was assumed to be the entire length of the cell for each feature. The result of this analysis is shown in Fig. 3.7. Fitting this data to a single exponential decay ($e^{-\alpha x}$) gave values of α equal to 0.012 mm^{-1} and 0.011 mm^{-1} for the first and second transducer, respectively.

As all the above measurements show, there is very little difference between the two transducer responses, and therefore, either one can be used for the electroacoustic measurements.

3.2 Acrylic cell

The first configuration of the electroacoustic apparatus used an aluminium cell to contain the sample. As this cell did not provide sufficient clearance for attaching contacts to the electrodes that are deposited on the end of the delay rods, a second cell was machined from acrylic. In the initial configuration of the acrylic sample cell, the delay rods were positioned 19 mm apart. Thus, the expected transit time through the cell when filled with water is 12.8 μs (the velocity of a compression wave in water is 1484 m s^{-1} at 25 °C [58]). Figure 3.8 shows the response of the transducer in transmission mode when attached to the acrylic cell. The first feature occurs at 22.5 μs. Accounting for the delay from the two delay rods, the transit time through

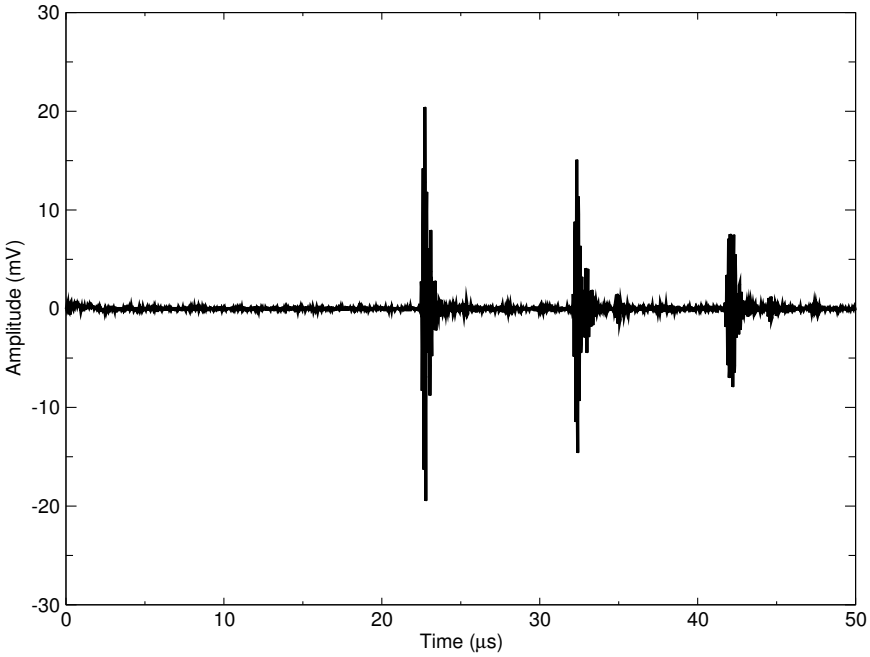

Figure 3.8: Transmission through the first iteration of the acrylic electroacoustic cell.

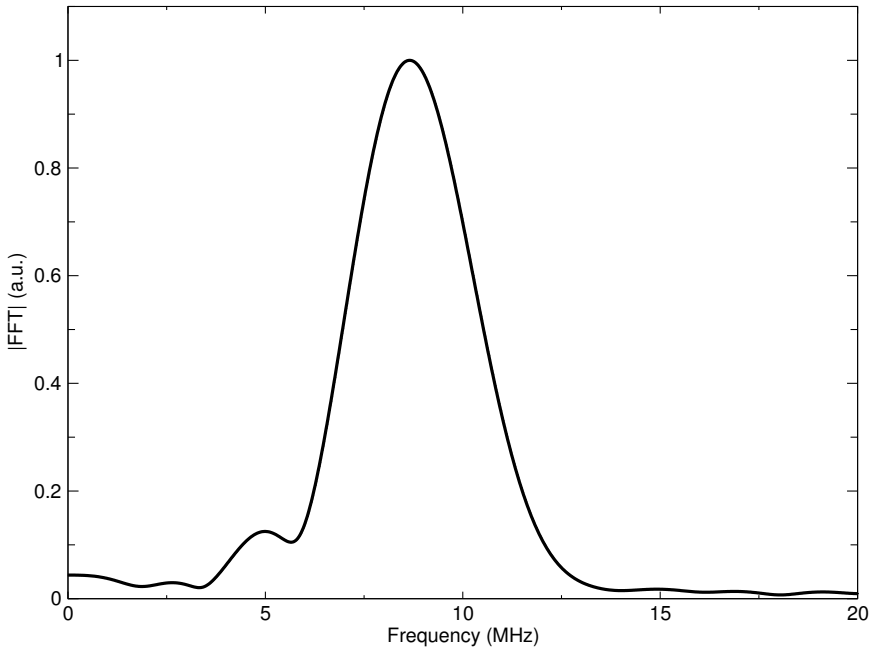

Figure 3.9: Normalized fast Fourier transform of the first transmission through the acrylic cell.

the cell is 12.7 μs, matching closely the expected delay. The separation between the successive signals detected by the transducer is unchanged indicating that, as expected, the acrylic cell had no effect on the characteristics of the transducer/delay rod response.

The transmission mode measurement shown in Fig. 3.8 was performed with contacts affixed to the electrodes. In order to determine if the contacts had any effect on the electroacoustic cell, the frequency components of the first feature in the transmission measurement were determined by a Fourier transform. The results of this analysis are displayed in Fig. 3.9, showing essentially no change from the Fourier transforms from the first configuration of the electroacoustic cell. Thus, attaching

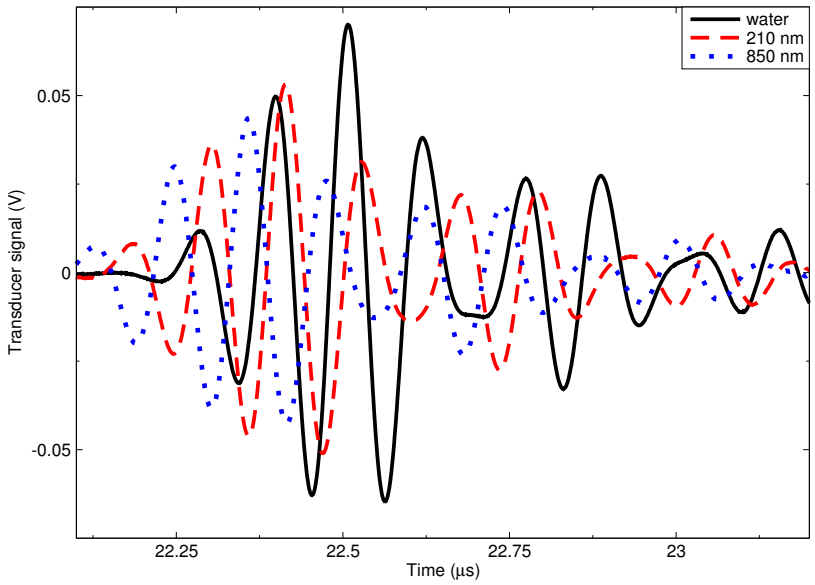

Figure 3.10: Recorded transducer signal in transmission mode with zero applied field.

contacts to the electrodes had no noticeable effect on the propagation of ultrasound through the

electroacoustic cell.

Initial transmission mode measurements of samples (latex spheres) with an applied electric field, driven by a constant sinusoidal potential, showed significant changes in the transit time through the cell. Figure 3.10 shows the recorded transducer response for the first transmission through the electroacoustic cell filled with water, and the 210 nm and 850 nm latex samples with zero applied field. Figure 3.11 displays the result of the same measurements with a constant sinusoidal potential at a frequency of 10 MHz applied to the electrodes. The applied electric field appeared to shift the detection of the ultrasound pulse to later times when the cell was filled with

nanoparticle samples. Repeated measurements using the same conditions revealed that this was not in fact attributable to the sample contained within the cell, but was a consequence of a shifting delay rod. That is, the time delay between the detection of the ultrasound pulse in successive measurements and the initial scan increased as a function of measuring time even when the cell was filled with water. For example, Fig. 3.12 shows the time delay in the detection of the ultrasound pulse as a function of time for a water filled cell.

A clamp to hold the delay rods at a constant separation was constructed to address this issue. The clamp consists essentially of two sets of aluminium slabs, each of which holds one delay rod. By firmly connecting the two sets of aluminium holders, the delay

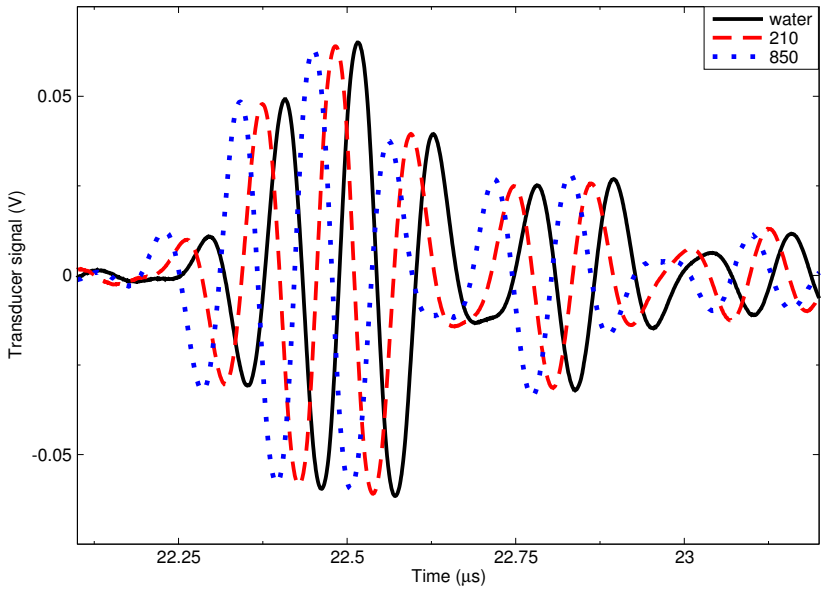

Figure 3.11: Recorded transducer signal in transmission mode with a 500 mV peak-to-peak constant sinusoidal potential at 10 MHz applied to the electrodes.

rod separation can be fixed. Figure. 3.13 shows the same analysis as done in Fig. 3.12, but with the clamps holding the delay rods. Figure. 3.13 displays a clear improvement over Figure. 3.12 (note the change in vertical scale) and thus the effectiveness of the clamps in holding fixed the delay rod separation.

The final step in the cell characterization was to measure the transducer response when only an electric field is applied to the cell. That is, the pulser is no longer used to drive the transducers; the included receiving amplifier is used only to amplify the signal from the transducer. Figure 3.14 shows the amplified signal from the transducer attached to the first delay rod when a five cycle sinusoidal burst potential was applied to the electrodes of the cell filled with water. Shown clearly at small

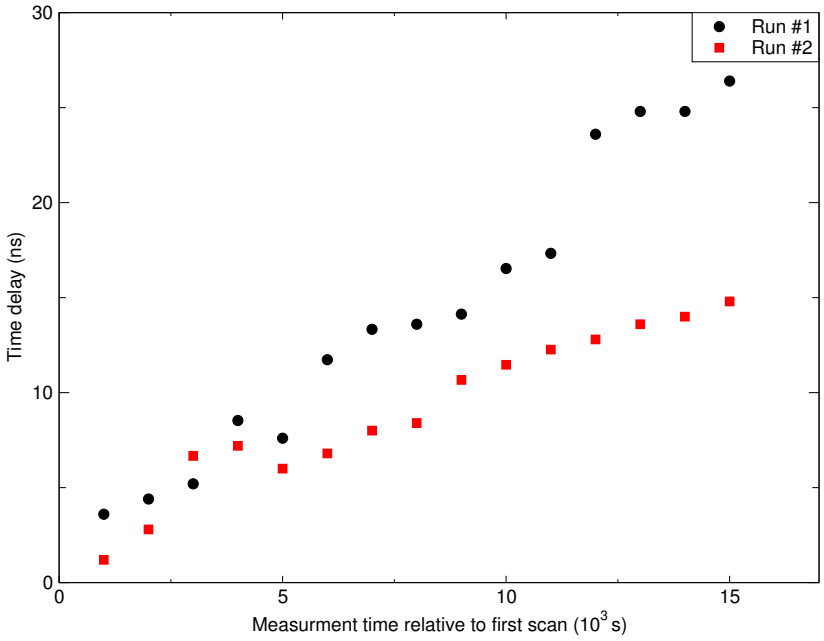

Figure 3.12: Observed delay in the detection of the ultrasound pulse as a function of measuring time for a water filled cell, showing the delay increasing with time.

times is the effect of the electrical cross talk between the applied potential and the transducer. Effectively, the transducer vibrates in response to the changing electric field. The electrical pick-up does not immediately stop after the potential is turned off (the burst potential ends at 0 μs in Fig. 3.14), taking some time to decay completely. While it would be desirable to use the first signal generated by the sample (the one emanating from the closest electrode, see Fig. 2.2), expected to occur at 4.9 μs, it appears that the currently used delay rod does not provide sufficient time for the initial vibrations to decay. Thus, the the second signal from the sample, the one originating from the second electrode, must be used.

Using the second signal from the sample was also problematic for this version

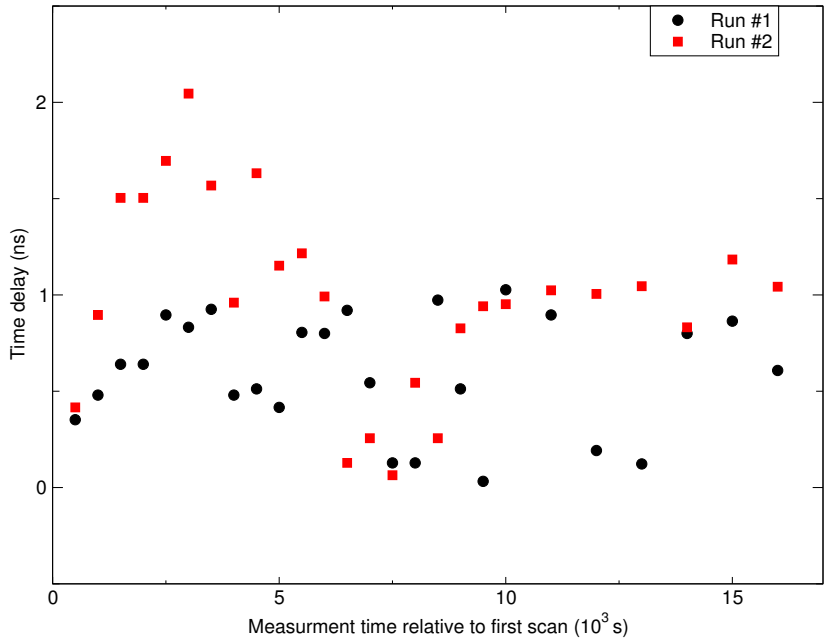

Figure 3.13: Observed delay in the detection of the ultrasound pulse as a function of measuring time for a water filled cell with the added clamp.

of the cell. The response of the transducer to the initial burst potential propagates a compression wave down the delay rod which both transmits through and reflects at the boundary between the rod and the suspension. Thus, a single transducer measures several ultrasound pulses not related to the sample. The first set occurs due to reflections of the pulse generated by the measuring transducer, detected at integer multiples of 9.8 μs. The second set of ultrasound pulses originates from the second transducer, first detected at 22.5 μs, the propagation time through both delay rods and the sample volume, and detected subsequently after intervals of 9.8 μs. The

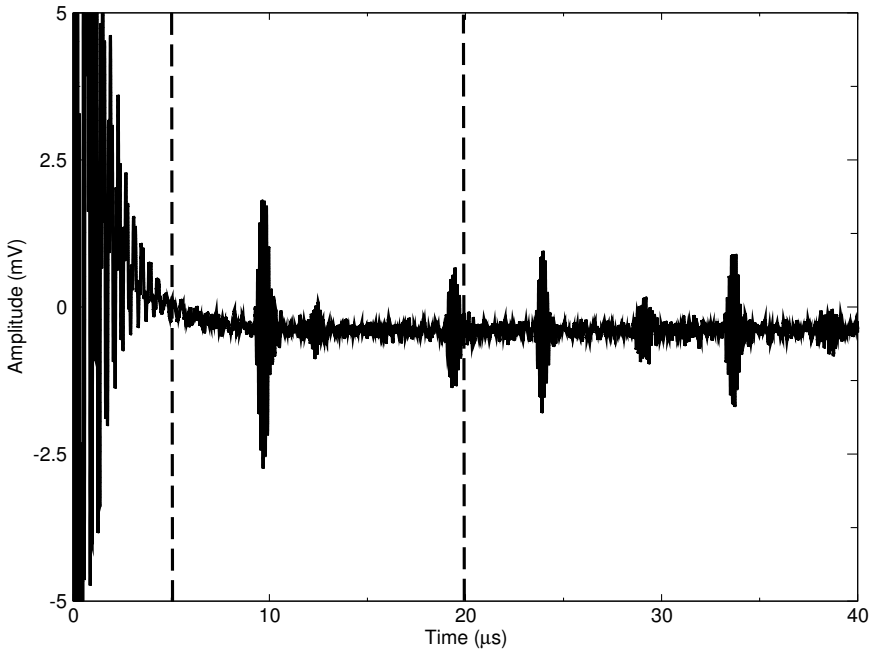

Figure 3.14: Response of the transducer to a 10 MHz, five cycle sinusoidal burst potential applied to the electrodes. The dashed lines indicate the expected detection time of the electroacoustic signals.

ultrasound signal generated by the sample is expected to occur at approximately 18 μs. Thus, for frequencies in which the burst potential lasts longer than 1.5 μs, the signal from the sample could be partially masked by the ultrasound pulse generated from electrical cross talk detected at 19.6 μs.

The final correction to the design of the electroacoustic cell was to adjust the delay rod separation so that the transit time through the sample volume and one delay rod was between 16 and 17 μs. This was accomplished by decreasing the delay rod separation from 19 mm to 17 mm, corresponding to a decrease in the transit time through the sample volume from 12.7 μs to 11.5 μs.

3.3 Electrical impedance

It was expected that the electroacoustic cell would have different electrical properties depending on which particle suspension occupied the cell volume due to the varying conductivities of the suspending media. This could lead ultimately to differences in applied field between samples. The electrical impedance between the electrode of the cell was recorded using a broadband network analyser. Figure 3.15 shows the electrical impedance of the cell recorded from 50 kHz to 50 MHz. The largest difference occurs at smaller frequencies, which is the expected result as the cell acts essentially as a capacitor. That is, the frequency dependence of a capacitor's impedance is f^{-1} and thus, should contribute less to the total impedance with increasing frequency.

Figure 3.16 shows the recorded impedance of the cell filled with water and two

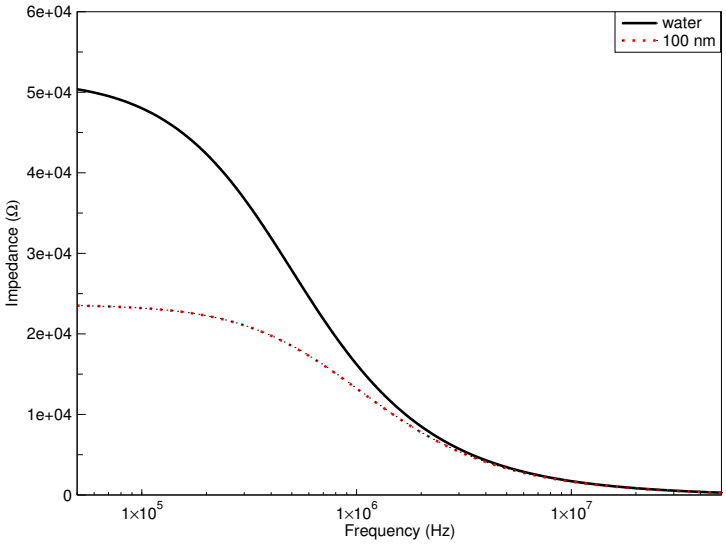

Figure 3.15: Electrical impedance of the acrylic cell containing water and the 100 nm latex spheres.

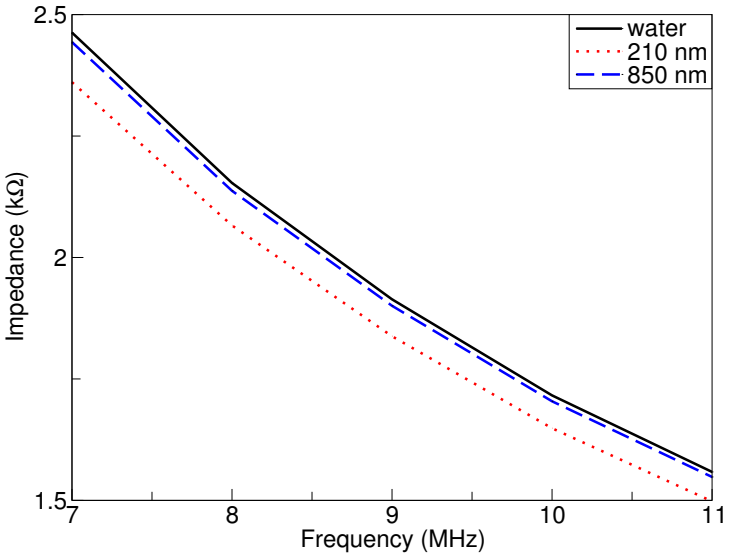

Figure 3.16: Electrical impedance of the acrylic cell containing water, and the 210 and 850 nm latex spheres over the frequency range used for electroacoustic measurements.

latex samples over a smaller range of frequencies corresponding to those used for the electroacoustic measurements. The frequency dependence of the cell impedance does not change significantly when filled with water or the two latex spheres, although a slight change in magnitude was observed ($\sim$ 10 %). If the input side of the electroacoustic apparatus (the components driving the electric field) is set to provide fixed power to the electrodes, there would be an expected $\sim$ 10 % variation in the electric field from sample to sample. To resolve this, the input voltage was monitored and adjusted for each sample to ensure the electric field was of constant magnitude.

Chapter 4

Nanoparticle characterization

In order to determine the effectiveness of the electroacoustic method for determining nanoparticle zeta-potentials and hydrodynamic radii required a characterization of the nanoparticles by other techniques, allowing for a comparison between the various assessments of nanoparticle properties. The following sections describe the results of nanoparticle hydrodynamic size assessment by dynamic light scattering and the impedance technique along with a characterization of the solid nanoparticle cores of several samples by X-ray diffraction measurements. The chapter concludes with a discussion of the results of electroacoustic measurements.

4.1 Particle size determination by dynamic light scattering

Stock nanoparticle suspensions were diluted with additional suspending fluid by a factor of approximately 100, with some variation depending on the concentration of the stock suspension. The scattered light intensity for the diluted samples was collected over at least two minutes, at scattering angles of 60°, 90° and 120°. The measured autocorrelation functions for the nanochip sample at the three scattering angles are shown in Fig. 4.1.

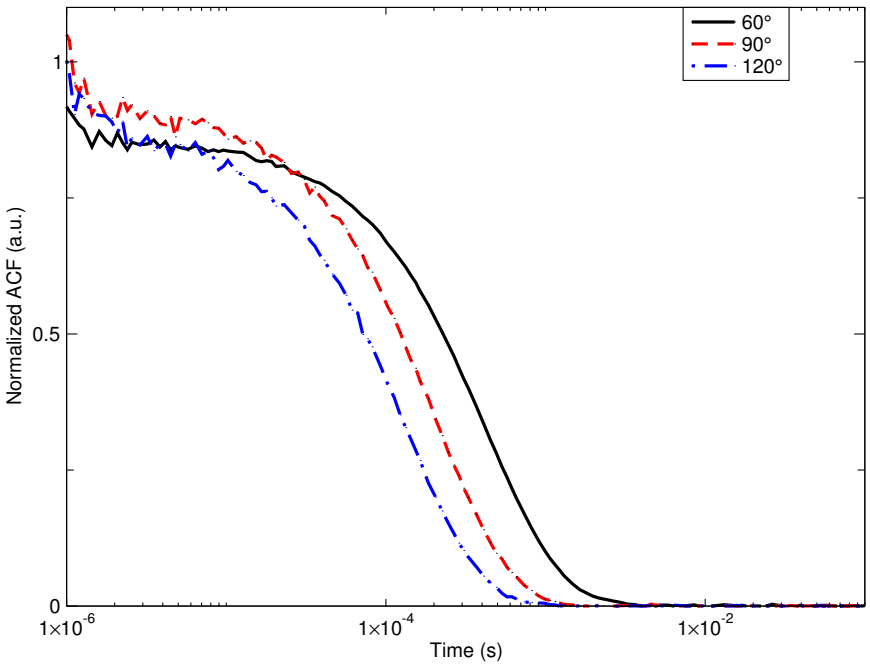

Figure 4.1: Autocorrelation functions collected for the nanochip sample at scattering angles of 60°, 90° and 120°.

Evident from Fig. 4.1 is the effect that scattering angle has on the autocorrelation function. Fitting of the autocorrelation functions to an exponential decay gives the diffusion constant which is then converted to an intensity weighted distribution in hydrodynamic size through Eqn. 2.6. The calculated intensity distributions for the nanochip sample are displayed in Fig. 4.2, showing clearly the very broad distribution of hydrodynamic sizes present in the nanochip sample. The hydrodynamic size distribution provides also some information of the structure of the particles in suspension, primarily if they are spherical or not. The change in the shape of the intensity distribution (Gaussian at 90° and log-normal 60° and 120°) for the nanochip sample with scattering angle is indicative of non-spherical particles [8].

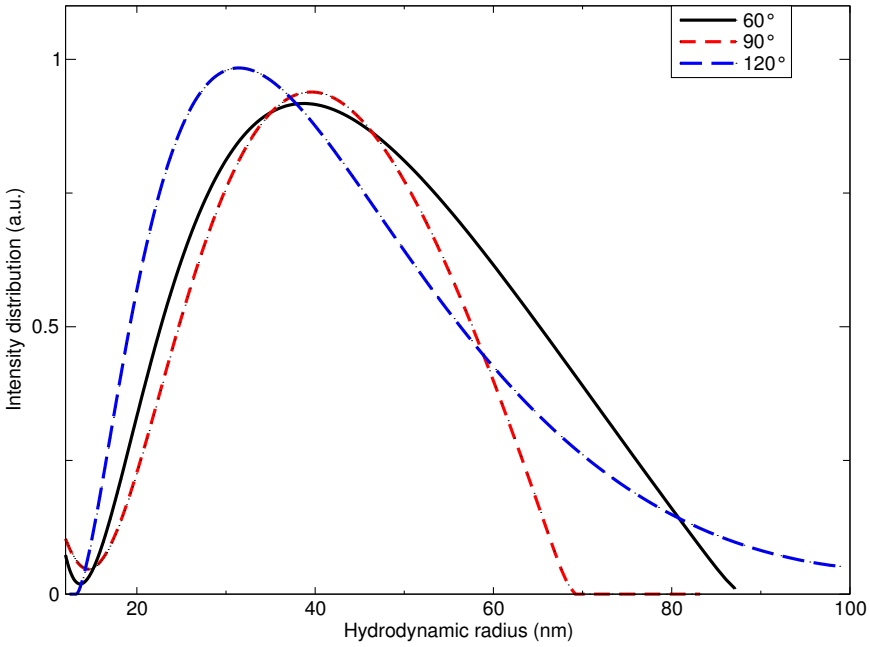

Figure 4.2: Distribution in hydrodynamic radii of the nanochip sample obtained by fitting the autocorrelation functions for different scattering angles.

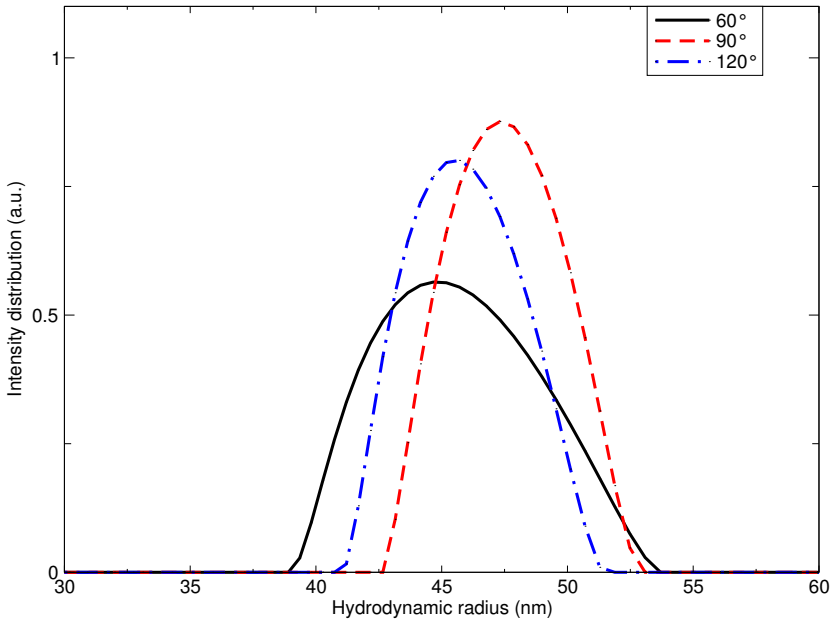

Figure 4.3: Distribution in hydrodynamic radii of the 100 nm latex sample.

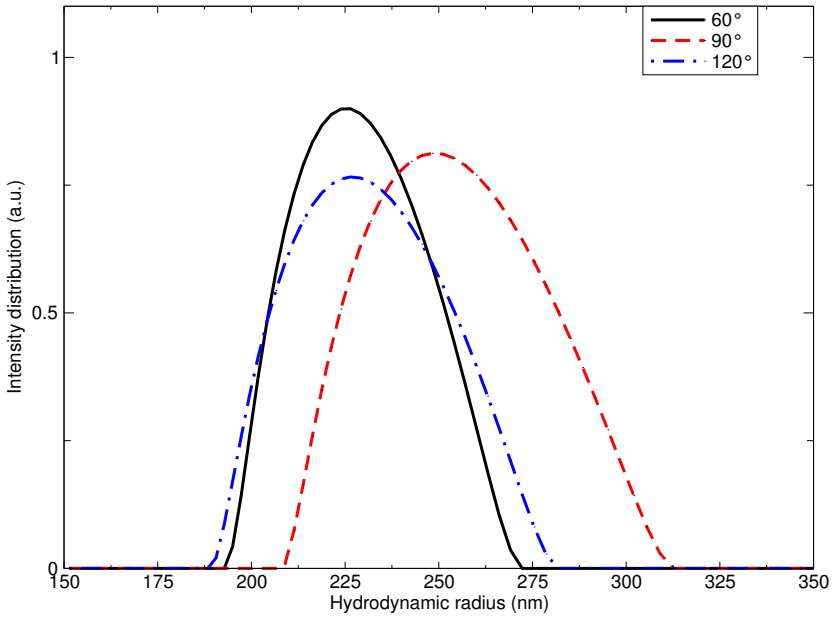

Figure 4.4: Distribution in hydrodynamic radii of the 500 nm latex.

The calculated hydrodynamic size distributions of the 100 nm and 500 nm latex spheres are displayed in Figs. 4.3 and 4.4. The lack of variation in the forms of the distributions determined at each scattering angle is indicative of spherical particles; only the position and width of the hydrodynamic size distributions change as a function of scattering angle. While there is some variation in the means of the hydrodynamic size distributions with scattering angle, the variation is well within the standard deviations.

Figure. 4.5 shows the calculated distributions in hydrodynamic size for the CoFe nanoparticle sample. These show also no change in form with scattering angle, suggesting a population of spherical particles. As is the case with the latex spheres, the

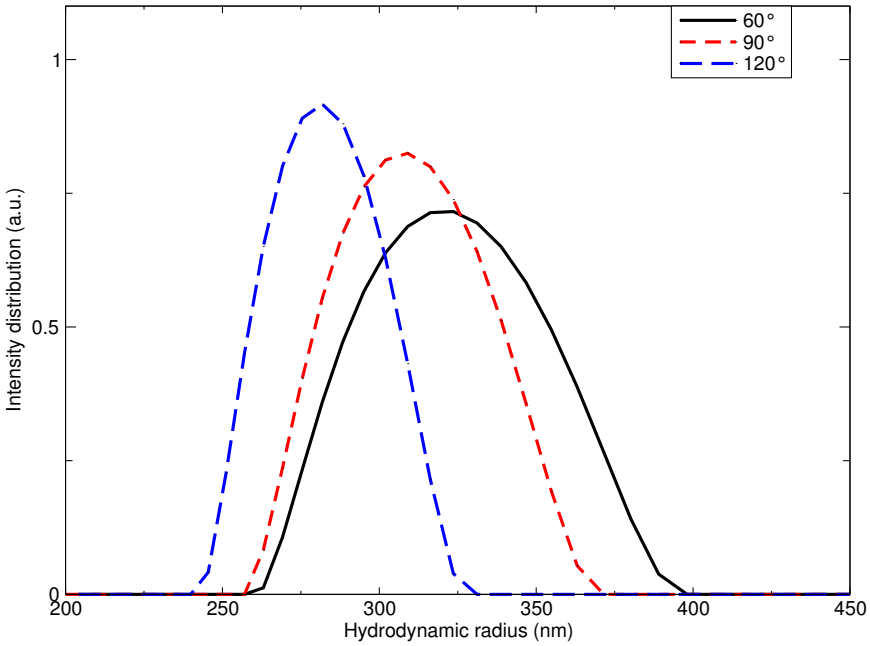

Figure 4.5: Distribution in hydrodynamic radii of the CoFe nanoparticle sample.

variations in the mean hydrodynamic radius of the CoFe nanoparticles as a function of scattering angle are within the standard deviations of the distributions.

The calculated distributions in hydrodynamic radius for the Lignosite sample are shown in Fig. 4.6. This sample showed a vastly different hydrodynamic size at one of the scattering angles (60°), indicative of aggregation effects [8].

The hydrodynamic radii determined at each scattering angle were averaged, the results of which are displayed for all samples in Table 4.1. The total uncertainly in the hydrodynamic size for each sample was calculated by adding in quadrature the deviations of the hydrodynamic size distribution at each scattering angle.

The determined hydrodynamic size for the latex calibration spheres match the

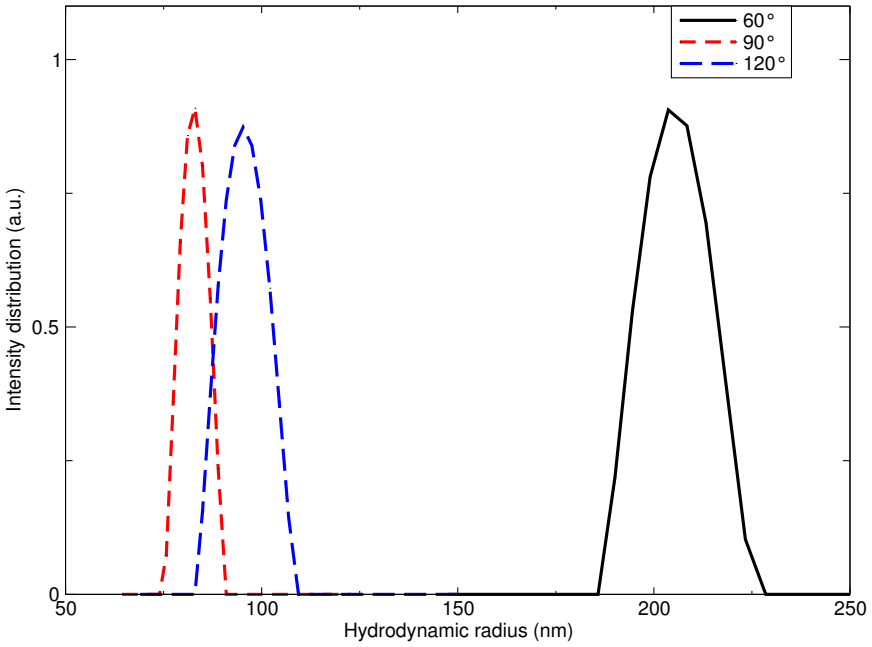

Figure 4.6: Distribution in hydrodynamic radii of the Lignosite sample.

expected size to within 10 %, a discrepancy accounted for by the standard deviation of the size distributions. The hydrodynamic sizes of the magnetite samples synthesized by the group at Kent State agree within error with the initial characterization. The largest discrepancies from the expected size are observed in the Au and CoFe nanoparticle samples. The CoFe in particular is drastically different, likely due to an uneven coating of oleic acid; these particles were not colloidally stable, aggregating and falling out of suspension after approximately one hour.

Table 4.1: Average of the mean hydrodynamic radii determined from fitting the autocorrelation functions at 60°, 90° and 120° for all samples.

Sample	**Hydrodynamic radius (nm)**	**Standard deviation (nm)**
100 nm latex	45	5
210 nm latex	100	20
500 nm latex	240	20
850 nm latex	500	100
NC	40	20
AmS NP	15	5
Au NP	7	1
CoFe NP	300	50
Lig	140	20

4.2 Impedance measurements of rotational diffusion

The frequency dependent susceptibility of two magnetic nanoparticle samples was determined by measuring the impedance of an inductor over the frequency range of 40 Hz to 400 kHz. The real and imaginary component of the AC susceptibility measured for the AmS nanoparticle and Lignosite samples are shown in Figs. 4.7 and 4.8. From Eqn. 2.11, it is clear that the out of phase component of the susceptibility is a maximum when $\omega = 1/\tau$. At low frequencies (large times) the rotational diffusion mechanism of magnetization relaxation is dominant. Thus, the low frequency peaks observed in Figs. 4.7 and 4.8 can be attributed to the energy loss due to the rotational diffusion of the nanoparticle magnetization.

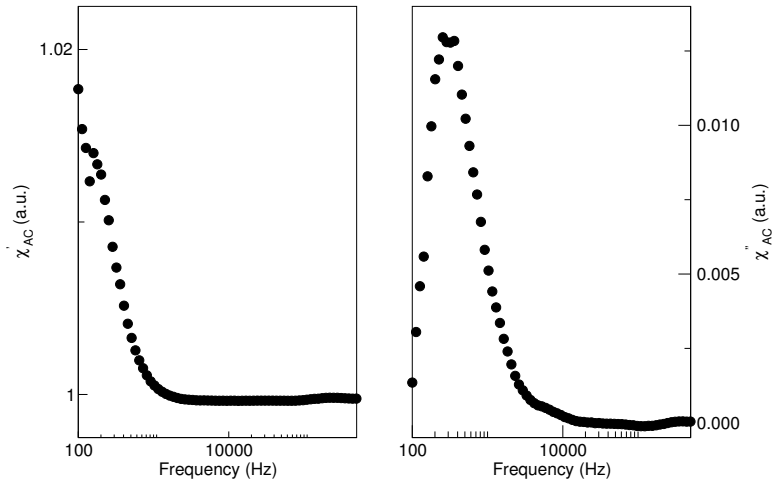

Figure 4.7: AC susceptibility of the AmS nanoparticle sample acquired using the impedance technique.

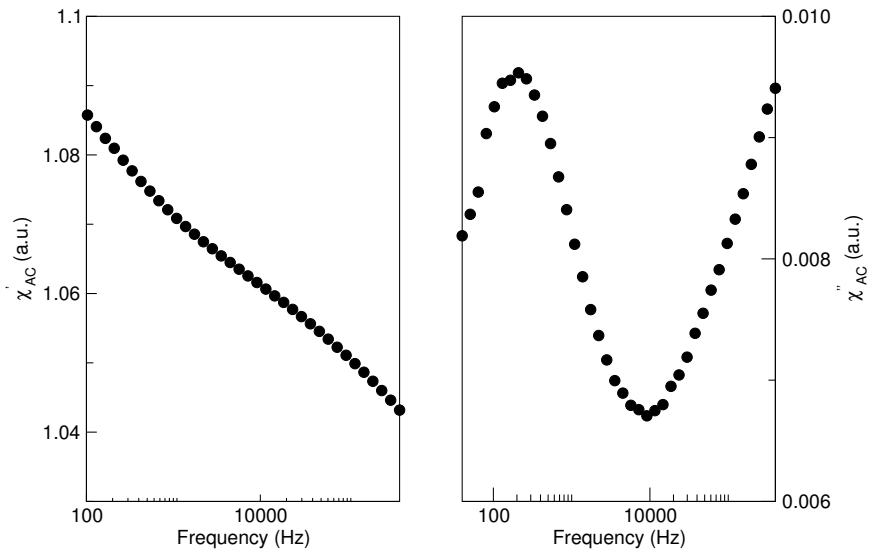

Figure 4.8: AC susceptibility of the Lignosite sample acquired using the impedance technique.

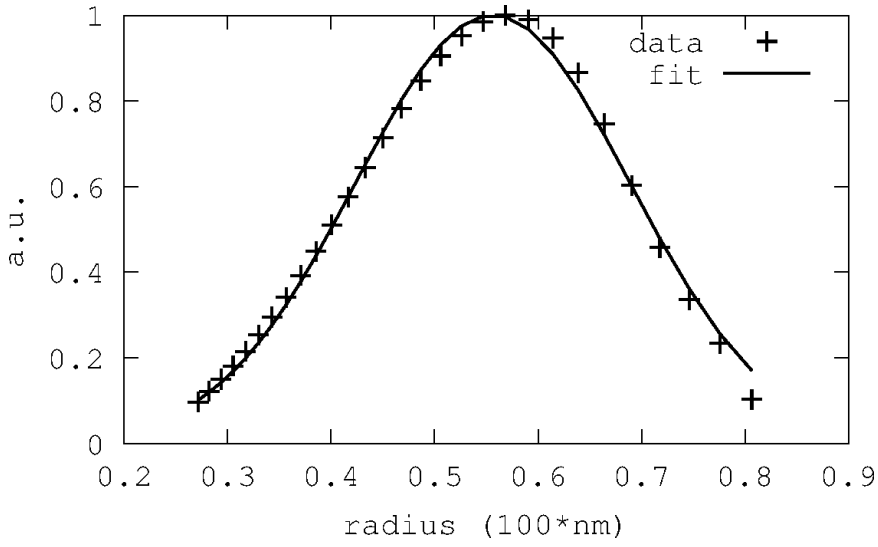

Figure 4.9: Fit to a normal distribution of the imaginary component of the AC susceptibility for the AmS nanoparticle sample.

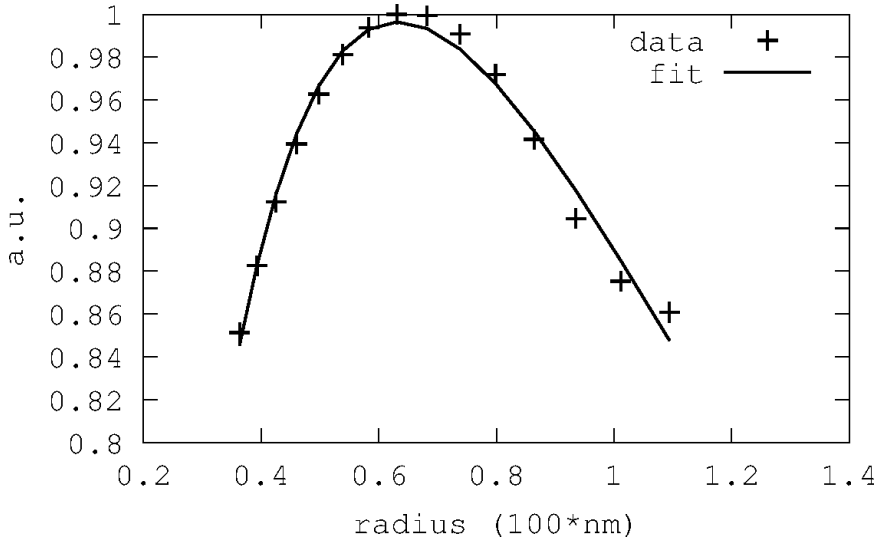

Figure 4.10: Fit to a log-normal distribution of the imaginary component of the AC susceptibility for the Lignosite sample.

As there is a distribution of particle sizes in suspension, there is consequently a distribution in relaxation times. Under this assumption, the frequencies which comprise the peaks in the out of phase component of the AC susceptibility are translated to hydrodynamic radius by means of Eqn. 2.10. The resulting peaks in hydrodynamic radius were then fit to either a normal or log-normal distribution using a least-squares method. The fits to the AC susceptibility data are shown in Figs. 4.9 and 4.10, while the fit hydrodynamic radius and corresponding standard deviations are summarized in Table 4.2.

Table 4.2: Results of fitting the imaginary component of the AC susceptibility obtained by the impedance technique.

Sample	**Distribution**	$a_{hydrodynamic}$ **(nm)**	$\sigma_{hydrodynamic}$ **(nm)**
AmS NP	Normal	60	15
Lignosite	Log-normal	50	10

4.3 X-ray diffraction

A number of nanoparticle samples were analysed also by x-ray powder diffraction. The scattered x-ray intensity was recorded over a range of scattering angle (2θ) for

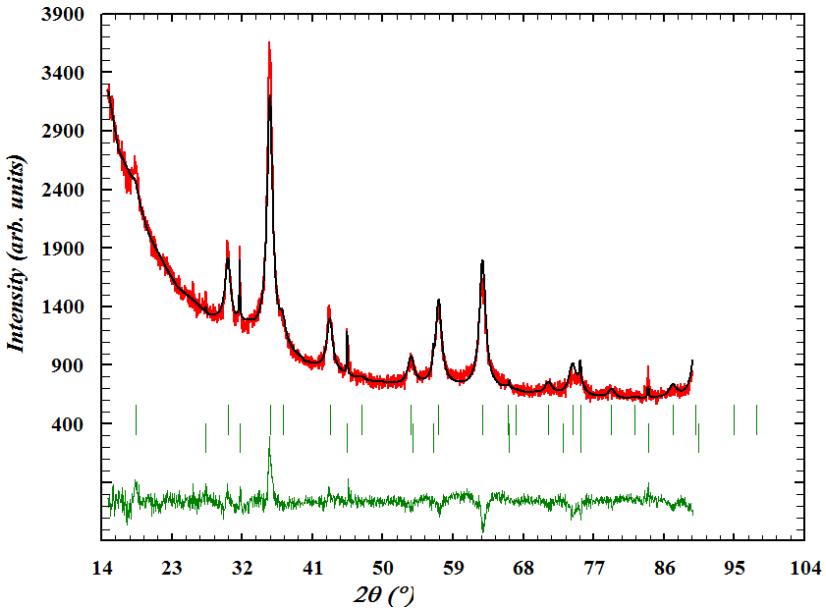

Figure 4.11: Reitveld refinement of the X-ray diffraction pattern obtained for the CoFe nanoparticle sample. The green dashes are Bragg markers of the fitted peaks and below are the residuals.

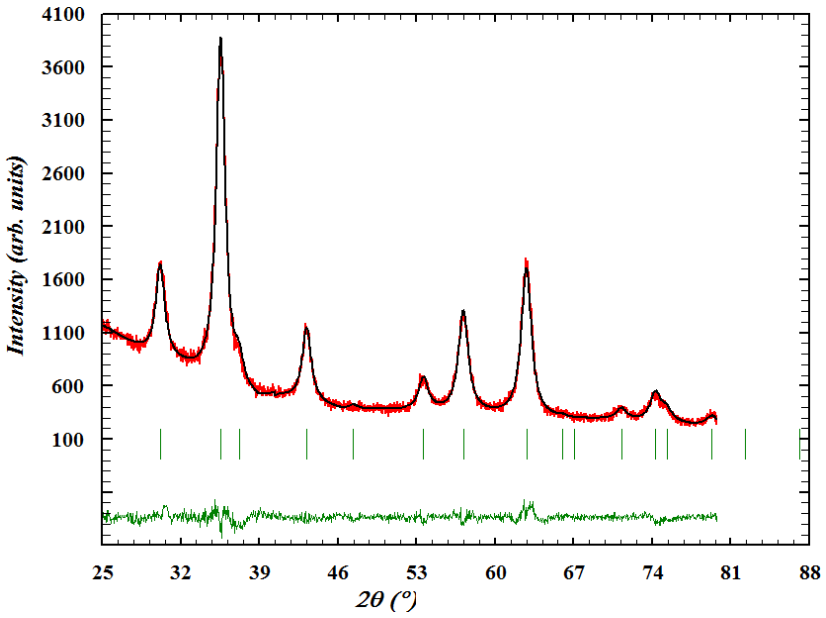

Figure 4.12: Reitveld refinement of the X-ray diffraction pattern obtained for the nanochip sample. The green dashes are Bragg markers of the fitted peaks and below are the residuals.

the nanochip, Lignosite and CoFe nanoparticle samples. The obtained diffraction patterns were analysed using Reitveld refinement [59] as well as by Scherrer analysis of the peak broadening [60].

Reitveld refinement of the x-ray diffraction patterns was accomplished using the FullProf suite [61]. With an assigned space group of $Fd\bar{3}m$ (the symmetry group that best matched the Bragg peaks in the x-ray diffraction pattern), the lattice constant of the CoFe nanoparticles with face centred cubic structure was determined to be 8.3646 ± 0.0006 Å. The crystalline size returned by refinement was 7 nm, a two-fold decrease when compared with the crystalline size determined through analysis of the Scherrer broadening of the peaks. The refinement of the x-ray pattern for the

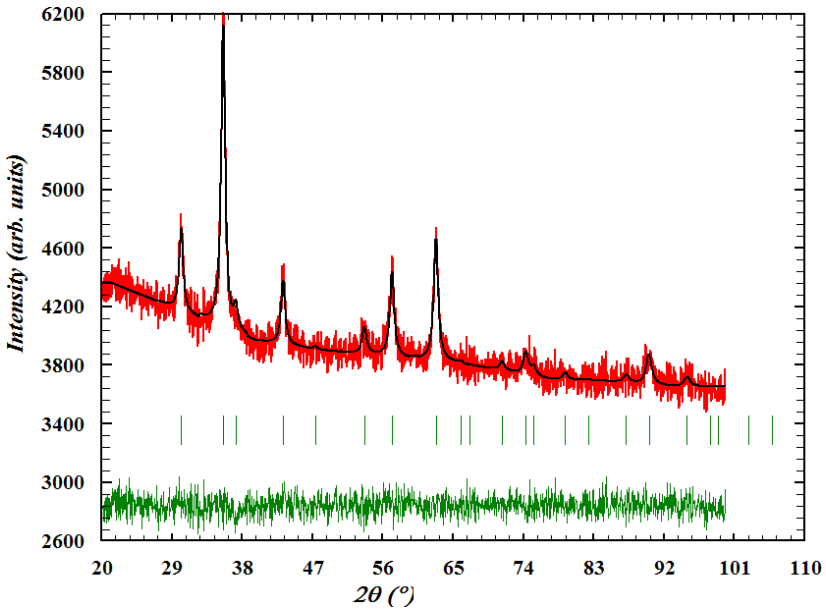

Figure 4.13: Reitveld refinement of the X-ray diffraction pattern obtained for the Lignosite sample. The green dashes are Bragg markers of the fitted peaks and below are the residuals.

CoFe nanoparticles revealed the presence of two phases. The first, corresponding to the broad peaks in Fig. 4.11, was the expected face centred cubic $CoFe_2O_4$ phase. The second phase was determined to have the halite structure (interpenetrating face centred cubic lattices), corresponding to the narrow peaks at 32° and 44.5°. This phase is likely unreacted reagents from the synthesis process.

Similar changes between the crystalline size determined by Reitveld refinement and Scherrer analysis were found for the Lignosite and nanochip samples. The diffraction patterns for both of these samples were refined also using the $Fd\bar{3}m$ space group (the symmetry group that best matched the Bragg peaks). It was determined by refinement that both of these nanoparticle samples are composed of iron-oxide with

Table 4.3: Results of Scherrer broadening analysis and Rietveld refinement of the peaks in the powder X-ray diffraction patterns.

Sample	Scherrer analysis		Reitveld refinement		
	# peaks	Crystalline size (nm)	Space group	Crystalline size (nm)	Lattice constant (Å)
NC	6	10	$Fd\bar{3}m$	6	8.3641 ± 0.0007
Lig	6	16	$Fd\bar{3}m$	5	8.361 ± 0.001
CoFe	5	12	$Fd\bar{3}m$	7	8.3646 ± 0.0006

lattice constants comparable to that determined for the CoFe system. The crystalline sizes of the Lignosite and nanochip samples derived from the refinement were 5 and 6 nm, respectively. A summary of the results of Scherrer analysis and Reitveld refinement for all samples is provided in Table 4.3.

4.4 Electroacoustic measurements

Electroacoustic measurements were performed using two damped sine wave potentials with different number of cycles. Looking first at the measurements with the longer burst potential (Gauss6, Fig. 2.6), taken for electric field frequencies from 4 to 13 MHz in 0.5 MHz steps, with the gain of the gated amplifier was adjusted so that the magnitude of the potential was fixed at 55 V across the frequency range. This

magnitude was chosen as it is the maximum output of the amplifier at the highest frequency. Each measurement is the average of 10,000 scans over the selected time interval, performed internally on the measuring oscilloscope. The transducer response was recorded from 8 to 28 μs at a time resolution of 160 ps/point.

As the measurable electroacoustic signal from the sample is expected to be generated at the electrode opposite the measuring transducer, appropriate time ranges can be chosen for analysis. For water based samples (latex spheres, nanochips and Lignosite) this is between 16 and 18 μs, 17 to 19 μs for the CoFe (suspended in propanol) and 18 to 20 μs for the Au (suspended in hexanes). The difference in expected time arises from the varying speed of compression waves through the different suspending

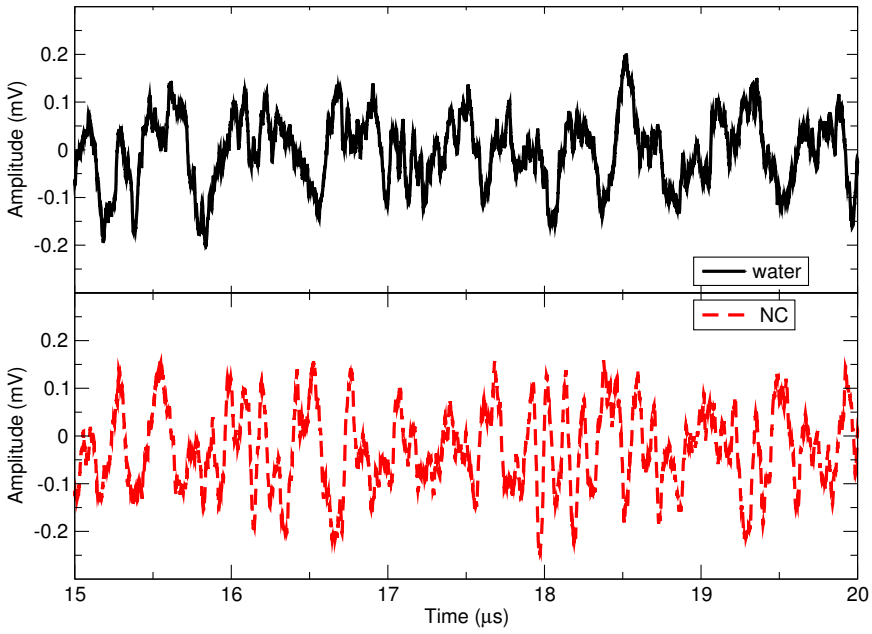

Figure 4.14: Transducer response for the Gauss6 field profile at a driving frequency of 9 MHz for the nanochip sample and water.

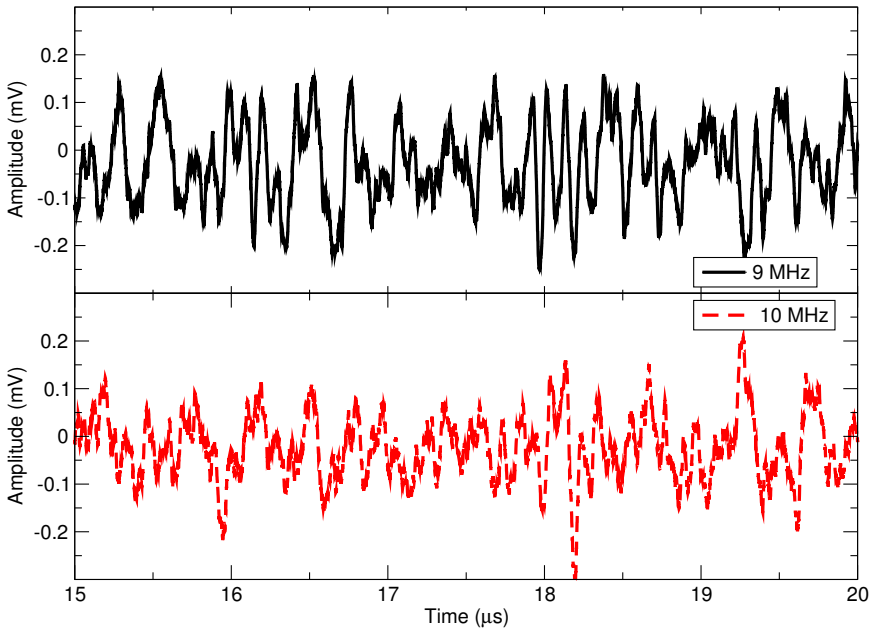

Figure 4.15: Transducer response for the Gauss6 field profile at electric field frequencies of 9 and 10 MHz for the nanochip sample.

media [1].

Figure 4.14 shows the transducer signal over the expected time range for a water and nanochip filled cell. There is not a distinct feature over this time interval that can be attributed to the electroacoustic signal produced by the nanoparticle sample. There are some coherent oscillations in the signal from the nanochip filled cell near 18 μs, but the number of cycles does not correspond to the input potential. That is, at 9 MHz the Gauss6 field profile consists of ten oscillations whereas the transducer signal at 18 μs oscillates only four times. This type of coherent oscillation is not seen at all

[1]The expected delay is calculated by considering a fixed width of suspending media and using the compression wave velocities of the different media.

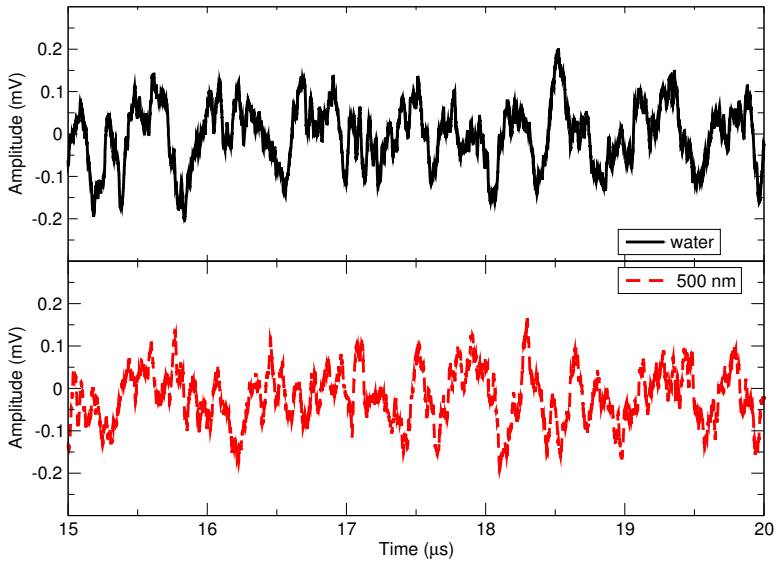

Figure 4.16: Transducer response for the Gauss6 field profile at a driving frequency of 9 MHz for the 500 nm latex and water.

frequencies or for all samples. Figure 4.15 shows the recorded transducer signal for electric fields with a frequency of 9 and 10 MHz for the cell filled with the nanochip sample.

Figures 4.16 and 4.17 show the same scans as mentioned above, but for the 500 nm latex particles. There appears to be very little difference between the 500 nm latex and water filled cell at 9 MHz. The scans of the latex filled cell at different frequencies reveal no visible frequency dependence. As the electroacoustic signal depends linearly on the difference in density between the solid and liquid phase, it is possible that the lack of change observed in the latex filled cell compared to the water filled one is because the produced compression waves are too small to measure.

As the raw transducer signal for nanoparticle samples shows almost negligible

change when compared with scans of a water filled cell, it is clear that a more in-depth analysis is required. The general procedure for this analysis involves isolating the time range over which the electroacoustic is expected to occur, depending on the suspending medium for a particular sample (e.g. 16 to 18 μs for water-based suspensions). A fast Fourier transform is performed over the time interval where an electroacoustic signal is expected. As the frequency of the electroacoustic signal is expected to be to same as that of the electric field, the maximum in the Fourier transform around the frequency of the applied field is taken. The interval over which the maximum is searched for is taken as the frequency step used in the measurement. That is, for 0.5 MHz steps of the electric field frequency, the maximum in the Fourier transform is taken in a 0.5 MHz interval centred on the frequency of the electric field.

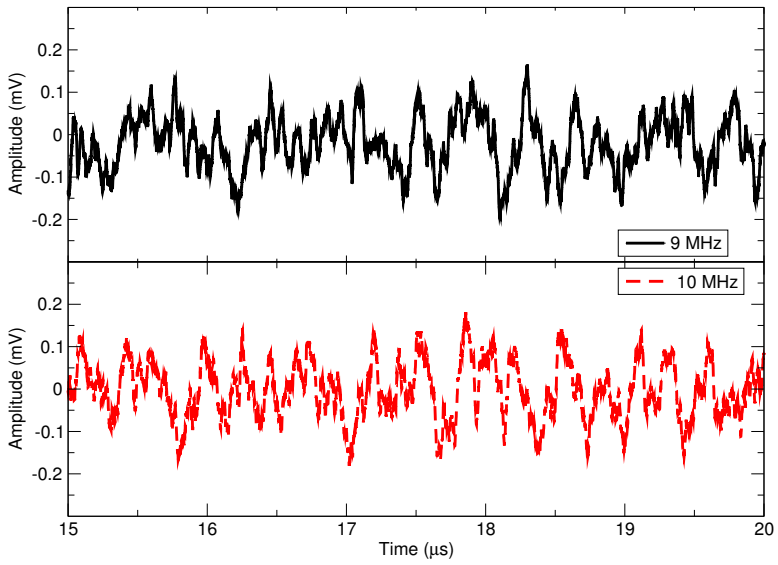

Figure 4.17: Transducer response for the Gauss6 field profile at electric field frequencies of 9 and 10 MHz for the 500 nm latex spheres.

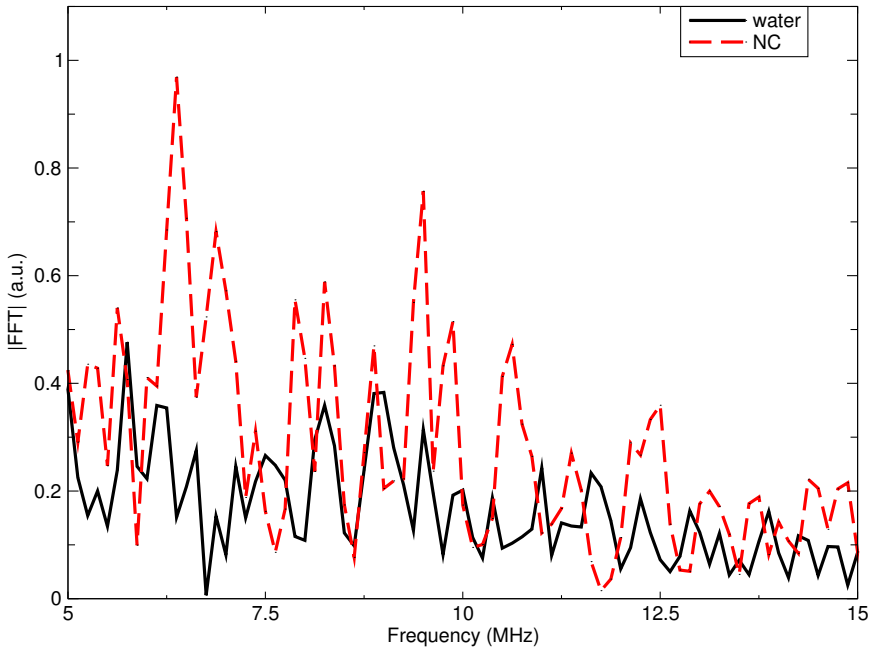

Figure 4.18: Magnitude of the Fourier transform of the recorded transducer signal for the nanochip sample and water at a driving frequency of 10 MHz.

In order to accurately compare the magnitude spectra between different frequencies of applied fields, the Fourier transforms are normalized to a common signal. The value used for normalization was taken as the maximum of the Fourier transform of a pure sine wave with unit magnitude and a frequency equal to that of the driving electric field, computed over the same 2 μs time interval.

Figure 4.18 shows a comparison of the Fourier transform of the transducer response when the cell is filled with the nanochip sample to that of a water filled cell at a frequency of 10 MHz. While the maximum in the spectrum of the nanochip sample is at a lower frequency than the applied field, there is a component close to 10 MHz that is larger than in the spectrum computed for the water filled cell. It is the value

of the Fourier transform at this point which is tracked for each frequency.

Further evidence of the electroacoustic response of the nanochip sample can be seen through a comparison of the fast Fourier transforms performed over a shorter time interval (where there exists coherent oscillations). Figure 4.19 shows the ratio of the fast Fourier transform of the transducer response with a nanochip filled cell to a water filled one. This Fourier transform was calculated over a shorter, 1 μs time interval beginning where the electroacoustic signal is expected to occur (16.5 μs). The magnitude of the fast Fourier transform of the response with the nanochip filled cell

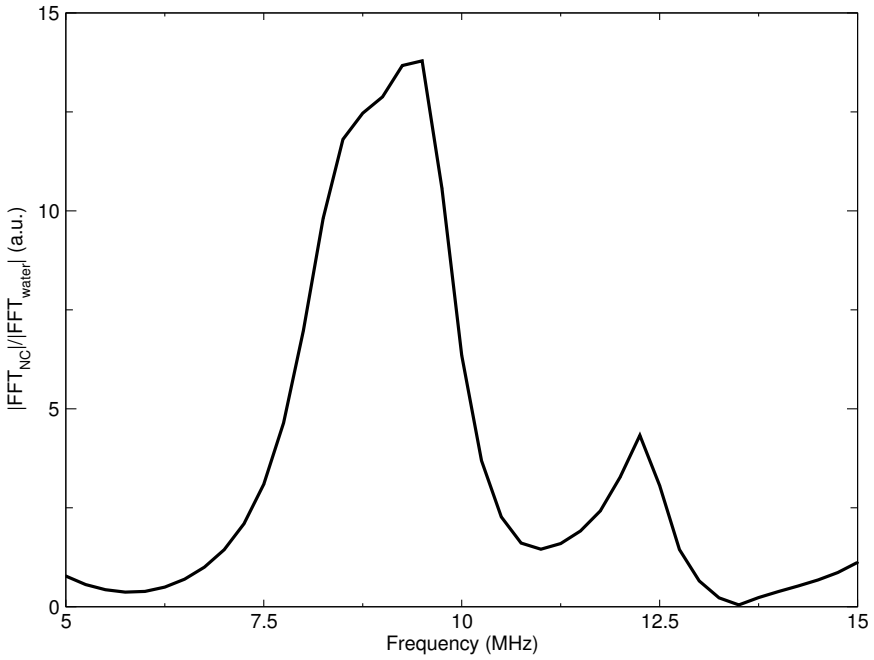

Figure 4.19: The ratio of the magnitude of the fast Fourier transform of the transducer response with a nanochip filled cell to a water filled one for an applied electric field with a driving frequency of 8 MHz.

is larger than the water filled cell over a range of frequencies centred roughly on the driving electric field frequency ($\sim$ 7 to 10 MHz). It is known through characterization of the electroacoustic apparatus (Fig. 3.3) that the transducers used are more sensitive over a range of frequencies which maps well to the width of the feature shown in Figure 4.19. The increased transducer response with the nanochip filled cell is indicative of a real electroacoustic signal produced by the colloidal nanoparticle sample and therefore shows the effectiveness of the electroacoustic apparatus. With this in mind, a comparison between the electroacoustic response of the different nanoparticle samples can be made.

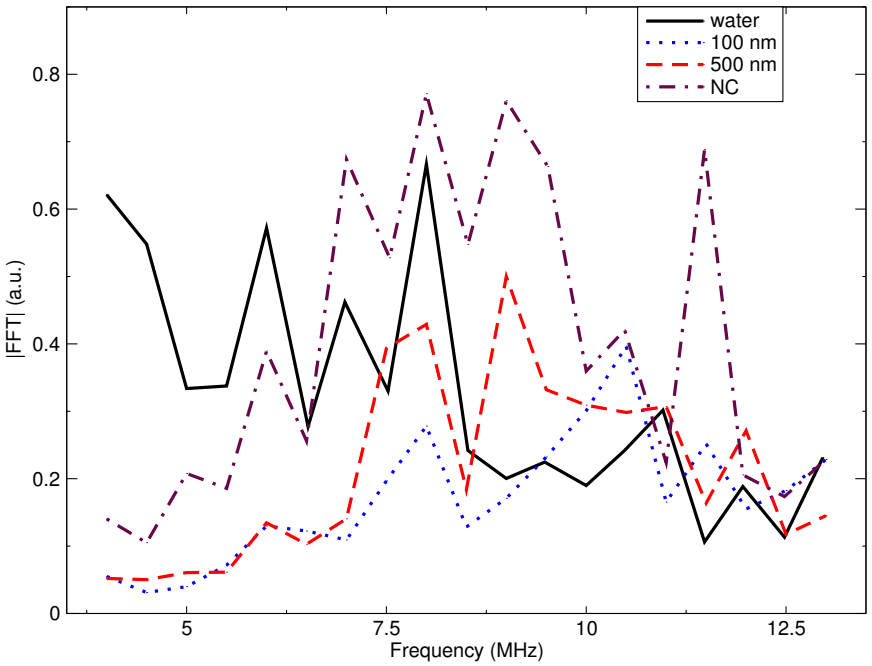

Figure 4.20: Magnitude of the fast Fourier transform of the transducer response centred around the frequency of the applied electric field with the Gauss6 profile.

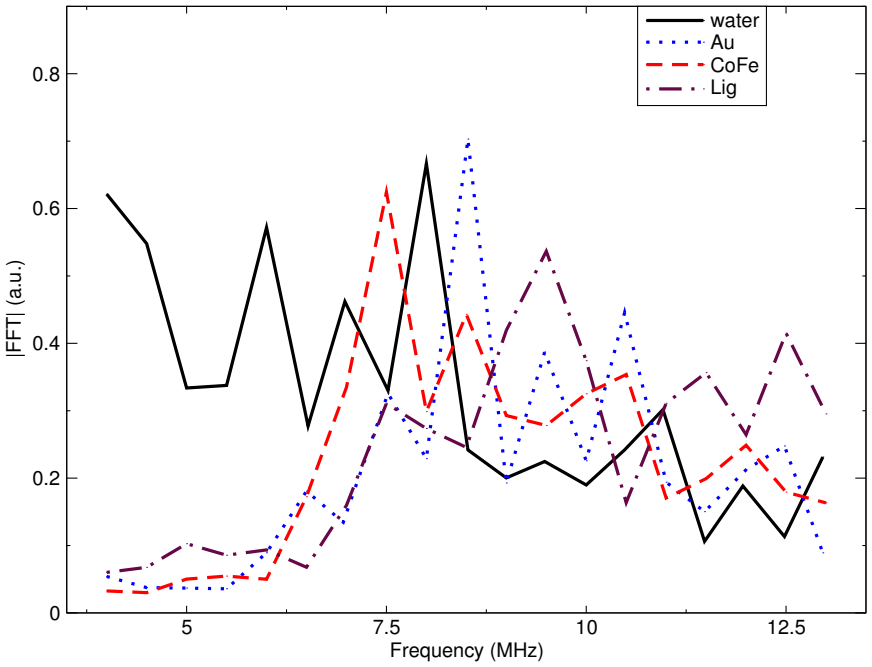

Figure 4.21: Magnitude of the fast Fourier transform of the transducer response centred around the frequency of the applied electric field with the Gauss6 profile.

Figure 4.20 shows the magnitude of the maximum in the Fourier transform centred on the frequency of the applied electric field as a function of that frequency, for two latex and nanochip samples. This quantity calculated for the scans of the cell filled with deionized water is included also, as this should represent the properties of the electroacoustic cell by itself. There should be effectively no ionic species present in the deionized water and thus it can be used as an effective background. While at low frequencies the magnitude of the Fourier transforms for the nanochip sample is below that of water, there is a steady increase with frequency, surpassing the values for the water filled cell at 7 MHz. The maxima in the magnitude of the transducer response

for the latex calibration spheres stay well below the values for the water filled cell for most frequencies. Only for a $\sim$ 3 MHz range does the maximum magnitude of the transducer response for the latex filled cell surpass that of water.

A clearer trend in the computed magnitude of the transducer signal is apparent for the Au nanoparticle, CoFe nanoparticle and Lignosite samples, as seen in Fig. 4.21. These samples follow roughly the same trend; increasing rather quickly in magnitude up to a frequency of 7-8 MHz followed by a slow decrease. The magnitude of the transducer signal for these samples is very close to that for the water filled cell over all frequencies.

For the second field profile (Gauss2, Fig. 2.5), the maximum output from the

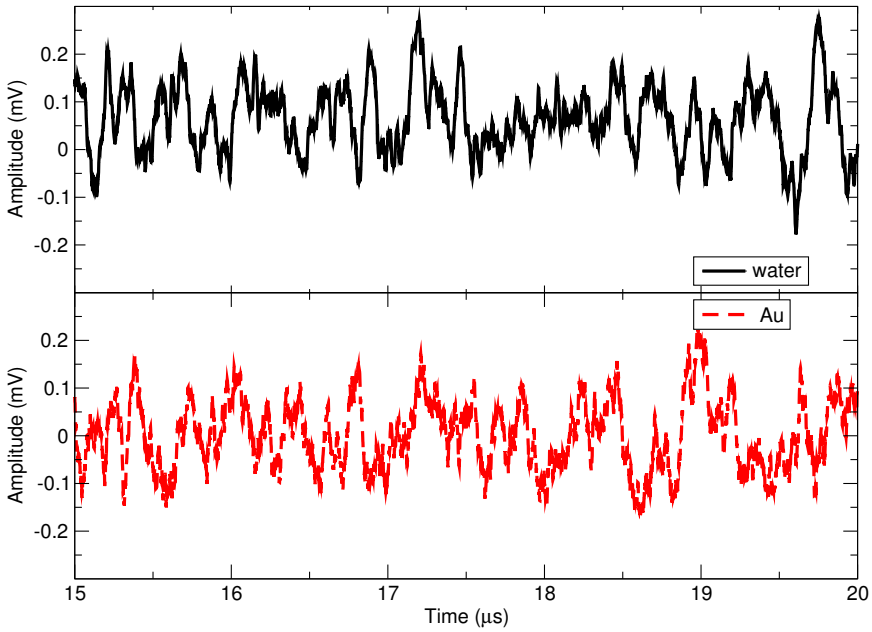

Figure 4.22: Transducer response for the Gauss2 field profile at a driving frequency of 8 MHz for the Au nanoparticle sample and water.

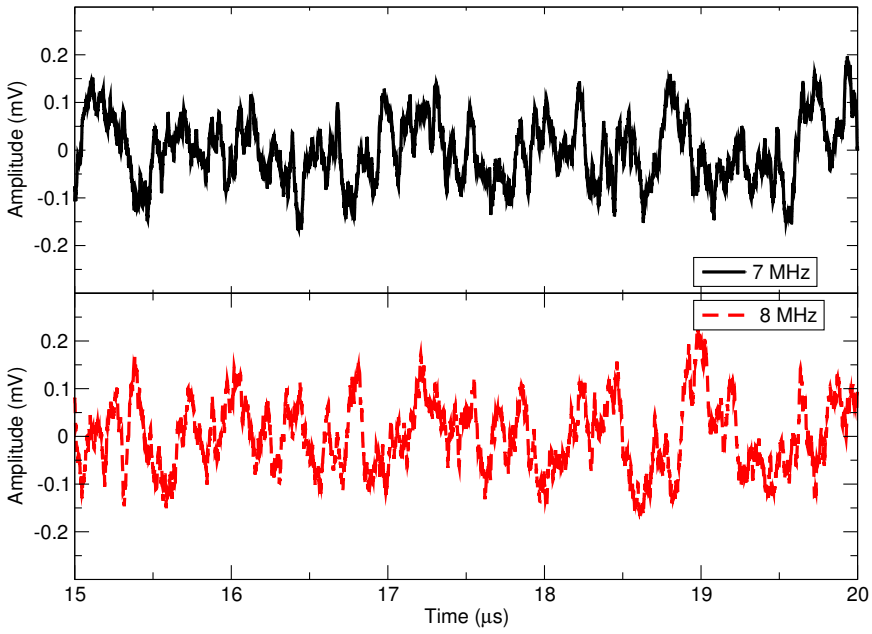

Figure 4.23: Transducer response for the Gauss2 field profile at electric field frequencies of 7 and 8 MHz for the Au nanoparticle sample.

gated amplifier at 13 MHz was 50 V, and this was the potential used over the whole frequency range. The same electric field frequencies were used as in the measurements with the Gauss6 field profile. The measurement conditions for the oscilloscope were also unchanged.

The transducer signals recorded with the electroacoustic cell filled with water and Au nanoparticle at 8 MHz are shown in Fig. 4.22. As is the case with the longer (in time) burst potential discussed above, there are no obvious coherent oscillations in the data collected for the Au nanoparticle filled cell. Ultrasound generated by particles suspended in hexanes is expected to be detected between 18 and 20 μs (due to the decreased velocity of compression waves through hexanes when compared with

water) for the current configuration of the measuring device. The signal recorded for the Au nanoparticle over this time interval is not noticeably different from the lower times shown in Fig. 4.22.

As an example of the changes in the measured transducer response with frequency, Fig. 4.23 shows the collected signal for Au nanoparticles at frequencies of 7 and 8 MHz. While there is a difference in the structure of the time domain signal between the two frequencies, similar changes are observable at times where no ultrasound is expected from the sample.

Again, it is required to analyse the magnitude spectra of the recorded transducer

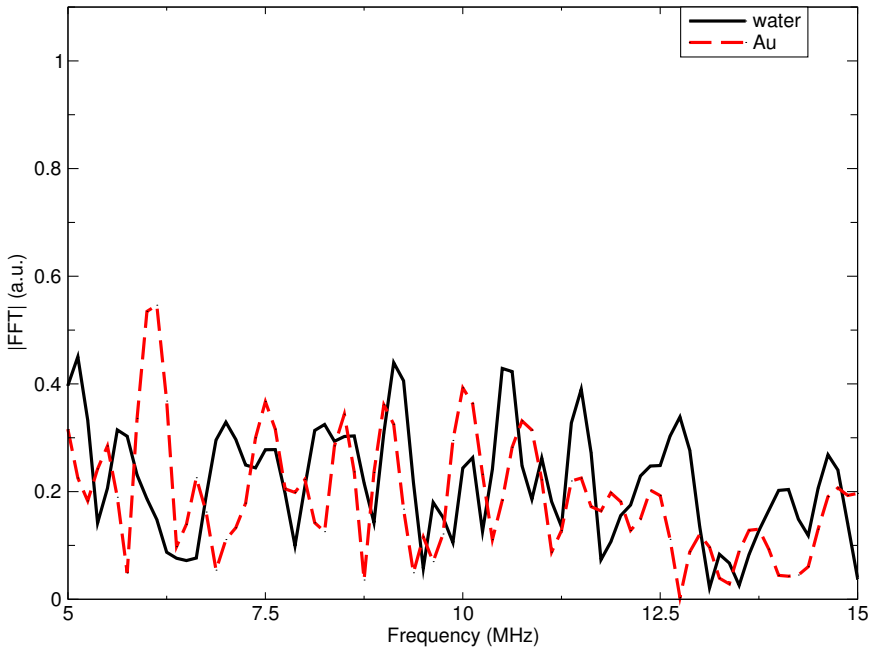

Figure 4.24: Magnitude of the Fourier transform of the recorded transducer signal for the Au nanoparticle sample and water at a driving frequency of 8.5 MHz.

signal to look for any changes in the electroacoustic response between samples. The same approach that was used for finding the maximum magnitude at the expected frequency of the electroacoustic signal with the Gauss6 field profile is applied here. First, by comparing the Fourier transform of one sample at a single frequency to the magnitude spectrum of the water filled cell at the same frequency, it can be seen that while small, there is a difference between the two. This is shown in Fig. 4.24, displaying the Fourier transform of the transducer response with a driving frequency of 8.5 MHz.

As before, tabulating the maximum value of the magnitude spectra near the expected frequency of ultrasound generated by the electroacoustic effect for each sample

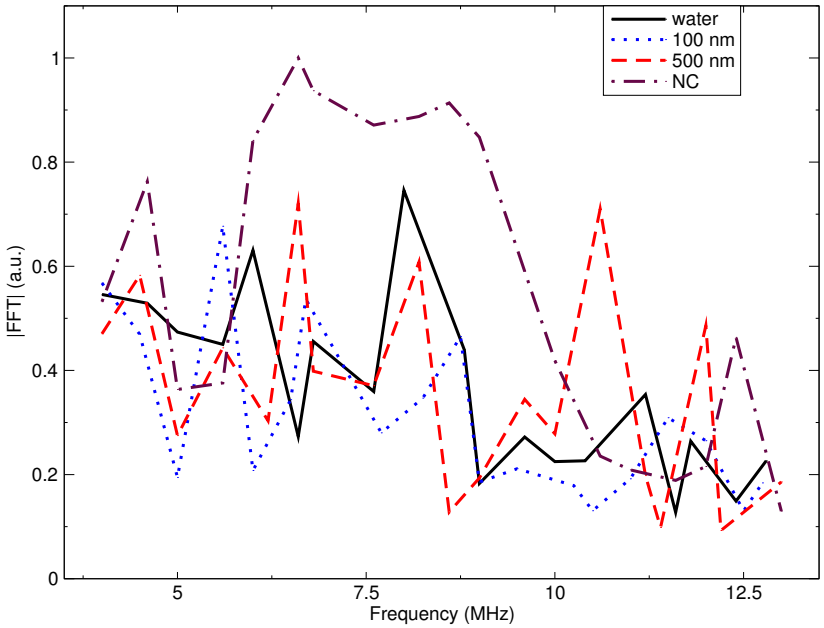

Figure 4.25: Maximum in the magnitude of the Fourier transform of the transducer signal as a function of driving field frequency for the Gauss2 profile.

will allow for observations of any trends with frequency. The result of this tabulation for the 100 and 500 nm latex along with the nanochip samples is shown in Fig. 4.26. Out of these three nanoparticle systems, only the nanochips show any obvious change with the electric field frequency. The maximum in the magnitude spectrum centred around the frequency of the electric field rises quickly above the water background and remains above this level over a range of $\sim$ 3 MHz. While the latex spheres show some change at higher frequencies, the calculated magnitude of the transducer signal at low frequencies is comparable to the water background.

Figure 4.26 shows the results of the same data analysis as done for Fig. 4.25, but for the Au nanoparticle, CoFe nanoparticle and Lignosite samples. These samples show

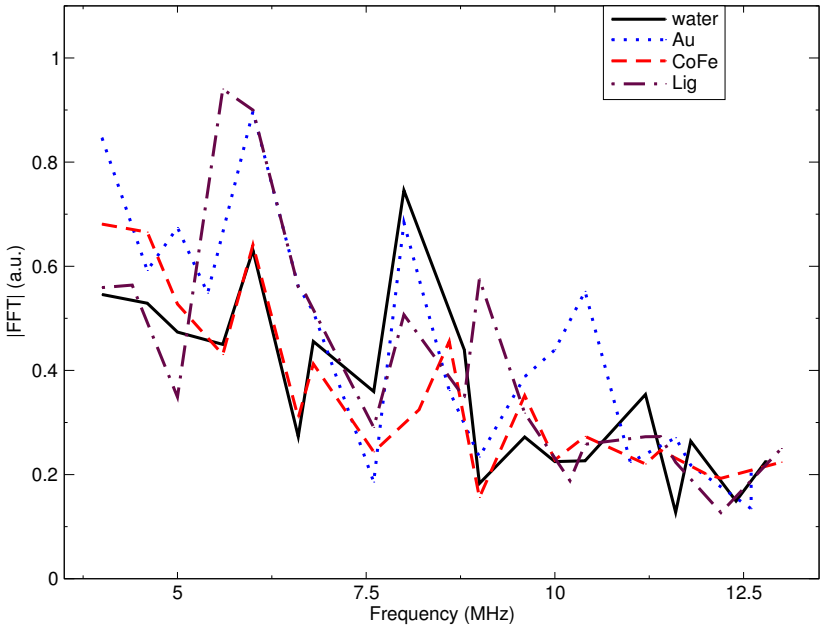

Figure 4.26: Maximum in the magnitude of the Fourier transform of the transducer signal as a function of driving field frequency for the Gauss2 profile.

less change with respect to the water background than the nanochip formulation, although the Au nanoparticle and Lignosite exhibit a low frequency maximum. The CoFe nanoparticle sample shows essentially no useful features as the magnitude of the Fourier transform spectrum in this case does not change significantly from the water background. While this is a surprising result, this is likely due to aggregation effects occurring in the CoFe nanoparticle system, as will be described further in the following discussion section.

Chapter 5

Discussion of the results

As a consequence of the small signal amplitudes measured by the electroacoustic apparatus, it is clear that a direct determination of particle size and zeta-potential by mapping the results to theory is problematic as nanoparticles fall likely into the "intermediate" regime of double layer thickness described in Sec. 1.1. Instead, combining the results of the other particle characterization techniques will allow for tracking the changes in the electroacoustic signal as a function of the nanoparticle properties. By comparison between the electroacoustic signals generated by samples with known zeta-potential, a qualitative discussion of the zeta-potential dependent electroacoustic effect can be undertaken.

The electroacoustic signal generated by a particle suspension depends fundamentally on the properties of the suspending medium and the particle hydrodynamic size and zeta-potential, while detection of the generated signal will depend on the elec-

troacoustic instrument itself. As the electroacoustic measurements were all performed using the same configuration of the instrument with only differing field profiles, the results obtained can be compared without consideration of the instrument factors (e.g. geometry of the electroacoustic cell and characteristics of the transducer response). The effect that the electric field profile has on the electroacoustic instrument can be determined through a comparison of the transducer response for the water filled cell collected with both field profiles, shown in Figs. 4.20 and 4.25. While there are some variations between the measured transducer response of the water filled cell for the Gauss2 and Gauss6 pulse profiles, the frequency dependence is similar. That is, there is a similar decrease in magnitude of 50 % over the frequencies of the driving electric field, and both field profiles show a maximum in the magnitude of the transducer signal at around 8 MHz. Thus, it is appropriate to compare the electroacoustic measurements collected using either field profile.

While the presence of particles will alter somewhat the behaviour of the suspending medium (e.g. density and viscosity changes with variation in particle concentration), the influence that these properties have on the generated electroacoustic signal can be reduced by comparing only nanoparticles suspended in the same medium with similar concentration. For example, the latex spheres used for electroacoustic measurements were received from the manufacturer as stock suspensions with the same concentration (2.5 % w/v). These were both diluted with the same volume of deionized water and thus their electroacoustic response can be compared by assuming fixed properties of

the suspending medium. Comparing only samples with the same suspending medium will account also for the effect that the acoustic impedance of the suspension has on the measurement of the generated electroacoustic signal.

The relation of the electroacoustic effect to the difference in density between the solid and liquid phase is simply a matter of magnitude. That is, the electroacoustic signal generated by a nanoparticle sample is linear in $\Delta\rho$, regardless of the theory applied to give the functional form of the dynamic mobility, μ_D. Thus, even for particles with intermediate values of the double layer thickness (the regime likely applicable to nanoparticles, for which there exists only empirical formulations for the dynamic mobility), $\Delta\rho$ is a useful quantity for comparing the magnitude of the sample generated electroacoustic signal.

With the considerations given above, it is possible to discuss the electroacoustic measurements of the latex spheres with reference to their hydrodynamic size determined by light scattering and their assumed zeta-potential. A summary of the parameters relevant to the electroacoustic effect discussed above along with the hydrodynamic size is given in Table 5.1. Particle density and zeta-potentials are taken from Table 2.1 and the references therein. The density of the suspending medium (water) is taken as 1000 kg m^{-3}

As the latex spheres should have roughly the same zeta-potential [50] and density, comparing the electroacoustic measurements obtained for these two suspensions will allow for a determination of the effect that particle size has on the generated elec-

troacoustic signal. Figures. 4.20 and 4.25 show that for both field profiles used in the electroacoustic experiments, the calculated magnitude of the transducer response at the frequency of the applied field for the latex spheres was very close to that of the water filled cell. This is likely due to the very small difference in density between the latex spheres and the water in which they are suspended, therefore generating a small electroacoustic response.

For measurements performed using the Gauss2 field profile, the decrease in the maximum to the minimum magnitude of the transducer signal for the 500 nm latex is approximately 75% (from 10.5 to 13 MHz), compared with a change of roughly 30% for the 100 nm samples over the same frequency range. With the Gauss6 profile, the 500 nm latex sample shows an 80% decrease in magnitude from 9 MHz to 13 MHz, while the 100 nm latex decreases by a factor of 1/2 from 10.5 to 13 MHz. These results suggest that particles with larger hydrodynamic size will generate a

Table 5.1: Summary of the parameters relevant to the electroacoustic effect of the latex suspensions. Hydrodynamic radius is taken from fits of dynamic light scattering measurements and the particle density and zeta-potential from literature (see Table. 2.1).

Sample	$\mathbf{a}_{hydro}$ **(nm)**	$\Delta\rho/\rho$	ζ **(mV)**
100 nm	45	~ 0.1	-60
500 nm	240	~ 0.1	-60

more strongly decaying electroacoustic response over the frequency range measured, a trend particularly evident for the latex spheres due to their relatively monodisperse nature. That is, the intensity weighted distributions in hydrodynamic size determined from dynamic light scattering experiments (shown in Figs. 4.3 and 4.4) show very little variation with scattering angle. Therefore, any effects that a broad distribution in hydrodynamic size have on the generated electroacoustic signal are not expected to be strong for the latex spheres.

The insight gained from the electroacoustic measurements performed on the latex spheres allows for a discussion of the remaining samples. As the Lignosite and nanochips samples have similar composition, as determined by Reitveld refinement of measured x-ray diffraction patterns, these nanoparticle systems have similar density. Scherrer analysis of the peak broadening in the diffraction patterns gives a crystalline size of 10 and 16 nm for the nanochip and Lignosite samples, respectively. Reitveld refinement returned crystalline sizes of 6 and 5 nm. The hydrodynamic radii determined by light scattering measurements are 40 $\pm$ 20 for the nanochip and 140 $\pm$ 20 nm for the Lignosite. Finally, the hydrodynamic size of the Lignosite sample under the influence of a magnetic field is 50 $\pm$ 10 nm, as determined by the impedance technique.

There is large discrepancy between the crystalline size determined from x-ray diffraction and the hydrodynamic size determined by light scattering and impedance measurements. As the crystalline size is effectively an assessment of the uncoated and

unaggregated particle size, the difference between this crystallite size and the hydrodynamic size is attributed typically to the coating (x-ray diffraction is not sensitive to the coating materials as they consist primarily of elements with small atomic number that scatter only weakly the incident x-rays). The large difference for the nanochips is explained well by the dynamic light scattering experiments, results of which are shown in Fig. 4.2. The changing form of the hydrodynamic size distribution determined from dynamic light scattering measurements suggests that the nanochips have a non-spherical structure. This, in conjunction with the very wide size distributions observed for the nanochips, leads to an overestimation of the hydrodynamic size by dynamic light scattering.

The discrepancy between the hydrodynamic and crystalline size of the Lignosite sample is explained also by a consideration of the hydrodynamic size distributions determined through dynamic light scattering experiments. While the approximately 20 fold increase in hydrodynamic size compared with the crystalline size determined through x-ray diffraction experiments cannot be explained by the typical picture of a core coated with a surfactant, aggregation of the particles in suspension is likely. That is, in the water suspension, a number of Lignosite particles collect together leading to a larger hydrodynamic size, an effect seen in the dynamic light scattering experiments (a distribution centred on a significantly different hydrodynamic size was observed for the Lignosite sample, see Fig.4.6).

The size of the Lignosite nanoparticles as determined through susceptibility mea-

surements is also quite different from the hydrodynamic size determined by light scattering. While the impedance technique probes the same quantity as dynamic light scattering (diffusion in suspension), there is a bias to particles with a larger magnetic moment, as these would contribute more to measured magnetic susceptibility. The fit of the AC susceptibility of the Lignosite sample was performed under the assumption that the viscosity of the suspending medium was the same as that of water. This is likely not a valid assumption. This is a consequence of the magnetic susceptibility scaling with the number density of particles in suspension; a more concentrated sample is more easily measured with the impedance technique. Thus, measuring the nanoparticle susceptibility using the impedance technique required samples more concentrated than the ones used for the dynamic light scattering experiments. This would lead presumably to differences in the effective viscosity of the suspension. Additionally, the viscosity of a suspension of magnetic nanoparticles is influenced by the application of a magnetic field [10]. This effect can be seen also in the aminosilane coated nanoparticle sample. The hydrodynamic radius of this sample determined by dynamic light scattering was 15 $\pm$ 5 nm, compared with 60 $\pm$ 15 nm as determined by the impedance technique.

With the discussion above of the nanochip and Lignosite characterization by other methods, it is now appropriate to address the electroacoustic measurements of these samples. As before, a summary of the quantities relevant to the electroacoustic effect is provided in Table 5.3. As determined by refinement of the x-ray diffraction patterns,

these samples are both composed of iron-oxide and thus should have similar densities. While the zeta-potential of the nanochip sample is known from initial characterization using phase analysis light scattering, the charge of the Lignosite sample is unknown.

As shown with the latex samples, the difference in size leads to a change in the structure of the electroacoustic signal. For the electric field with the Gauss2 profile, the magnitude of the recorded transducer response when the cell was filled with Lignosite sample decreased by approximately 80% over the frequency range of 6 to 13 MHz after a sharp increase from the starting frequency. A similar decrease was not observed for the Gauss6 profile of the electric field. In fact, the electroacoustic response for the Lignosite increased by a factor of five from 4 to 9 MHz, after which the magnitude decreased by only approximately 40% at the end of the frequency range. The discrepancy in the electroacoustic response of the Lignosite sample between the two field profiles is most likely a consequence of the aggregation effects observed

Table 5.2: Summary of the parameters relevant to the electroacoustic effect of the nanochip and Lignosite suspensions. Hydrodynamic radii are taken from dynamic light scattering measurements and the density of iron-oxide from literature (see Table. 2.1).

Sample	$\mathbf{a}_{hydro}$ **(nm)**	$\Delta\rho/\rho$	ζ **(mV)**	**Crystalline size (nm)**
NC	40	4.2	-40	6
Lignosite	140	4.2	-	5

in the dynamic light scattering measurements. Indeed, it has been shown that a sample which exhibits aggregation will have variations in the measured electroacoustic response [38] (Sec. 1.3).

The electroacoustic measurements for the nanochip sample showed similar frequency dependencies between the two field profiles used. There is an initial four or five fold increase in magnitude of the transducer signal over the first 3 MHz of frequencies scanned, reaching a plateau at approximately 6 to 7 MHz until a frequency of 9 MHz. The presence of this plateau in frequency is attributed to the large distribution in hydrodynamic size of the nanochips assessed by dynamic light scattering measurements (see Fig. 4.2). That is, it is known from the electroacoustic measurements performed on the latex spheres that an increasing hydrodynamic size will act to reduce the electroacoustic response, attributable to increasing drag forces with increasing particle size. This result suggests that at a particular frequency of applied field, a certain range of hydrodynamic sizes will contribute more strongly to the measured electroacoustic signal. Therefore, a system with a broad size distribution will have strong contributions to the electroacoustic signal over a large range of frequencies.

The final two samples measured by the electroacoustic method are the Au and CoFe nanoparticles. The core size of the CoFe nanoparticles was determined to be 12 nm by Scherrer analysis of peaks in the x-ray diffraction pattern. Reitveld refinement of the diffraction pattern gave a crystalline size of 7 nm. The hydrodynamic

size in suspension was determined to be 300 ± 30 nm by dynamic light scattering. As was discussed for the Lignosite sample, this discrepancy between the core and hydrodynamic size cannot be explained simply by a surfactant. The reason for the discrepancy in hydrodynamic and crystalline size of the CoFe nanoparticles is quite clearly aggregation. The CoFe nanoparticles were observed to fall out completely out of suspension in less than one hour.

Dynamic light scattering measurements performed on the Au nanoparticles revealed a relatively monodisperse hydrodynamic size of 7 ± 1 nm, in agreement with sample synthesis conditions. A summary of the hydrodynamic sizes determined by dynamic light scattering along with the difference in density between the particles and suspending medium for the Au and CoFe nanoparticle samples is given in Table 5.3.

As all of the successful use of the electroacoustic technique reported in literature was performed on colloids with a hydrodynamic size of 200 nm or larger (Sec. 1.3), it

Table 5.3: Summary of the parameters relevant to the electroacoustic effect of the CoFe and Au nanoparticle suspensions. Hydrodynamic radius is taken from dynamic light scattering measurements and the densities from literature (see Table. 2.1).

Sample	$\mathbf{a}_{hydro}$ **(nm)**	$\Delta\rho/\rho$	ζ **(mV)**	**Crystalline size (nm)**
CoFe	300	4.6	-	6.79
Au	7	18	-	-

was expected that the CoFe nanoparticles, with a hydrodynamic diameter of 600 nm, in conjunction with the density of cobalt ferrite, would generate a large electroacoustic response. This was not observed in the electroacoustic measurements performed on the CoFe nanoparticle suspension. For the measurements performed with the Gauss2 field profile, the electroacoustic signal from the CoFe nanoparticles was smaller or equal to the transducer response for the water filled cell over all frequencies measured. With the Gauss6 field profile, the response of the CoFe filled cell is only slightly larger than the water filled cell at higher frequencies (from 8 MHz onward). Dynamic light scattering experiments performed on the CoFe nanoparticles revealed the presence of a wide size distribution (see Fig. 4.5). Considered in the context of electroacoustic measurements performed on the latex spheres and nanochip sample, the weak electroacoustic response of the CoFe nanoparticles is reasonable. A sample with a wide size distribution will have strong electroacoustic response over a wide range of frequencies whereas particles with larger hydrodynamic sizes will generate a smaller electroacoustic signal. The combination of these two effects is suggested as the origin of the weaker electroacoustic response observed for the CoFe nanoparticles.

The Au nanoparticles were found to be relatively monodisperse, with a very small hydrodynamic size (7 ± 1 nm) through dynamic light scattering experiments. This, in combination with their large density with respect to the medium in which they were suspended, leads to an expectation of a large electroacoustic response. The magnitude of the transducer signal for the electroacoustic measurements of the Au

nanoparticles was observed to not significantly deviate from the same measurements performed on a water filled cell. These results show that there is a reduced dynamic mobility for particles with very small hydrodynamic size, a result that is not consistent with predictions from the theory of electroacoustics for colloids with thin double layers. Therefore, the electroacoustic experiments performed on the Au nanoparticles suggest that a theoretical model applicable to particles with intermediate double layer thickness is required to more completely interpret the results of electroacoustic measurements on nanoparticle samples with very small hydrodynamic size.

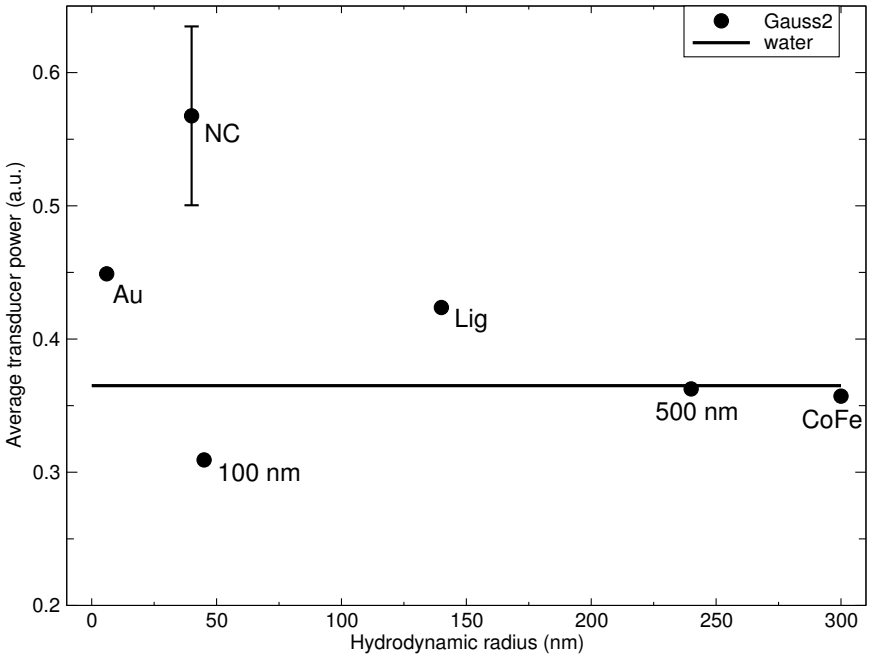

Figure 5.1: Average of the magnitude of the transducer signal for the Gauss2 field profile over all driving field frequencies. Error bars for the nanochip samples were determined from the standard deviation from two different data sets.

To compare better the electroacoustic results of all the samples together, the magnitude of the transducer signal for each sample was averaged over all driving field frequencies. Figure 5.1 shows the average magnitude of the transducer response for the Gauss2 field profile as a function of the mean hydrodynamic size determined through dynamic light scattering experiments. The nanoparticle samples, in order of increasing hydrodynamic radius, are: the Au nanoparticles (7 nm), nanochips (40 nm), 100 nm latex spheres (45 nm), Lignosite (120 nm), 500 nm latex spheres (240 nm) and finally the CoFe nanoparticle system (300 nm). Shown also in Fig. 5.1 (horizontal line) is the average of the transducer signal magnitude for the water filled cell. The average magnitude increases abruptly at small hydrodynamic radii and then decreases slowly past 50 nm. The outlier of this trend are the 100 nm latex spheres.

While the theoretical model for the dynamic mobility of colloids with thin double layers is likely not applicable to nanoparticle systems, components of the theory can be used to guide a discussion of the expected electroacoustic response of nanoparticles. The most strongly contributing factors to the expected electroacoustic response for dilute particle suspensions with thin double layers are the G function in Eqn. 1.9, describing the frequency dependent inertial effects, and the difference in density between the solid and liquid phase, $\Delta\rho$ in Eqn. 2.1. The relation of the electroacoustic effect to the difference in density between the solid and liquid phase is simply a matter of magnitude. That is, the electroacoustic signal generated by a nanoparticle sample is linear in $\Delta\rho$, regardless of the theory applied to give the functional form of the dy-

namic mobility, μ_D. Thus, even for particles with intermediate values of the double layer thickness (the regime likely applicable to nanoparticles, for which there exists only empirical formulations for the electrophoretic mobility), $\Delta\rho$ will contribute to the magnitude of the electroacoustic response. This is observed for the 100 nm latex spheres, which do not fall in line with the general trend observed in the average magnitude of the transducer response for the other samples.

The final strongly contributing factor to the electroacoustic response is the frequency dependent inertial drag force, which is shown for colloids with thin double layers in Fig. 1.7. The argument of this quantity depends most strongly on the particle hydrodynamic radius (quadratic dependence), with additional factors relating to the properties of the suspending medium and the frequency of the applied electric field. While the exact form of this function is not applicable to nanoparticles with intermediate values of double layer thickness, the general behaviour with particle size can likely be assumed for nanoparticle systems. That is, for a fixed frequency of applied electric field, the viscous drag forces will increase in magnitude with increases in the particle size, and thus lead to a decrease in the dynamic mobility, μ_D. A decrease in the average magnitude of the transducer signal with increasing hydrodynamic size of the particles is very clearly seen in Fig. 5.1. It is suggested that this decrease occurs due to the increasing viscous drag forces acting on particles with increasing particle size.

The average magnitude over all frequencies was calculated also for the electroa-

coustic experiments performed using the Gauss6 field profile, shown with the averages calculated for the Gauss2 pulse potential in Fig. 5.2. The average magnitude of the transducer response of the 100 nm latex sample for the electroacoustic measurement performed with the Gauss2 field profile was omitted for clarity. The average magnitude as a function of hydrodynamic size shows an almost identical form for measurements performed using the different field profiles. For the Gauss6 field profile, there is also a sharp increase in magnitude at small sizes followed by a slow decrease with increasing hydrodynamic radius past 50 nm. The 100 nm latex sample falls again outside of this trend, attributable to their small density.

Comparing the average magnitude for the different field profiles reveals only a difference in magnitude. This suggests that the form of the driving electric field has an effect on the electroacoustic response of the various nanoparticle suspensions. The ratio of the average magnitude for the Gauss2 and the Gauss6 field profiles are summarized for all samples in Table 5.4. The average magnitude of the transducer for the Gauss2 field profile is approximately 1.75 times larger than with the Gauss6 pulse potential, although there is some variation from sample to sample. It is suggested that these differences arise from the zeta-potentials of the measured samples, as the Gauss2 and Gauss6 pulse potentials do not differ in frequency but only in magnitude (a difference of roughly 10%). This is reinforced by the ratios of the average magnitude of the transducer signal for the Gauss2 and Gauss6 profiles for the latex samples (which have similar zeta-potential) being approximately the same. It is likely also

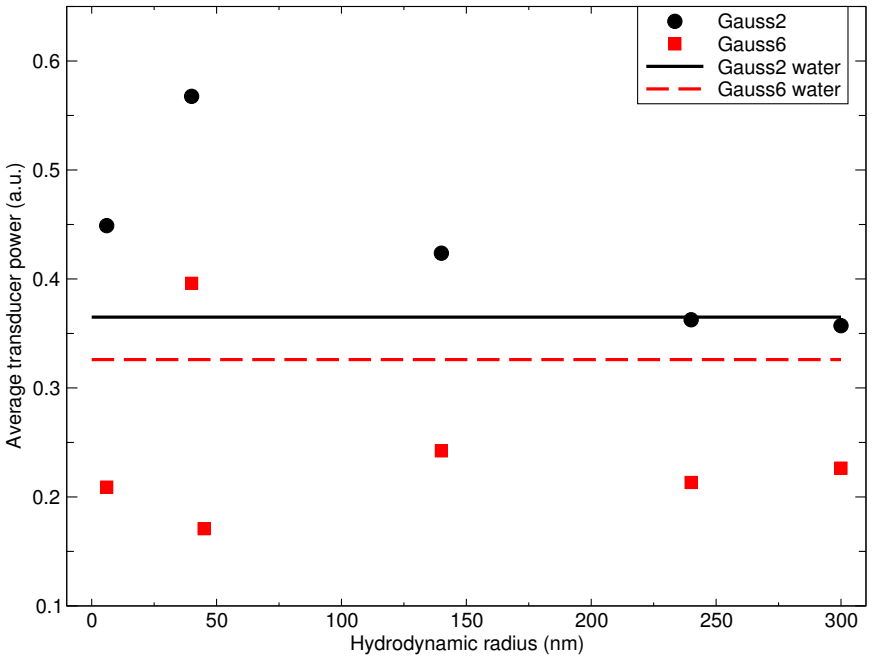

Figure 5.2: Average magnitude of the transducer signal for the Gauss2 and Gauss6 field profiles. The average magnitude of the 100 nm latex spheres for the Gauss2 profile is omitted for clarity.

Table 5.4: Ratios of the average magnitude of the transducer signal for the Gauss2 and Gauss6 field profiles.

Sample	100 nm	500 nm	Au	NC	CoFe	Lig
Ratio	1.81	1.70	2.15	1.44	1.58	1.77

that the length (in time) of the electric field pulse should have little effect on the dependence that the average magntidue has on particle hydrodynamic radius.

With this in mind, along with the known zeta-potential of the latex spheres and

Table 5.5: Estimate of the zeta-potential (ζ) magnitude from the ratio of the average magnitude of the transducer signal for electroacoustic measurements using the Gauss2 and Gauss6 field profiles.

Sample	100 nm	500 nm	Au	NC	CoFe	Lig
Ratio	1.81	1.70	2.15	1.44	1.58	1.77
Known ζ (mV)	60	60	-	40	-	-
Estimated ζ (mV)	-	-	90	-	50	60

the nanochip sample, a basic mapping of the ratio of the average magnitudes for the Gauss2 and Gauss6 field profiles to the nanoparticle zeta-potential can be made. An increase in the average magnitude between the two field profiles by a factor of approximately 1.75 was observed for the latex spheres, which have a zeta-potential of 60 mV. The nanochips, with a zeta-potential of 40 mV, showed an increase in magnitude from the Gauss6 to Gauss2 field profile by a factor of 1.44. With these two values, the relative increases in average magnitude of the transducer signal can be scaled to the difference in zeta-potential between the nanochips and the latex spheres. The results of using this scaling to estimate the zeta-potentials of the other samples is shown in Table 5.5.

While the current estimation of the zeta-potentials is only qualitative, the validity

of this assessment can be estimated by a consideration of the nanoparticle coatings of the Au, CoFe and Lignosite samples. The Au nanoparticles have tri-octylamine as a surfactant. This is a long chain molecule terminated with an amine group (NH_2). The amine group has a free pair of electrons and thus, it is expected that they have a relatively large surface charge. The CoFe nanoparticles have an oleic acid coating, terminated with a hydroxyl group and thus, is expected to have a smaller surface charge than the gold nanoparticles. Finally, the Lignosite sample has as surfactant sodium lignosulfonate. Sodium lignosulfonte is a long chain molecule terminated with a sulphur group and thus is expected to provide a surface charge similar to that of oleic acid. Therefore, the determined zeta-potentials are reasonable assessments considering to nature of the various coating materials. It is suggested that studying the changes in average magnitude of the transducer response using a single field profile at varying magnitude will allow for a more rigorous determination of the particle zeta-potential. In addition, confirming this estimation by measuring the electroacoustic response of other samples with known zeta-potential would be useful.

Mapping directly electroacoustic measurements of nanoparticles to a hydrodynamic size and zeta-potential requires new theories for the dynamic mobility of nanoscale colloids. These theories must account for physical phenomena which would likely act to modify the dynamic mobility for nanoparticles, the first of which are polarization effects. Nanoparticles fall in the intermediate range of double layer thickness where the characteristic dimension of the diffuse ion cloud surrounding the particle in

suspension is on the order of the particle radius. It is in this region where polarization effects are strongest [62]. Thus, in an applied electric field of sufficient magnitude, the diffuse layer could become adequately distorted as to produce a local electric field equal in magnitude and opposite in direction to the driving electric field. Thus, the nanoparticles in suspension would see effectively zero electric field and thus no driving force. This would clearly prevent the generation of pressure waves that would be measured as an electroacoustic signal.

Additionally, the polymer nature of the organic coatings used in nanoparticle synthesis could act to decrease a nanoparticle's dynamic mobility [63]. The coatings used for nanoparticles destined for eventual biomedical application are typically long-chain organic molecules. The theory of electroacoustics treats the colloidal particles as solid, with a diffuse layer consisting of ions with opposite charge to the particle surface, attracted electrostatically from the suspending medium. The retarding inertial forces acting on a moving particle in suspension are simply modifications of the viscous drag force for linear motion to include the deformation of the diffuse layer. The addition of long-chain organic molecules to the particle surface could lead to dramatically increase the drag forces experienced by the particles in suspension and thus suppress their electroacoustic response.

Chapter 6

Conclusions

To use successfully magnetic nanoparticles for biomedical applications requires a fundamental understanding of the effects that complex media have on nanoparticle hydrodynamic size and zeta-potential. To this end, an apparatus capable of measuring the dynamic mobility of colloidal suspensions was designed, constructed and made operational. The results of measurements using the electroacoustic method were mapped to samples with known zeta-potential and with hydrodynamic sizes determined using typical characterization methods (e.g. dynamic light scattering) in order to draw conclusions about the effectiveness of electroacoustic technique in determining nanoparticle hydrodynamic size and zeta-potential.

In the current configuration of the electroacoustic apparatus, the measured response from nanoparticle suspensions is not sufficiently large for a direct assessment of the nanoparticle's hydrodynamic size and zeta-potential; determining the desired

quantities from electroacoustic measurements requires a dynamic mobility that is resolvable into real and imaginary components. In addition, there exists currently no complete theory describing the dynamic mobility of nanoparticles (that likely fall into the regime of moderate double layer thickness) to which electroacoustic measurements can be mapped. With these limitations, focus was put on tracking the magnitude of the dynamic mobility of nanoparticle suspensions to the known zeta-potential and hydrodynamic size measured by other characterization techniques.

By comparing measurements of the electroacoustic response for latex calibration spheres of different hydrodynamic size, the effect of size on the magnitude of the measuring transducer signal was determined. The latex spheres are an excellent material for this determination because they have a small distribution in hydrodynamic size, shown clearly by dynamic light scattering experiments at a numerous of scattering angles. This is particularly important as it was found through electroacoustic measurements performed on other nanoparticle samples that a wide distribution in hydrodynamic size can alter the measured electroacoustic response. From experiments performed on the monodisperse latex samples, it was found that larger particle sizes correspond to a larger change in the electroacoustic response. While a theory for mapping the dynamic mobility of nanoparticles (with moderate double layer thickness) to their zeta-potential and hydrodynamic size is currently lacking, models of the dynamic mobility for colloids with thin double layers can be used as a guide to assess the validity of the electroacoustic results. That is, the effect of increasing particle size

is to decrease the dynamic mobility through an increase in the viscous drag forces acting on the particle, to which the results of the electroacoustic measurements on the latex spheres maps well.

The electroacoustic response of various other nanoparticle samples were also measured. The "nanochips" (plate-like nanoparticles) had a crystalline size of 6 nm as determined by Reitveld refinement of powder x-ray diffraction data, which confirmed also their composition as iron-oxide. The hydrodynamic size of the nanochip sample was determined to be 40 $\pm$ 20 nm by dynamic light scattering which revealed also their non-spherical structure through changes in the distribution shape as a function of scattering angle. The electroacoustic measurements performed on this sample showed a plateau in the magnitude of the transducer signal at moderate frequencies of the applied electric field, which is likely a consequence of their broad size distribution. At a particular frequency of applied electric field, the electroacoustic instrument is more sensitive to a small range of sizes. Therefore, a nanoparticle suspension with a broad size distribution will have constituents which contribute more strongly to the measured electroacoustic response over a range of frequencies.

The Lignosite and cobalt ferrite samples showed a large discrepancy between the crystalline size determined by x-ray diffraction measurements and the hydrodynamic size assessed by dynamic light scattering. The simple picture of a hard particle core coated in surfactant is not sufficient to account for this discrepancy. The discrepancy was attributed to aggregation effects occurring in these suspensions. Aggregation in

the Lignosite sample was confirmed by dynamic light scattering experiments which revealed the presence of multiple size populations, whereas the cobalt ferrite visibly fell out of suspension. The electroacoustic response of the Lignosite sample was small when compared with that of the nanochips. This was attributed to aggregation effects, which have been shown to lead to variations in the electroacoustic response of micrometre-sized colloids [38].

The cobalt ferrite nanoparticles were expected to show the strongest electroacoustic response as they have a large density and their hydrodynamic size ($\sim$ 600 nm diameter) is within the range of sizes previously measured by the electroacoustic method. The recorded electroacoustic response for this sample was only slightly larger than the same measurements performed on the water filled cell. Dynamic light scattering experiments revealed a broad hydrodynamic size distribution for this system, which, in combination with the increased inertial drag force experienced by larger particles, was suggested as the origin of the weakened electroacoustic response from this sample.

Relatively monodisperse gold nanoparticles (as confirmed by dynamic light scattering) were measured also by the electroacoustic method. It was predicted that the gold nanoparticles, having a large density and well defined size, would exhibit a large electroacoustic response. This prediction did not hold true in that the electroacoustic measurements for this system did not deviate significantly from the response of the water filled cell. Thus, these measurements show that there is a reduced dynamic

mobility for very small particles, a result that is not consistent with the theory of electroacoustics for colloids with thin double layers. This suggests that a theoretical model describing the dynamic mobility of colloids with intermediate double layers is required to more completely interpret the results of electroacoustic measurements on nanoparticle suspensions.

To compare the electroacoustic response of all samples together, the recorded magnitude of the transducer signal for each sample was averaged over all frequencies of the applied electric field. Displaying the average magnitude of the transducer signal as a function of the hydrodynamic size of the samples determined by dynamic light scattering showed an increase in the electroacoustic response up to a size of 40 nm (the nanochip sample) and then a slow decrease with increasing size. While this trend with hydrodynamic size was found for both of the pulse potentials used to drive the electric field, there was an observed change in average magnitude of the transducer signal. As the two types of applied electric fields had the same frequency and differing amplitude and bandwidth, the change in magnitude of the transducer signal between the two different pulse potentials was attributed to the zeta-potential of the particles. Therefore, the ratios of the average magnitudes of the transducer signals were used in conjunction with the known zeta-potentials of the latex and nanochip samples to estimate the zeta-potentials of the other three nanoparticle samples. The results of this estimate agreed qualitatively with expectations based on the organic materials coating the various nanoparticle systems.

The most likely physical mechanism masking the electroacoustic response of the smallest particles measured is through the polarization of the double layer. In response to an applied electric field, the electrical double layer becomes distorted sufficiently to produce a local electric potential equal in magnitude but opposite in direction to the applied field. The nanoparticles see effectively zero electric field, inducing no motion and thus, not generating pressure oscillations that can be recorded as an electroacoustic response. Nanoparticles fall likely in the regime where the double layer thickness is on the order of the size of the solid core, where polarization effects are strongest. An additional physical mechanism that could act to reduce the dynamic mobility of nanoparticle suspensions with very small hydrodynamic size is through the nature of their coatings, which are typically long-chain organic molecules. The diffuse nature of these coatings could act to increase dramatically the viscous drag forces experienced by the particles and thus reduce their dynamic mobility further.

The electroacoustic apparatus in its current state was able to probe the dynamic mobility of various nanoparticle suspensions. The hydrodynamic size dependence of the electroacoustic response was determined by mapping the average magnitude of the measuring transducer to the hydrodynamic radii of the various samples measured. Zeta-potentials were estimated by comparison of the average magnitude of the transducer signal recorded for electric fields with different magnitudes and using nanoparticle systems with known zeta-potentials. It was determined also that the current theory of electroacoustics, valid for particles with thin double layers, is not

applicable for nanoparticle suspensions. Further refinement of the electroacoustic apparatus will allow ultimately the development of a fundamental understanding of the effects that complex media have on nanoparticle surface properties and permit the rational design of nanoparticle systems for future biomedical use.

6.1 Future work

Several improvements can be made to the electroacoustic apparatus in order to increase its sensitivity. In its current configuration, the electrical response (crosstalk) of the transducers to the burst potential driving the electric field is the most pressing issue. The decay of this initial response is long enough to mask the detection of the electroacoustic response generated closest to the measuring transducer, which should be the strongest signal from the sample. Several solutions to this problem exist; either by increasing the lengths of the quartz delay rods to increase the expected detection time past the complete decay of crosstalk or by reducing electrical reflections through matching the electrical impedance of the electroacoustic cell to that of the field-driving electronics. Additionally, electrical shielding (e.g. Faraday cage) can be used to suppress further the interaction between the driving potential and the measuring transducers.

Measuring the electroacoustic response over a wider range of frequencies is precluded by the current selection of piezoelectric transducer. As it is difficult to construct a transducer that has sufficient bandwidth to cover the desirable frequency

range (up to 30-40 MHz), a possible solution is to replace one of the transducers with one sensitive to higher frequencies. Thus, both low and high frequency measurements could be performed with a single instrument. This would have the added benefit of reducing undesirable ultrasound waves passing through the system. For example, when the electric field is being driven at low frequencies, the high frequency transducer should have a smaller electrical response to the applied potential and thus the compression wave produced from the initial crosstalk will be smaller in magnitude.

Bibliography

[1] S. Mornet, S. Vasseur, F. Grasset, and E. Duguet, J. Mater. Chem. **14**, 2161 (2004).

[2] G. Liu, J. Gao, H. Air, and X. Chen, Small **9**, 1533 (2013).

[3] Z. Sun *et al.*, Int. J. Nanomed. **9**, 1 (2014).

[4] J. Wang, J. Byrner, M. Napier, and J. DeSimone, Small. **7**, 1919 (2011).

[5] B. Ware and W. Flygare, Chem. Phys. Lett. **12**, 81 (1971).

[6] J. Miller, K. Schätzel, and B. Vincent, J. Colloid Interf. Sci. **143**, 532 (1991).

[7] J. Gisma, Colloids Surfaces A. **149**, 451 (1999).

[8] B. Berne and R. Pecora, *"Dynamic light scattering with applications to chemistry, biology and physics"*, First ed. (Dover Publications, Mineola, NY, 2000).

[9] A. Arelaro *et al.*, J. Appl. Phys. **97**, 10J316 (2005).

[10] J. Nowak, F. Wiekhorst, L. Trahms, and S. Odenbach, J. Phys.: Condens. Matter. **26**, 176004 (2014).

[11] T. Cosgrove, *"Colloid science: Principles, methods and applications"*, Second ed. (John Wiley & Sons, West Sussex, UK, 2010).

[12] B. Binks, Curr. Opin. Colloid In. **7**, 21 (2002).

[13] A. Delgado, F. Gonzalez-Caballero, R. Hunter, L. Koopal, and J. Lyklema, J. Colloid Interf. Sci. **309**, 194 (2007).

[14] T. Doane, C.-H. Chuang, R. Hill, and C. Burda, Acc. Chem. Res. **45**, 317 (2012).

[15] W. Russel, D. Saville, and W. Schowalter, *"Colloidal dispersions"* (Cambridge University Press, New York, NY, 1989).

[16] M. Smoluchowski, *"Handbook of electricity and magnetism"* (, 1921).

[17] E. Hückel, Phys. Z. **25**, 204 (1924).

[18] D. Henry, Proc. R. Soc. London A. **133**, 533 (1931).

[19] B. Marlow, D. Fairhurst, and H. Pendse, Langmuir **4**, 611 (1988).

[20] P. Debye, J. Chem. Phys. **1**, 31 (1933).

[21] J. Bugosh, E. Yaeger, and F. Hovarka, J. Chem. Phys. **15**, 542 (1947).

[22] J. Hermans, Philos. Mag. **25**, 426 (1938).

[23] A. Rutgers, A. Physica **5**, 46 (1938).

[24] R. O'Brien, J. Fluid Mech. **190**, 71 (1988).

[25] R. O'Brien, D. Cannon, and W. Rowlands, J. Colloid Interf. Sci. **173**, 406 (1995).

[26] R. O'Brien, P. Garside, and R. Hunter, Langmuir **10**, 931 (1994).

[27] R. Zana and E. Yaeger *"Modern aspects of electrochemistry"* Vol. 14 (Plenum, New York, NY, 1982).

[28] J. Bickerman, Trans. Faraday Soc. **36**, 154 (1940).

[29] A. Dukhin and P. Goetz, Colloids Surfaces A. **192**, 267 (2001).

[30] R. O'Brien, A. Jones, and W. Rowlands, Colloids Surfaces A. **218**, 89 (2003).

[31] A. Harker and J. Temple, J. Phys. D.: Appl. Phys. **21**, 1576 (1988).

[32] A. Dukhin and P. Goetz, Langmuir **12**, 4987 (1996).

[33] T. Oja, G. Peterson, and D. Cannon, U.S. Patent 4,497,208 (1985).

[34] V. Hackley and S. Malghan, Ceram. Trans. **56**, 283 (1995).

[35] J. Wade, W. Beattie, W. Rowlands, and M.-A. Augustin, J. Dairy Res. **63**, 387 (1996).

[36] A. Dukhin and P. Goetz, Colloids Surfaces. A. **144**, 49 (1998).

[37] M. Tourbin and C. Frances, Powder Technol. **190**, 25 (2009).

[38] B. Klein, N. Altun, M. Colebrook, and M. Pawlik, Int. J. Miner. Process. **110**, 12 (2012).

[39] J. Tressler, S. Alkoy, and R. Newnham, J. Electoceram. **2**, 257 (1998).

[40] H. Kawai, Jpn. J. Appl. Phys. **8**, 975 (1969).

[41] J. Wackerle, J. Appl. Phys. **33**, 922 (1962).

[42] R. O'Brien, B. Midmore, A. Lamb, and R. Hunter, Faraday Discuss. Chem. Soc. **90**, 301 (1990).

[43] L. Brown, IEEE Trans. Ultrason., Ferroelect., Freq. Contr. **47**, 1377 (2000).

[44] R. Xu, Particuology **6**, 112 (2008).

[45] A. Einstein, Ann. d. Physik **17**, 549 (1905).

[46] L. Néel, Ann. Géophys. **5**, 99 (1949).

[47] W. Brown, J. Appl. Phys. **34**, 1319 (1963).

[48] P. Debye, *"Polar molecules"* (Chemical Catalogue Company, New York, NY, 1929).

[49] P. Fannin, B. Scaife, and S. Charles, J. Magn. Magn. Mater. **72**, 95 (1988).

[50] I. Ermolina and H. Morgan, J. Colloid Interf. Sci. **285**, 419 (2005).

[51] R. Weast, editor, *"CRC Handbook of chemisty and physics"*, 64 ed. (CRC Press, Boca Raton, FL, 1984).

[52] V. Yathindranath *et al.*, Langmuir. **29**, 10850 (2013).

[53] K. Maaz, A. Mumtaz, S. Hasanain, and A. Ceylan, J. Magn. Magn. Mater. **308**, 289 (2007).

[54] J. Rockenberger, E. Scher, and A. Alivisatos, J. Am. Chem. Soc. **121**, 11595 (1999).

[55] R. Weast, editor, *"CRC Handbook of chemisty and physics"*, 64 ed. (CRC Press, Boca Raton, FL, 1984).

[56] R. Weast, editor, *"CRC Handbook of chemisty and physics"*, 64 ed. (CRC Press, Boca Raton, FL, 1984).

[57] S. Ammar *et al.*, J. Mater. Chem. **11**, 186 (2001).

[58] V. D. Grosso and C. Mader, J. Acoust. Soc. Am. **52**, 1442 (1972).

[59] H. Rietveld, J. Appl. Cryst. **2**, 65 (1969).

[60] P. Scherrer, Göttinger Nachrichten Gesell. **2**, 98 (1918).

[61] J. Rodriguez-Carvajal, *"Satellite meeting on powder diffraction of the XV congress of the IUCr",* **vol. 127.**, Toulouse, France (1990).

[62] V. Shilov, Y. Borkovskaja, and A. Dukhin, J. Colloid Interf. Sci. **277**, 347 (2004).

[63] R. Hill and D. Saville, Colloids Surfaces A. **267**, 31 (2005).